Electronic Supplementary Information for:

Vacuum-Responsive and Water-Soluble Lanthanide(III)/2-Oxonicotinate Coordination Polymers with High Photoluminescence Efficiency

Maialen Terceño-Carrillo,[a] Laura Razquin-Bobillo,[a] Sergio Carrasco,[b] Patricia Horcajada,[b] Garikoitz Beobide,[c] Jose Angel García,[d] Pablo Salcedo-Abraira,[e] Andoni Zabala-Lekuona,[a] Antonio Rodríguez-Diéguez[e] and Javier Cepeda*[,a]

[a] *Departamento de Química Aplicada, Facultad de Química, Universidad del País Vasco (UPV/EHU), 20018 Donostia, Spain.* [b] *Advanced Porous Materials Unit, IMDEA Energy Institute, Avda. Ramón de la Sagra 3, 28935, Móstoles, Madrid, Spain.* [c] *Departamento de Química Orgánica e Inorgánica, Facultad de Ciencia y Tecnología, University of the Basque Country (EHU), 48940 Leioa, Spain* [d] *Departamento de Física, Facultad de Ciencia y Tecnología, Universidad del País Vasco/Euskal Herriko Unibertsitatea (UPV/EHU), 48940 Leioa, Spain.* [e] *Departamento de Química Inorgánica, UEQ, C/ Severo Ochoa s/n, Universidad de Granada, 18071, Granada, Spain.*

Contents:

S1. Experimental details.

Chemical characterization. Elemental analyses (C, H, N) were performed on a Leco CHNS-932 microanalyzer. FTIR spectra were recorded using KBr pellets in a ThermoNicolet IR 200 spectrometer in the 4000−400 cm^{-1} region. Thermal analyses (TG/DTA) were performed using a TA SDT 2960 thermal analyzer in a synthetic air atmosphere (79% N_2 / 21% O_2) with a 5 °C·min^{-1} heating rate. Solid-state absorption spectra were measured on a UV-2600 UV/Vis Shimadzu spectrophotometer over polycrystalline samples in order to assign the excited states participating in the photoluminescence process. These spectra were measured at room temperature using $BaSO_4$ as a reference material.

X-ray diffraction data collection and structure determination. Suitable single crystals of compounds $\mathbf{1}_{Y}$, $\mathbf{2}_{Nd}$, $\mathbf{3}_{Eu}$, $\mathbf{4}_{Gd}$, $\mathbf{5}_{Tb}$ and $\mathbf{6}_{Dy}$ were used for the structure determination. Single crystal X-ray diffraction (SCXD) data collection of $\mathbf{3}_{Eu}$, $\mathbf{4}_{Gd}$ and $\mathbf{6}_{Dy}$; and for $\mathbf{1}_{Y}$, $\mathbf{2}_{Nd}$, and $\mathbf{5}_{Tb}$ was done at 150 and 296 K, respectively, on a Bruker VENTURE area detector equipped with graphite monochromated Mo K_α radiation (λ = 0.71073 Å) and with a Phonon3 detector. The temperature during data collection was controlled by means of a dry N_2 cryostream (Oxford Cryostream 700). Data reduction of $\mathbf{1}_{Y}$, $\mathbf{3}_{Eu}$, $\mathbf{5}_{Tb}$ and $\mathbf{6}_{Dy}$ was performed with the APEX4[1] software and corrected for absorption using SADABS[2]. Data reduction of $\mathbf{2}_{Nd}$ and $\mathbf{4}_{Gd}$ was performed by using CrysAlisPro software and applying the ABSPACK absorption correction. $\mathbf{2}_{Nd}$ crystal was found to be twinned and thus processed and refined as two-component twin. Crystal structures were solved by intrinsic phasing using the SHELXT program[3] and refined by full-matrix least-squares on F^2 including all reflections employing the Olex2 software.[4] All hydrogen atoms were located in the difference Fourier map and included as fixed contributions using riding models with isotropic thermal displacement parameters 1.2 times those of their parent atoms for the 2onic ligand. Main parameters of the refinement of the crystal structure can be found in Table S1. Crystallographic data has been deposited with the Cambridge Crystallographic Data Center as supplementary publication with nos. CCDC 2456148-2456153. Copies of the data can be obtained free of charge on application to the Director, CCDC, 12 Union Road, Cambridge, CB2 1EZ, U.K. (Fax: +44-1223-335033; e-mail: deposit@ccdc.cam.ac.uk or http://www.ccdc.cam.ac.uk).

The powder X-ray diffraction (PXRD) patterns were measured over polycrystalline samples. For data acquisition, a Philips X'PERT powder diffractometer was used with Cu-Kα radiation (λ = 1.5418 Å) over the $5 < 2\theta < 50°$ range with a step size of 0.026° and an acquisition time of 2.5 s per step at 25 °C. Indexation of diffraction profiles was made using the FULLPROF program (pattern matching analysis)[5] based on the space group and cell parameters obtained from single crystal X-ray diffraction.

Variable-pressure powder X-ray diffraction experiments. Variable-pressure powder X-ray diffraction experiments were performed on a BRUKER D8 Advance A25 diffractometer (3-50º (2θ), step size 0.01º, step time 0.5 s, 25 ºC) equipped with a Pb safety slit (1 mm). An electronic manometer was coupled to the diffraction chamber, while a quaternary valve at the inlet allowed selection between Ar (ultra-high purity, 99.999%), compressed air, or ambient pressure. Internal pressure was determined by the maximum admissible pressure of the PXRD chamber at a constant gas flow rate of 100 mL/min (1584 mbar for air, 1728 mbar for Ar). The outlet was connected to a rotary pump, achieving a minimum pressure of 20 mbar. Before data acquisition, samples were equilibrated for 2 h under the selected pressure/vacuum conditions and through consecutive pressurization-depressurization cycles.

Additional CO_2 pressure experiments were conducted in a 100-mL stainless steel miniclave reactor (Buchiglas, Büchi AG) equipped with a manometer. Samples were exposed to CO_2 (10 bar) for 16 h at 25 ºC using an external water bath for temperature control. Subsequent PXRD patterns were collected on a Malvern Panalytical Empyrean diffractometer in the 3-35º (2θ) range with a step size of 0.013º at room temperature.

Photoluminescence measurements. Photoluminescent measurements were recorded using polycrystalline samples at room temperature and pressure as well as under high vacuum (of *ca.* 10^{-9} mbar) in the 10-310 K range by using a closed-cycle helium cryostat. These latter conditions avoid the presence of oxygen and also remove some of the water molecules present in the compounds. The sample holder is enclosed in an Edinburgh Instruments FLS920 spectrometer. For steady-state measurements, an IK3552R-G HeCd continuous laser (325 nm) and a Müller-Elektronik-Optik SVX1450 Xe lamp were used as excitation sources. In contrast, a pulsed laser diode and a μF900 lamp were employed for recording the decay curves. Photographs of the irradiated samples were taken at room temperature using an Olympus optical microscope illuminated with a Hg lamp. Quantum yield measurements were also performed using polycrystalline samples into a Horiba Quanta-φ integrating sphere, which are irradiated using an Oriel Instruments MS257 lamp as an excitation source and coupled to iHR550 spectrometer from Horiba to analyze the emission.

Computational details. TD-DFT calculations were performed over a suitable model of compound $\mathbf{4_{Gd}}$ obtained from single-crystal X-ray measurements using the Gaussian 16 package.[6] The Becke three-parameter hybrid functional with the nonlocal correlation functional of Lee-Yang-Parr (B3LYP)[7–9] and 6-311G(d) basis for non-metallic atoms and the LANL2DZ basis set for Zn(II) was employed.[10–12] The results were analyzed with the GausSum programme[13] and the molecular orbitals were plotted using the GaussView software.[14]

Table S1. Crystallographic data and structure refinement details of compounds $\mathbf{1_Y}$, $\mathbf{2_{Nd}}$, $\mathbf{3_{Eu}}$, $\mathbf{4_{Gd}}$, $\mathbf{5_{Tb}}$ and $\mathbf{6_{Dy}}$.

	$\mathbf{1_Y}$	$\mathbf{2_{Nd}}$	$\mathbf{3_{Eu}}$	$\mathbf{4_{Gd}}$	$\mathbf{5_{Tb}}$	$\mathbf{6_{Dy}}$
Empirical formula	$C_{12}H_{14}ClN_2O_{13}Y$	$C_{12}H_{14}ClN_2NdO_{13}$	$C_{12}H_{14}ClEuN_2O_{13}$	$C_{12}H_{14}ClGdN_2O_{13}$	$C_{12}H_{14}ClN_2O_{13}Tb$	$C_{12}H_{14}ClDyN_2O_{13}$
Formula weight	518.61	573.94	581.66	586.95	588.62	592.20
Crystal system	Monoclinic	Monoclinic	Monoclinic	Monoclinic	Monoclinic	Monoclinic
Space group	*P2/n*	*P2/n*	*P2/n*	*P2/c*	*P2/n*	*P2/n*
***a* (Å)**	9.8421(4)	9.9993(5)	9.9135(2)	9.706(3)	9.8908(5)	9.8783(3)
***b* (Å)**	6.4939(2)	6.5954(4)	6.4668(2)	6.298(2)	6.5206(3)	6.4121(2)
***c* (Å)**	28.5798(12)	28.6126(13)	28.4817(7)	30.301(15)	28.5986(14)	28.4029(10)
***β* (°)**	95.6210(10)	95.730(4)	95.7030(10)	114.22(5)	95.618(2)	95.6940(3)
V (Å^3)	1817.85(12)	1877.56(17)	1822.38(8)	1689.1(13)	1835.58(15)	1790.18(10)
Z	4	4	4	4	4	4
T (K)	150	150	150	150	150	150
μ (mm^{-1})	3.430	2.980	3.663	4.165	4.072	4.399
ρ (g cm^{-3})	1.895	2.030	2.120	2.308	2.130	2.197
Crystal size (mm^3)	0.1 × 0.08 × 0.005	0.10 x 0.06 x 0.05	0.10 x 0.075 x 0.002	0.08 x 0.075 x 0.005	0.04 × 0.02 × 0.02	0.08 x 0.07 x 0.02
F(000)	1040.0	1124.0	1136.0	1140.0	1144.0	1148.0
Unique reflections / total	3722 / 21059	7443 / 7443	3750 / 25859	1767 / 1767	3759 / 3759	3664 / 3664
GOF[a]	1.202	1.151	1.196	1.057	1.081	1.221
R_{int}	0.0497	0.0844	0.0347	0.1909	0.0484	0.0285
Final R indices						
R_1[b] / wR_2[c] [I>2σ(I)]	0.0560 / 0.1296	0.0917 / 0.2459	0.0274 / 0.0543	0.0805 / 0.1793	0.0238 / 0.0472	0.0330 / 0.0689
R_1 / wR_2 (all data)	0.0647 / 0.1329	0.0917 / 0.2460	0.0417 / 0.0646	0.1393 / 0.2178	0.0371 / 0.0526	0.0461 / 0.0795

[a] $S = [\sum w(F_0^2 - F_c^2)^2 / (N_{obs} - N_{param})]^{1/2}$. [b] $R_1 = \sum||F_0|-|F_c|| / \sum|F_0|$. [c] $wR_2 = [\sum w(F_0^2 - F_c^2)^2 / \sum wF_0^2]^{1/2}$; $w = 1/[\sigma^2(F_0^2) + (aP)^2]$ where $P = (\max(F_0^2,0) + 2F_c^2)/3$ with a = 14.7462 (**1_Y**), 0.1054 (**2_{Nd}**), 11.9889 (**3_{Eu}**), 0.0652 (**4_{Gd}**), 4.9152 (**5_{Tb}**), 22.1986 (**6_{Dy}**); b = 38.3066 (**2_{Nd}**), 109.7479 (**4_{Gd}**).

S2. Thermal characterization of compounds.

The thermal behaviour of compound $\mathbf{3_{Eu}}$ has been studied as a representative compound on the basis of the results obtained from thermogravimetric/differential thermal analyses (TG/DTA). As it can be seen in Figure S1, when the compound is heated from room temperature on, it remains unaltered without losing mass up to 100 ºC. Above this temperature, the sample presents two continuous mass loss steps: i) a first one in 110–165 ºC range that corresponds to the loss of 4 H_2O molecules and ii) a second step that accounts for the loss of the remaining 2 H_2O molecules in the 165–200 ºC range. Then, the TG curve shows a plateau in the 205–305 ºC range, after which a strong exothermic process related to the decomposition of the organic ligand takes place, which eventually yields the final residue identified as Eu_2O_3 at 700 ºC.

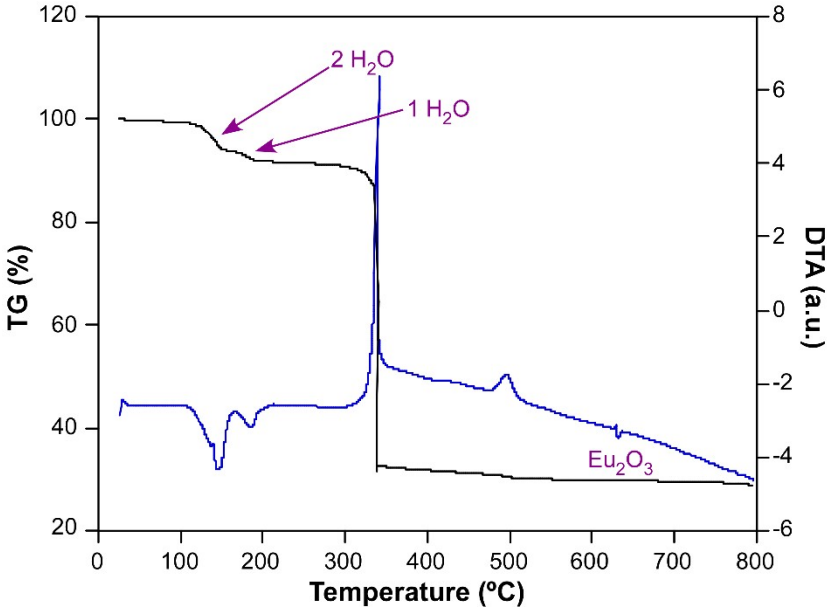

Figure S1. TG/DTA curves of compound $\mathbf{3_{Eu}}$.

Table S2. Thermal analysis data for compound $\mathbf{3_{Eu}}$.

Steps	T_i	T_f	T_{max}	ΔH	ΣΔm(%)	$\Sigma\Delta m(\%)_{theo}$	$\Delta m(\%)_{theo}$
1	30	105	–	–	0.0	0.0	0.0
2	105	165	145	endo	6.6	6.1 (–$4H_2O$)	6.6 (–$4H_2O$)
3	165	205	190	endo	8.8	9.2 (–$6H_2O$)	2.2 (–$2H_2O$)
4	205	300	–	–	8.8	9.2	0.0
5	300	530	345	exo	62.3	–	–
–	700	700	–	–	28.9	29.9 (Eu_2O_3) [a]	residue

Codes: T_i: initial temperature; T_f: final temperature; T_{max}: temperature of the DTA signal maximum for each step; ΣΔm: released mass summatory; ΔH: process type; $\Sigma\Delta m_{theo}$: theoretically released mass summatory; Δm_{theo}: theoretically released mass in each step. [a] This percentage corresponds to the mass of the final product (%).

Additionally, a thermodiffractometric study has been also conducted within 30-510 ºC, in which a diffractogram has been measured under continuous heating every 20 ºC. As observed in the next figure, the diffractograms recorded on the sample confirm that the compound remains crystalline up to 110 °C, although remarkable shifts in some maxima are observed in the diffractogram recorded at 130 °C. Upon heating, the diffraction maxima slowly lose intensity and at 170 °C a completely amorphous compound is obtained.

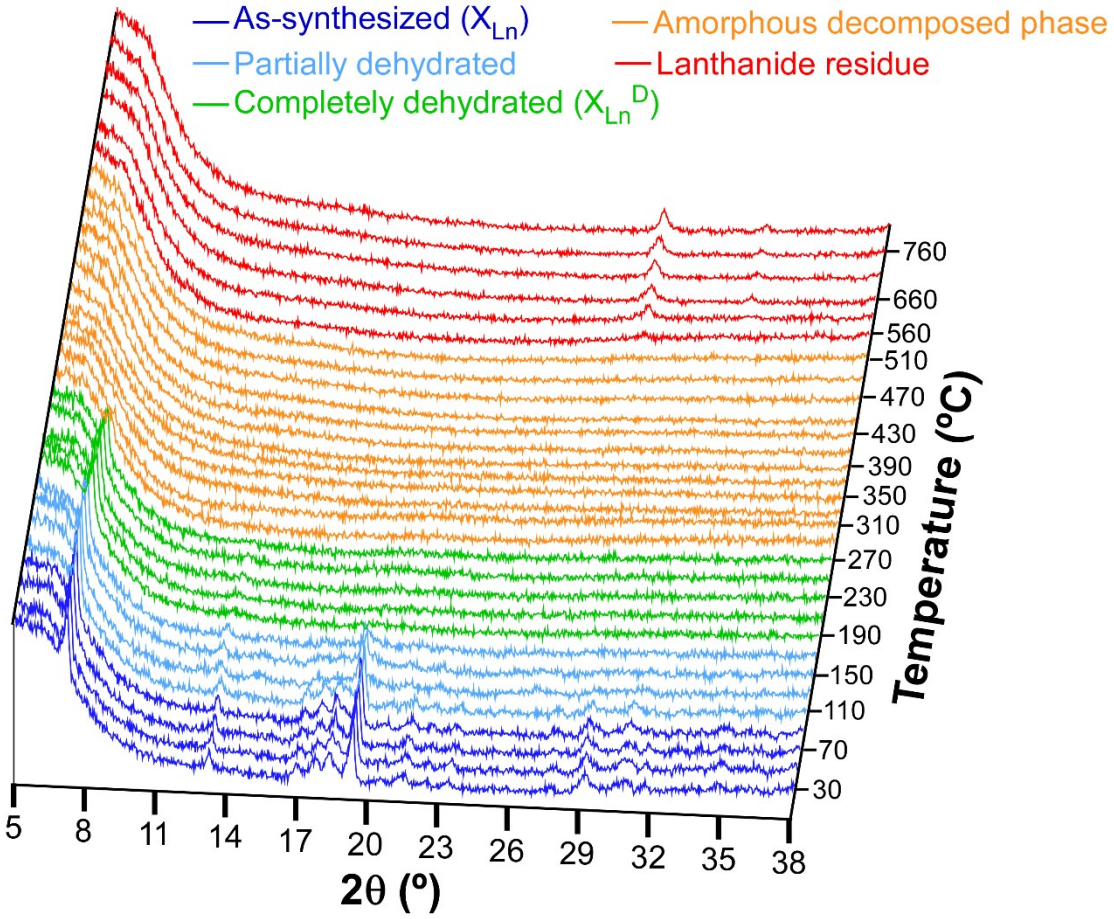

Figure S2. Thermodiffractometric data recorded on compound $\mathbf{3}_{\mathbf{Eu}}$. Three main groups of diffractograms are distinguished in different colours: i) original compound (blue), ii) progressively dehydrated compound (light blue), iii) completely degraded compound (green), iv) amorphous phase with decomposed product v) generated oxide as calcination residue.

S3. FT-IR spectroscopy.

Infrared spectroscopy has been used for the initial characterization of the compounds, as it allows us to check whether the synthesized complexes contain the ligand and whether it is coordinated to the metals. The spectra obtained for all compounds show a similar structure (Figure S3) given that the ligand exhibits the same coordination pattern in all compounds. In this sense, it should be mentioned that as a consequence of the chelating ring established with the lanthanide(III) atom, the ligand adopts the 1H-2-oxonicotinate tautomer.

In all spectra, the first band appearing between 3500-3300 cm^{-1} corresponds to the vibrational stretching of the O-H bonds of the adsorbed water molecules in the samples by ambient humidity (in the case of the free ligand) or of the water molecules of crystallization. This band is followed by a second, broader band in the 3300-2300 cm^{-1} range, which corresponds to the vibrations of the O-H, N-H and C-H bonds of the ligand. It is significant that in the ligand spectrum this band is much more intense than with the compounds, as the inter- and intra-molecular hydrogen bonds between the ligand molecules vibrate more intensely. In particular, a robust band of the protonated carboxylate group is seen in the ligand and weak vibrational signals of the N-H and C-H pyridine ring are observed in all compounds. The strong bands appearing in the range 1725-1450 cm^{-1} correspond to asymmetric vibrations of the carboxylate group and the C-C and C-N bonds of the aromatic ring, while the symmetric vibrations of the carboxylate group appear in the range 1400-1200 cm^{-1}. Again, the spectrum of the free ligand shows a strong broad band between 1725-1665 cm^{-1} and narrower at 1508 cm^{-1}, which corresponds to the protonation of the carboxylate group. It should also be noted that some symmetric vibrations of the carboxylate group are rather impeded in the compounds by the coordination form adopted in the compounds. The remaining bands of smaller wavenumbers can be assigned to the distortions occurring in the aromatic ring.

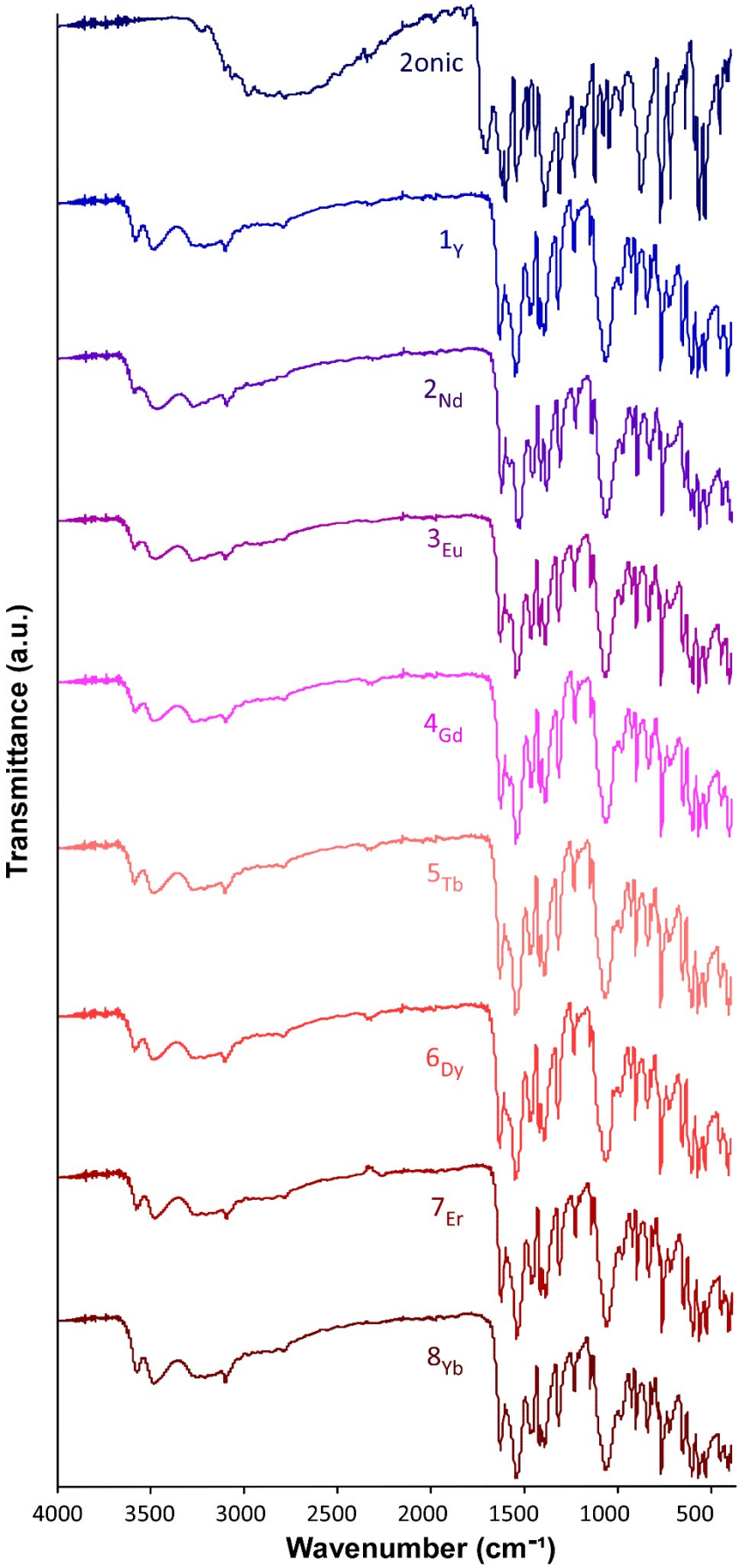

Figure S3. IR spectra of free ligand and isostructural compounds.

S4. Powder X-ray diffraction analysis of as-synthesized compounds.

Pattern-matching analysis confirms the purity of the polycrystalline samples of all compounds.

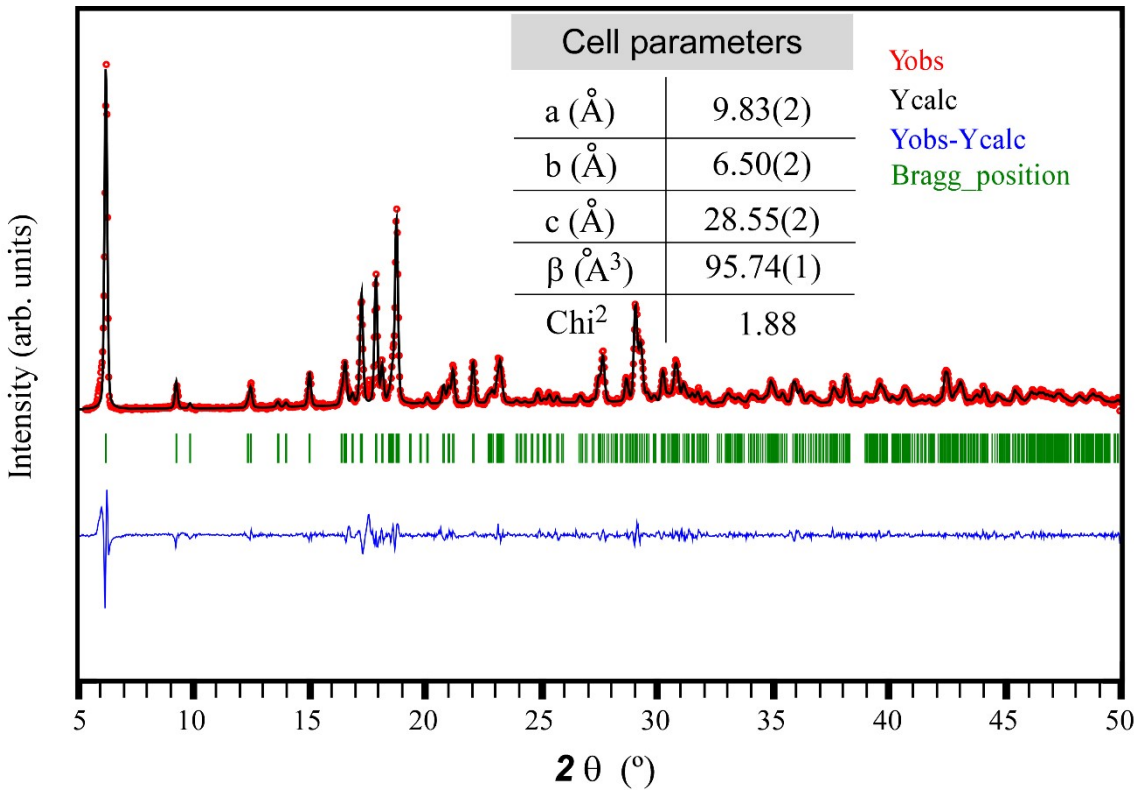

Figure S4. Full profile pattern matching analysis of the PXRD of $\mathbf{1_Y}$.

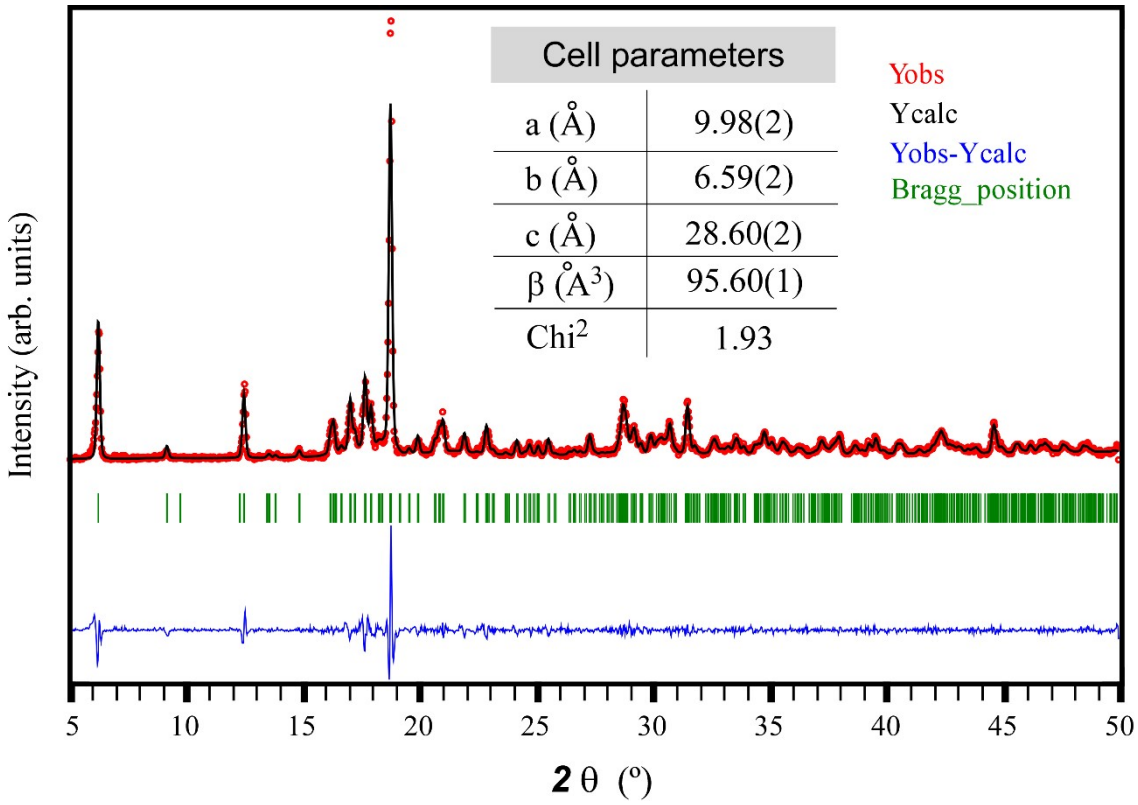

Figure S5. Full profile pattern matching analysis of the PXRD of $\mathbf{2_{Nd}}$.

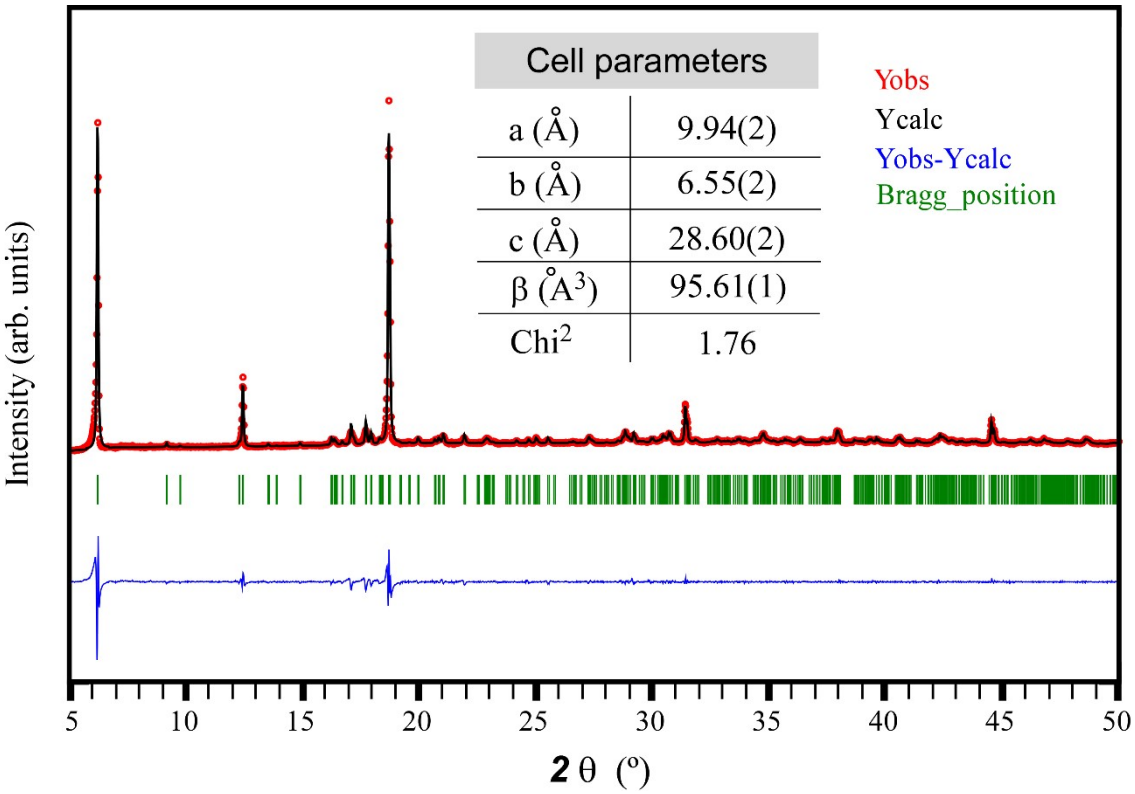

Figure S6. Full profile pattern matching analysis of the PXRD of $\mathbf{3}_{\mathbf{Eu}}$.

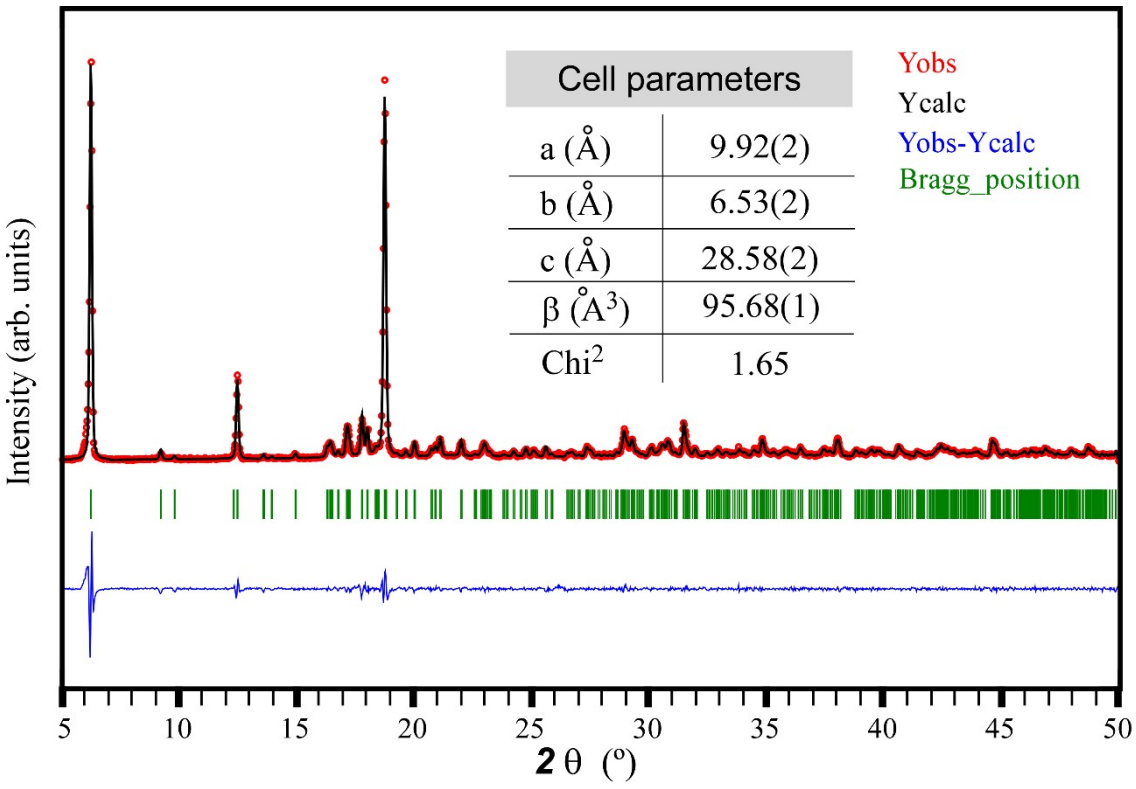

Figure S7. Full profile pattern matching analysis of the PXRD of $\mathbf{4}_{\mathbf{Gd}}$.

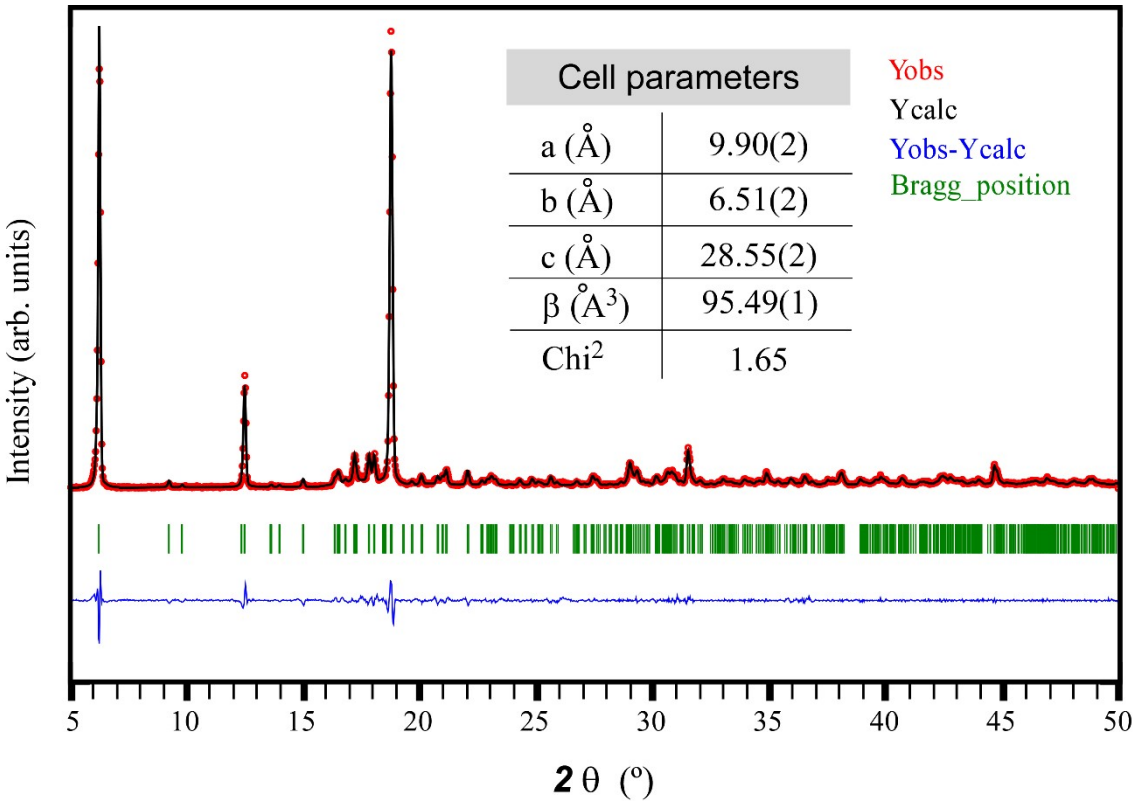

Figure S8. Full profile pattern matching analysis of the PXRD of $\mathbf{5}_{\mathbf{Tb}}$.

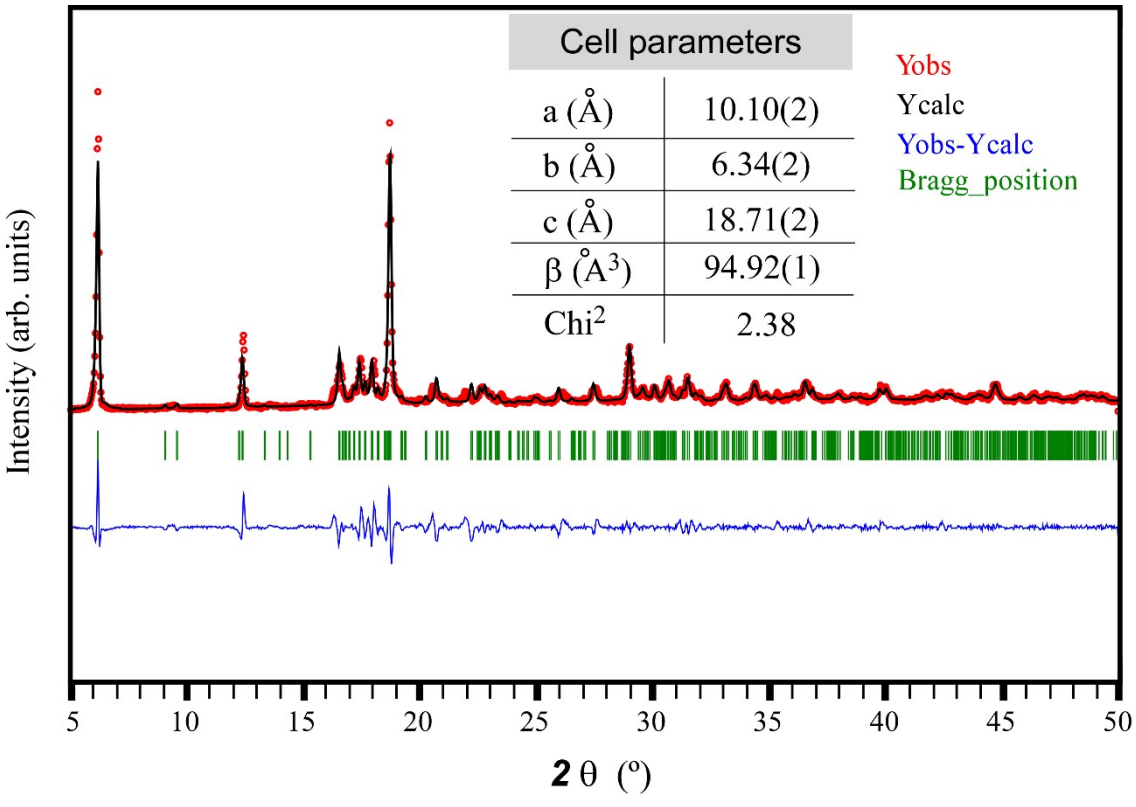

Figure S9. Full profile pattern matching analysis of the PXRD of $\mathbf{6}_{\mathbf{Dy}}$.

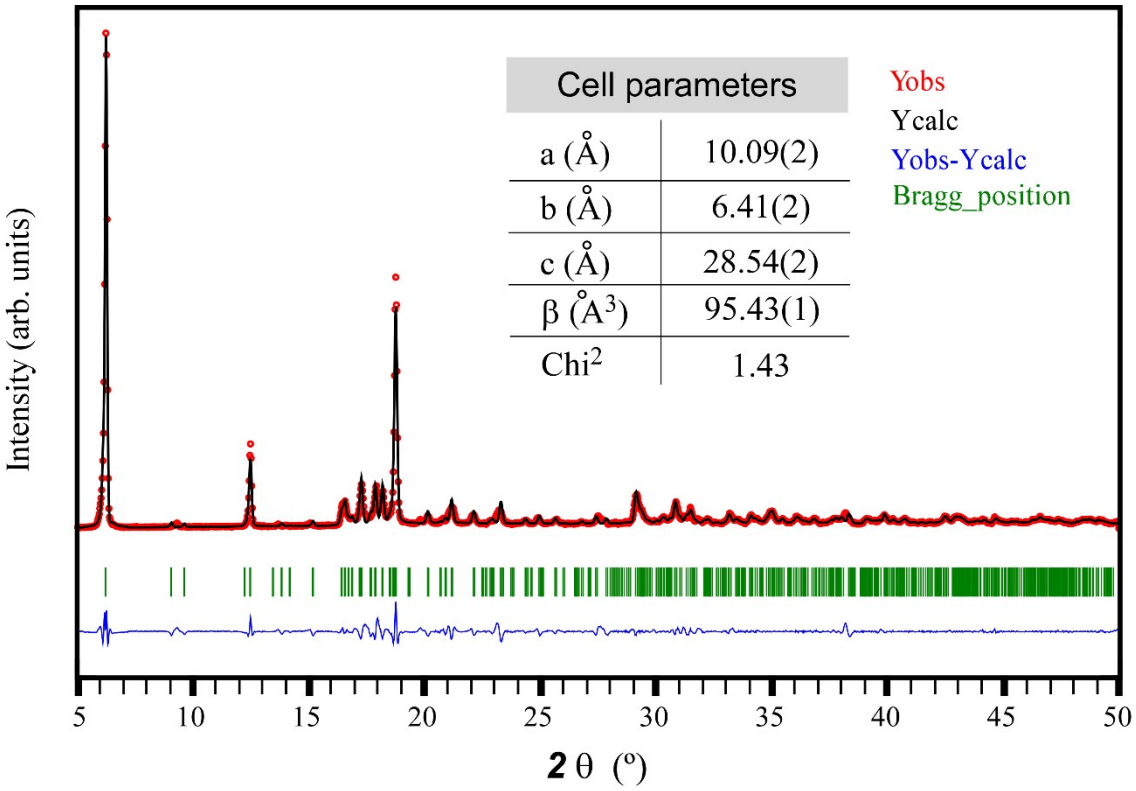

Figure S10. Full profile pattern matching analysis of the PXRD of $\mathbf{7}_{\mathbf{Er}}$.

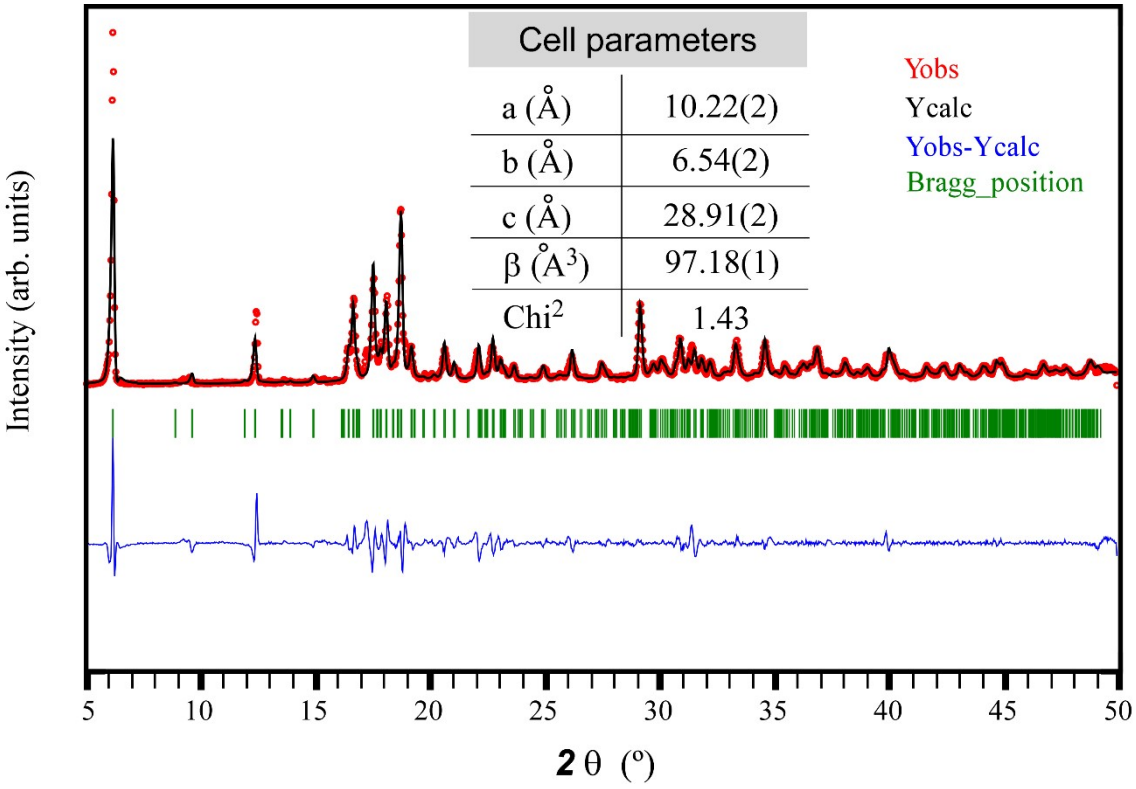

Figure S11. Full profile pattern matching analysis of the PXRD of $\mathbf{8}_{\mathbf{Yb}}$.

S5. Additional structural details.

Crystallographic data have been deposited with the Cambridge Crystallographic Data Center as supplementary publication with CCDC numbers 2456148-2456153. Copies of the data can be obtained free of charge on application to the Director, CCDC, 12 Union Road, Cambridge, CB2 1EZ, U.K. (Fax: +44-1223-335033; e-mail: deposit@ccdc.cam.ac.uk or http://www.ccdc.cam.ac.uk).

Table S3. Structural parameters (Å, °) of π-π interactions of compound $\mathbf{5}_{\mathbf{Tb}}$.[a]

Ring···Ring[b]	α	DC	β	DZ
1A–2B(i)	4.9(2)	3.919(2)	36.1	3.1292(17)
1A–2B(ii)	4.9(2)	3.500(2)	21.7	3.2878(17)
2B–1A(ii)	4.9(2)	3.500(2)	20.1	3.2520(17)
2B–1A(iii)	4.9(2)	3.919(2)	37.0	3.1672(17)

[a]Symmetry: (i) x, 1/2-y, -1/2+z; (ii) x, 1/2-y, 1/2+z. α: dihedral angle between mean planes of the rings (°), DC: distance between ring centroids (Å), β: angle between DC vector and normal to plane(I) (°), DZ: perpendicular distance of the centroids of the ring(I) on the plane of ring(II) (Å). [b] Rings: **1C**: N1C, C2C, C3C, C4C, C5C, C6C; **2C**: N10C, C9C, C8C, C7C, C12C, C11C.

S6. Continuous Shape Measurements (CShMs).

Table S4. CShMs for the coordination environment of compound $\mathbf{5}_{\mathbf{Tb}}$. The lowest values for each ion are shown in bold blue, indicating best fits.

Codes:

OP-8	1 D_{8h}	Octagon
HPY-8	2 C_{7v}	Heptagonal pyramid
HBPY-8	3 D_{6h}	Hexagonal bipyramid
CU-8	4 O_h	Cube
SAPR-8	5 D_{4d}	Square antiprism
TDD-8	6 D_{2d}	Triangular dodecahedron
JGBF-8	7 D_{2d}	Johnson gyrobifastigium J26
JETBPY-8	8 D_{3h}	Johnson elongated triangular bipyramid J14
JBTPR-8	9 C_{2v}	Biaugmented trigonal prism J50
BTPR-8	10 C_{2v}	Biaugmented trigonal prism
JSD-8	11 D_{2d}	Snub diphenoid J84
TT-8	12 Td	Triakis tetrahedron
ETBPY-8	13 D_{3h}	Elongated trigonal bipyramid

Structure [ML8]	OP-8	HPY-8	HBPY-8	CU-8	SAPR-8	TDD-8	JGBF-9
$\mathbf{5}_{\mathbf{Tb}}$ (Tb1)	30.931	24.214	16.808	10.143	2.337	**0.437**	12.923
$\mathbf{5}_{\mathbf{Tb}}$ (Tb2)	30.972	24.131	13.571	6.241	**0.864**	1.684	15.529

Structure [ML8]	JETBPY-8	JBTPR-8	BTPR-8	JSD-8	TT-8	ETBPY-8
$\mathbf{5}_{\mathbf{Tb}}$ (Tb1)	29.601	2.486	2.331	1.944	10.499	25.473
$\mathbf{5}_{\mathbf{Tb}}$ (Tb2)	29.306	3.252	2.543	5.293	7.129	24.655

S7. Gravimetric experiment to study solvent loss under high vacuum.

As mentioned in the "Framework response dynamics to temperature and variable pressure" of the manuscript, a simple experiment was performed in order to characterize the solvent loss taking place during pressurization of the sample under high vacuum of ca. 10^{-5} mbar. For this experiment, a sample of compound $\mathbf{2_{Nd}}$ was used as a representative of the family of isostructural compounds.

In this experiment, fresh sample of $\mathbf{2_{Nd}}$ was placed on an adsorption cell and weighed to calculate the exact mass of starting sample. The flask was then placed and adjusted into the outgassing station of a Autosorb iQ Quantachrome Instruments analyzer. The sample was kept under high vacuum for 72 hours at 25 ºC. After the experiment, the closed flask was again weighed to calculate the exact mass loss occurring during the experiment. The gravimetric data are shown in Table S5.

Table S5. Gravimetric data for compound $\mathbf{2_{Nd}}$ collected during the vacuum experiment.

Stage	Mass	Mass loss	Δm(%)	$\Delta m(\%)_{theo}$
Initial	0.1657	0.0113	6.82	6.27 ($-4H_2O$)
Final	0.1544			

Codes: T_i: initial temperature; T_f: final temperature; T_{max}: temperature of the DTA signal maximum for each step; $\Sigma\Delta m$: released mass summatory; ΔH: process type; $\Sigma\Delta m_{theo}$: theoretically released mass summatory; Δm_{theo}: theoretically released mass in each step. [a] This percentage corresponds to the mass of the final product (%).

As a consequence of the dehydration, coordination environments of both metal atoms are significantly affected. Mainly, polyhedron of Y1 is strongly affected because the reduction of coordination index from 8 to 6 is accompanied of substantial decrease in the polyhedron symmetry (from less distorted triangular dodecahedron symmetry (S_{TDD} = 0.453) to highly distorted pseudo-octahedron (S_{OC} = 1.744)). To a lesser extent, Y2 centre also decreases its symmetry (from 0.886 to 1.208 for the SAPR shape).

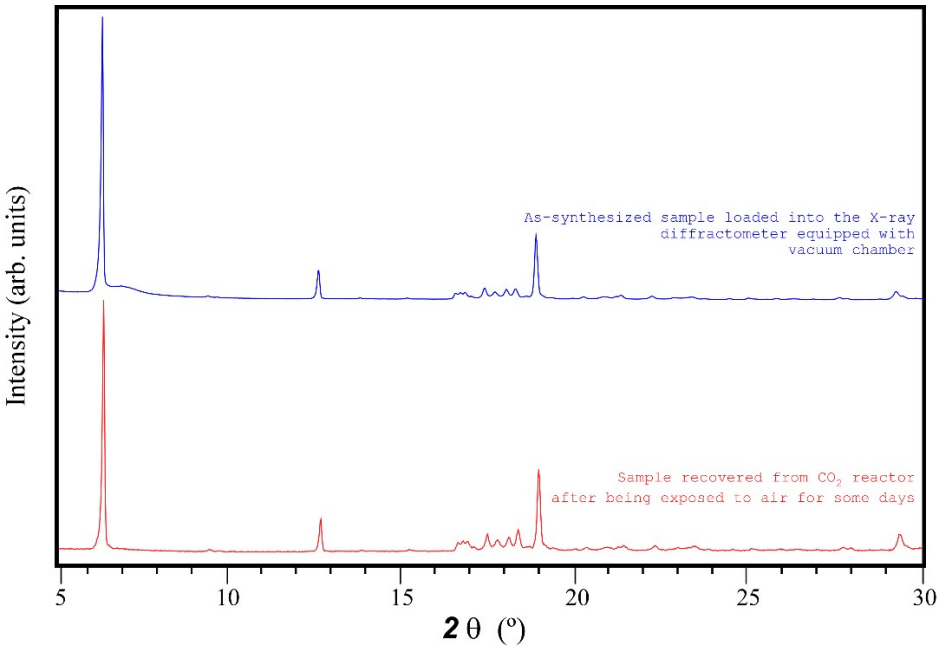

Figure S12. Reversibility of compound $\mathbf{7_{Er}}$ confirmed by comparison of the PXRD data acquired under high-pressure and after the experiment with sample exposed to air for some hours.

S8. Additional information about gas pressure experiments.

All samples of compound $\mathbf{3_{Eu}}$ employed for studying structural changes by in situ gas (air/Ar) pressure PXRD was mixed and placed in a reactor at 10 bar of CO_2 gas for 16 h. The powder recovered from this experiment exhibited a slightly beige/pinkish coloration, although it returned to white within a few minutes by the time the photograph was taken. This colour change resembles that habitually observed for other compounds during thermal dehydration, which is probably related with the fully dehydrated compound (of $\{[Eu_2(2onic)_4](ClO_4)_2\}_n$ formula) under these harsh conditions. The fact that this colour change is not observed for the sample under soft (2 bar) conditions and that the white colour is rapidly recovered on this occasion, in contrast to the slow recovery observed for the partially dehydrated compound (white coloured as the original compound) point to that hypothesis. Our best efforts in order to better characterize this other compound by PXRD were unfruitful as the time required to remove the sample from the reactor, bring it to the X-ray setup, and begin measurements is not sufficiently short. Instead, the diffractograms collected confirmed the metastable partially dehydrated phase associated to the $\{[Eu_2(2onic)_4(H_2O)_2](ClO_4)_2\}_n$ formula. Moreover, no higher pressures than 2 bar could be reached within the PXRD instrument, which is the maximum generated by a flow of 100 mL/min.

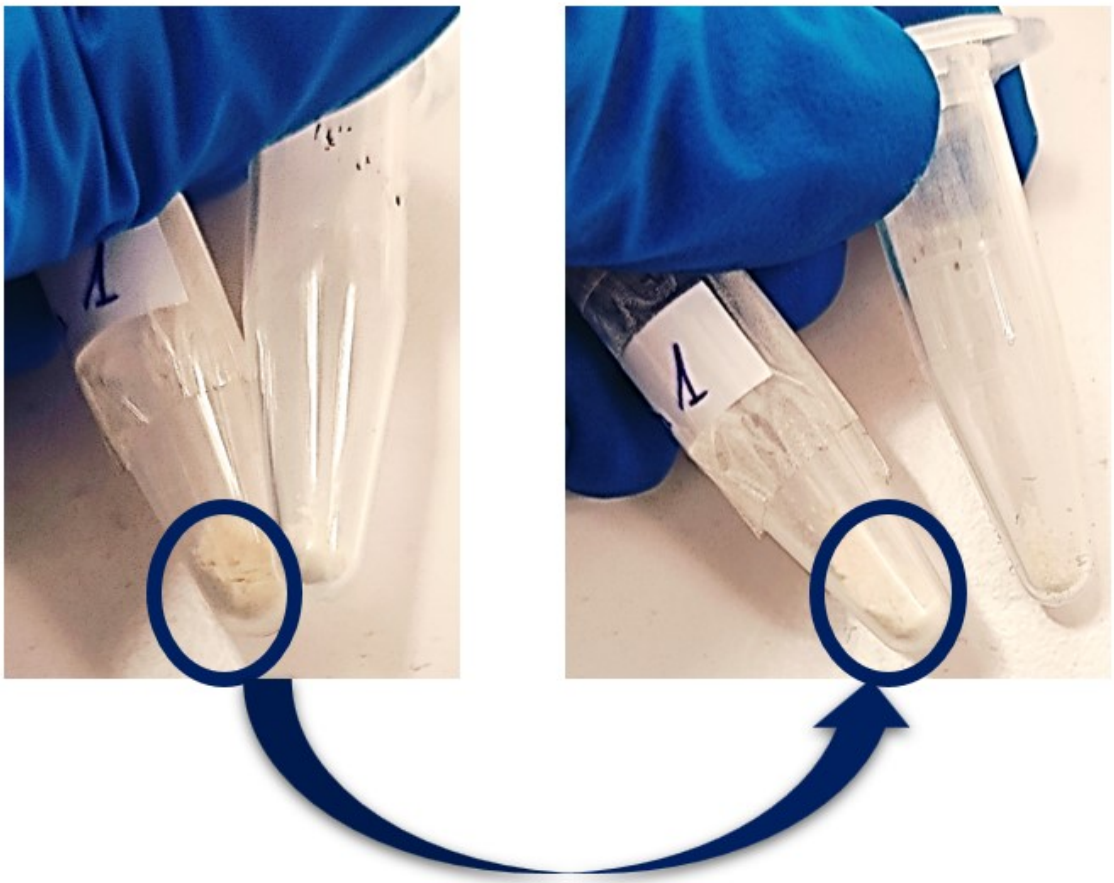

Figure S13. Reversible colour change appreciated for the fully and partially dehydrated phases of compound $\mathbf{3_{Eu}}$.

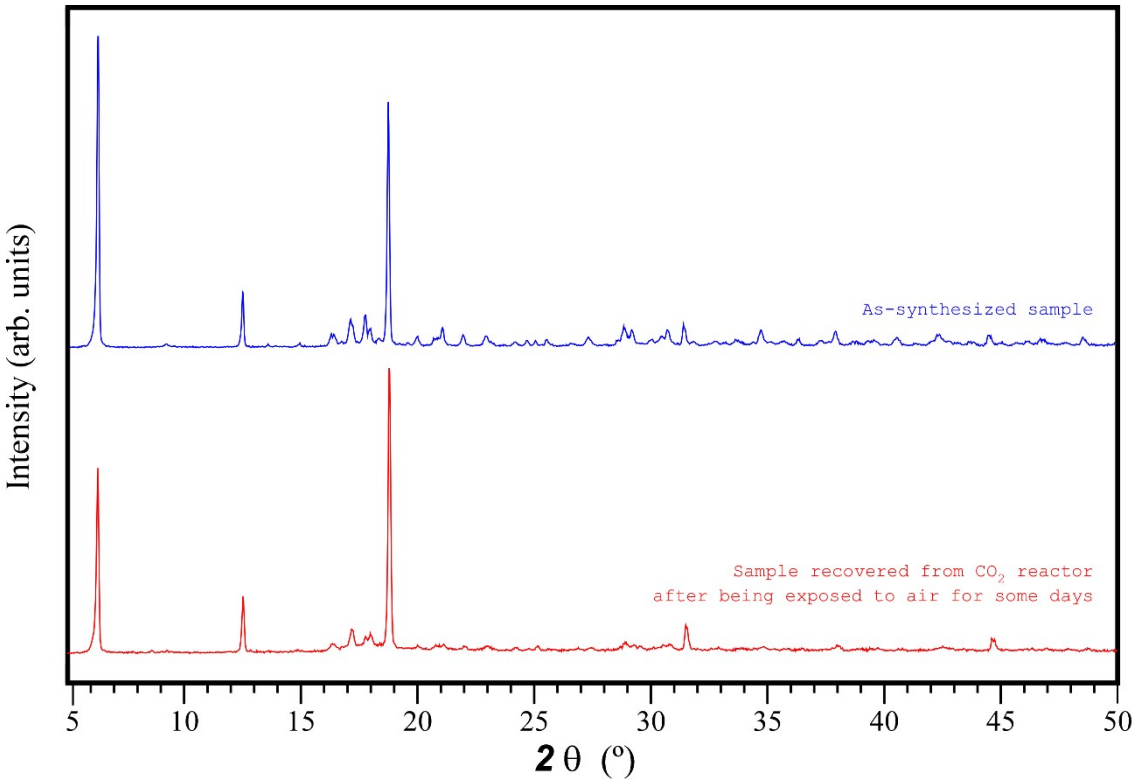

Figure S14. Reversibility of the high-pressure CO_2 triggered dehydration/spontaneous rehydration of compound $\mathbf{3_{Eu}}$.

S9. Solid-state absorption spectra.

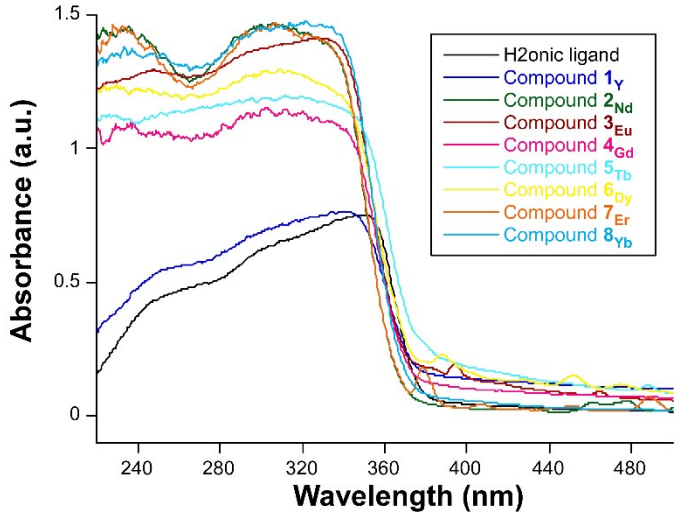

Figure S15. Solid-state UV-Vis absorption spectrum of the H2onic ligand and compounds $\mathbf{1_Y}$-$\mathbf{8_{Yb}}$.

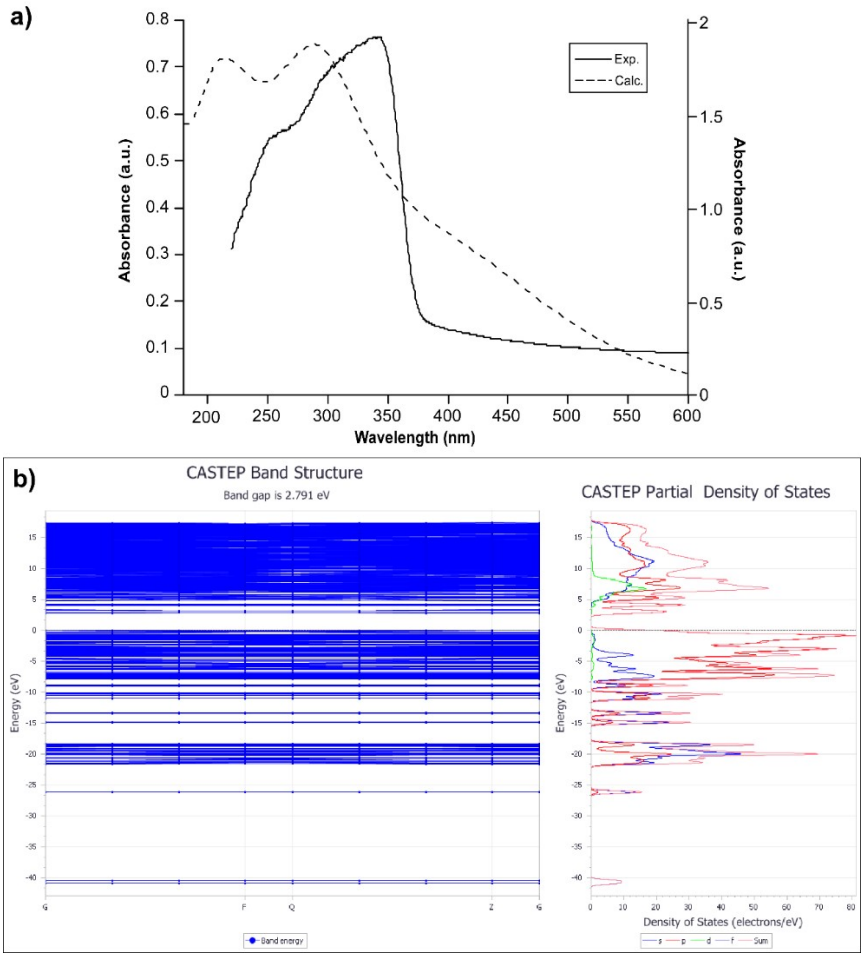

Figure S16. Results from the PDOS calculation for compound $\mathbf{1_Y}$ in the form of: **a)** comparative UV/Vis absorption spectrum (with experimental solid-state spectrum) and **b)** energy diagrams showing the band structure, band gap and main representative contributions to PDOS.

The diffuse reflectance spectrum of $\mathbf{1_Y}$ was converted into Tauc plot by applying the Kubelka-Munk function and employed to estimate the optical band gap of that compound.

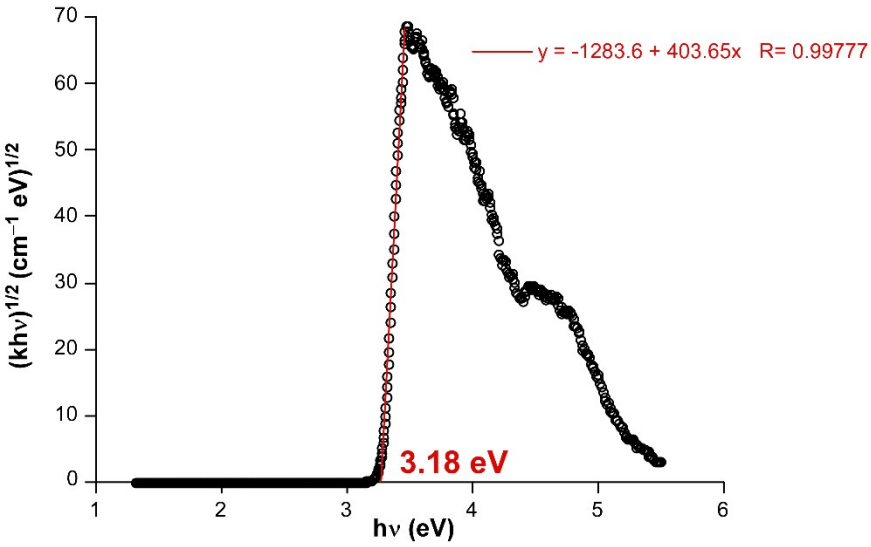

Figure S17. Diffuse reflectance data for compound $\mathbf{1_Y}$ plotted as Tauc plot showing the estimated band gap.

S10. Photoluminescence measurements in solid state in open atmosphere.

Below are shown the results gathered for the photoluminescence properties of the compounds in solid state:

H2onic ligand and compound ***4***$_{Gd}$ *at variable temperature:*

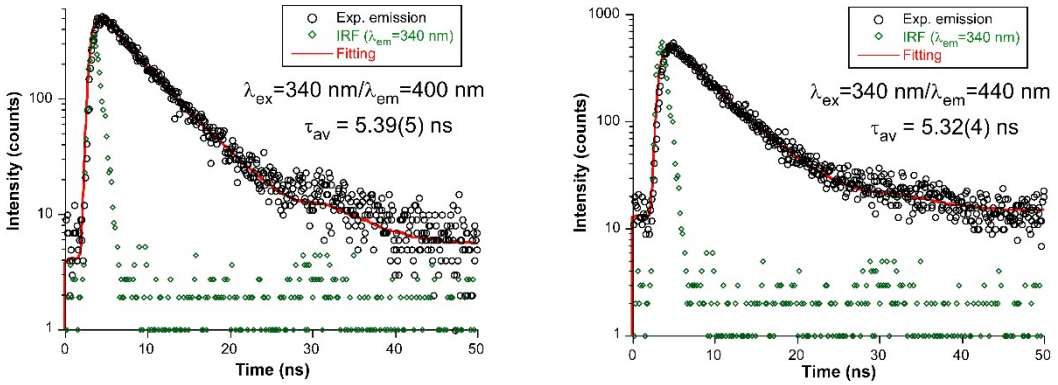

(a) **(b)**

Figure S18. Decay curves of free H2onic ligand sample taken at room temperature under UV LED illumination (λ_{ex} = 340 nm) for: **(a)** λ_{em} = 400 nm and **(b)** λ_{em} = 440 nm.

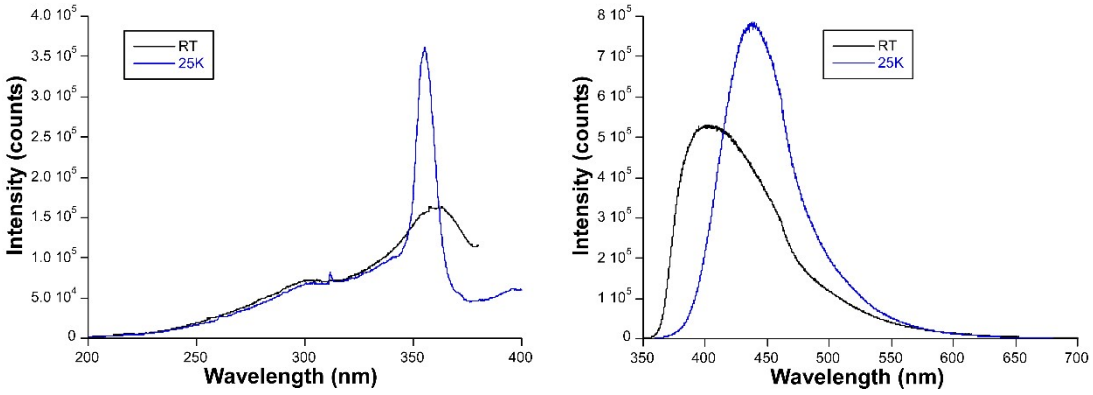

Figure S19. Comparative excitation and emission spectra of the free H2onic ligand sample taken at variable temperature at λ_{em} = 387 nm and λ_{ex} = 325 nm.

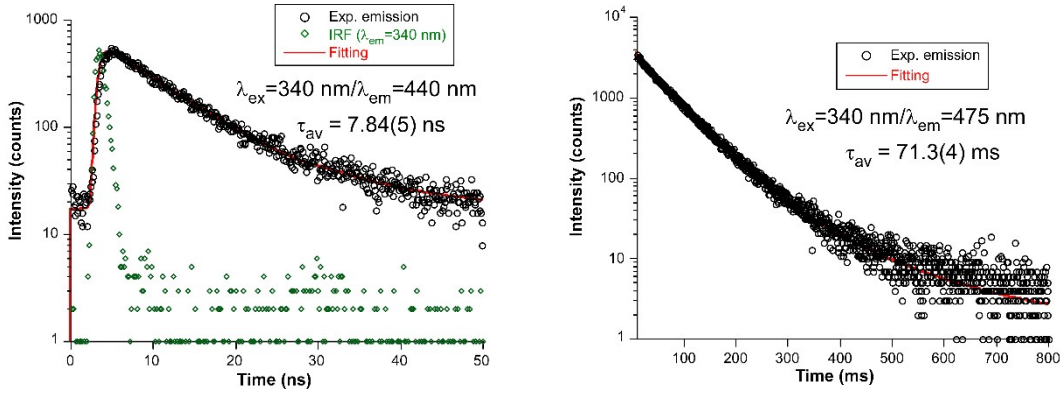

(a) **(b)**

Figure S20. Decay curves of free H2onic ligand sample taken at low temperature under variable pulsed lamp illumination (λ_{ex} = 340 nm) for: **(a)** λ_{em} = 440 nm and **(b)** λ_{em} = 475 nm.

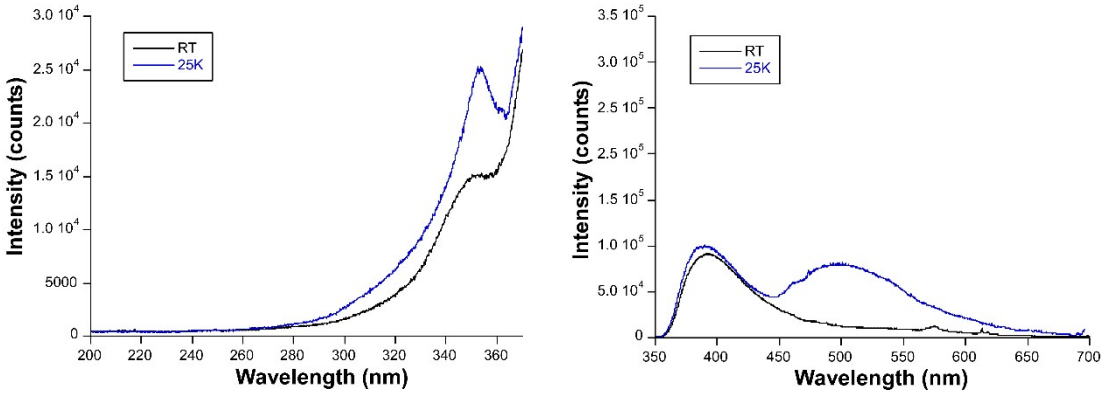

(a) **(b)**

Figure S21. Comparative excitation and emission spectra of compound $\mathbf{4_{Gd}}$ taken at variable temperature with: **(a)** λ_{em} = 387 nm and **(b)** λ_{ex} = 325 nm.

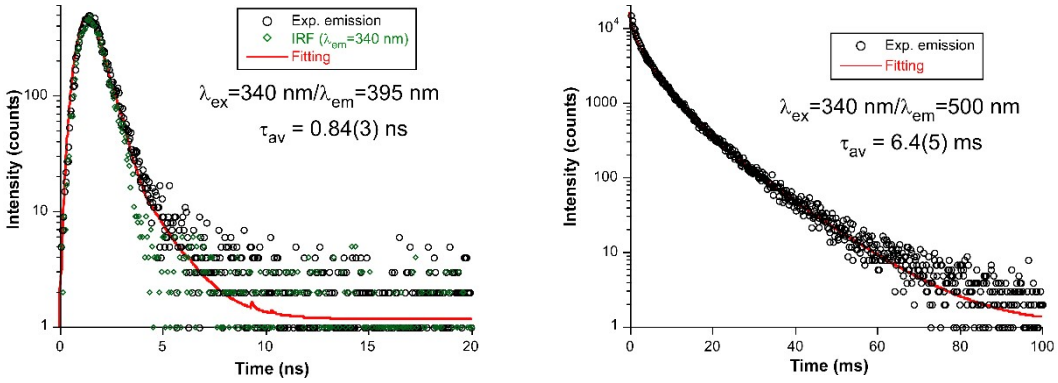

(a) **(b)**

Figure S22. Decay curves of compound $\mathbf{4_{Gd}}$ recorded at low temperature under LED pulsed lamp illumination (λ_{ex} = 340 nm) for: **(a)** λ_{em} = 440 nm and **(b)** λ_{em} = 475 nm.

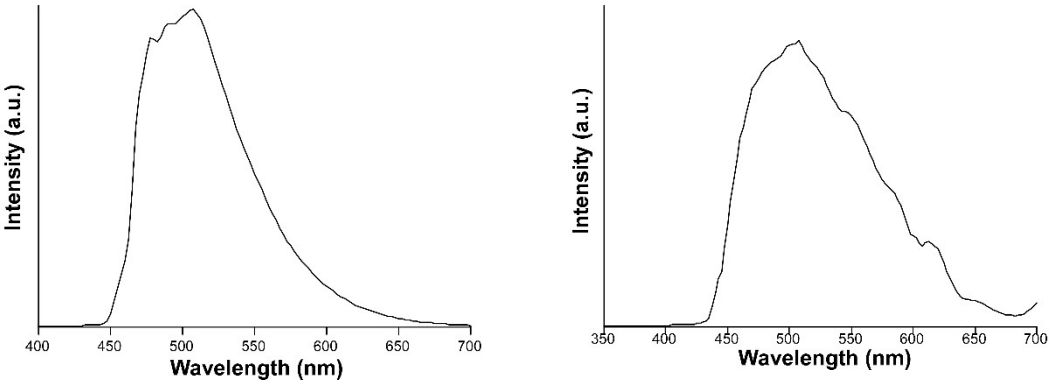

(a) **(b)**

Figure S23. Time-resolved emission spectra of **(a)** free H2onic ligand and **(b)** compound $\mathbf{4_{Gd}}$ recorded at t = 3 ms (after the lamp pulse).

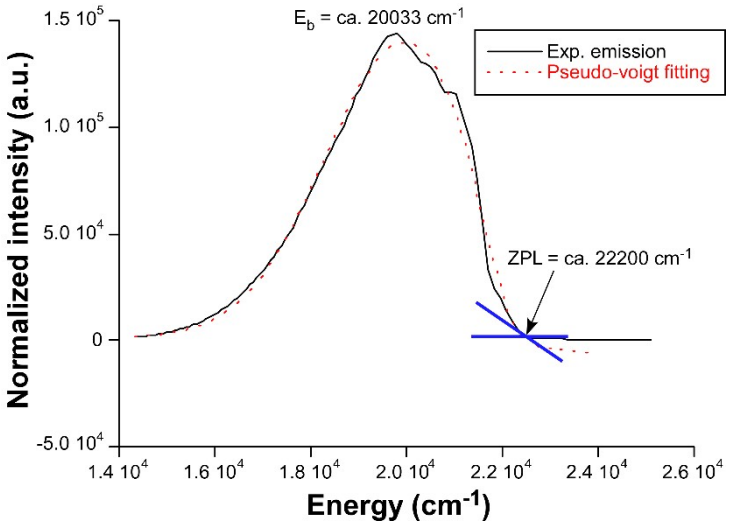

Figure S24. Processed phosphorescence emission spectrum for free H2onic ligand sample recorded at t = 3 ms (after the lamp pulse) showing the best gaussian fitting to estimate the barycentre and zero-phonon line.

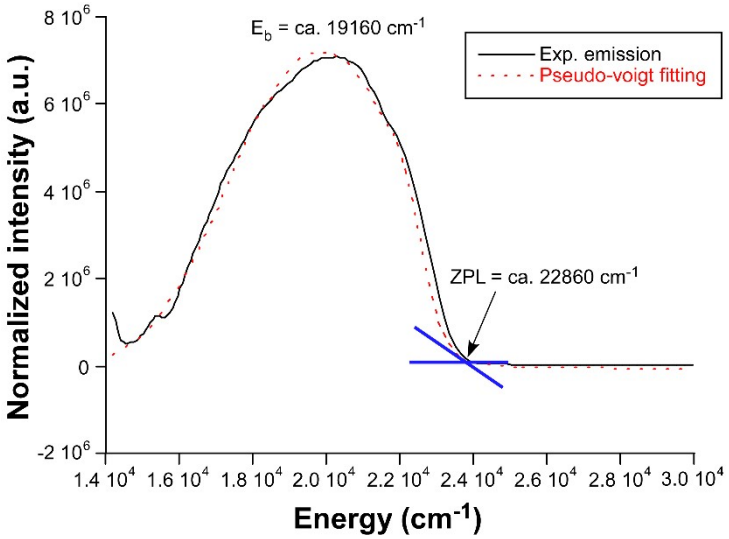

Figure S25. Processed phosphorescence emission spectrum for compound $\mathbf{4_{Gd}}$ recorded at t = 3 ms (after the lamp pulse) showing the best gaussian fitting to estimate the barycentre and zero-phonon line.

Compound $\mathbf{3_{Eu}}$ at room temperature:

As mentioned in the manuscript, the emission spectrum of compound $\mathbf{3_{Eu}}$ at room temperature and open atmosphere (in the absence of vacuum) presents four groups of signals peaking at 592, 613, 651 and 699 nm, which are assigned to $^7F_J \leftarrow {}^5D_0$ transitions (where J = 1 2, 3 and 4). Among these bands, the third signal (attributed to the hypersensitive $^7F_2 \leftarrow {}^5D_0$ transition) dominates the spectrum with an integrated intensity of almost six times that of the $^7F_1 \leftarrow {}^5D_0$ (286693 vs 50280 counts), a fact that is in agreement with the low symmetry of the Eu sites in the crystal structure. On its part, the excitation spectrum shows a wide peaking at 380 nm assigned to the ligand-centred π-π* transitions in addition to many narrow intense bands assigned to intra-Eu(III) f-f transitions (see assignation below).

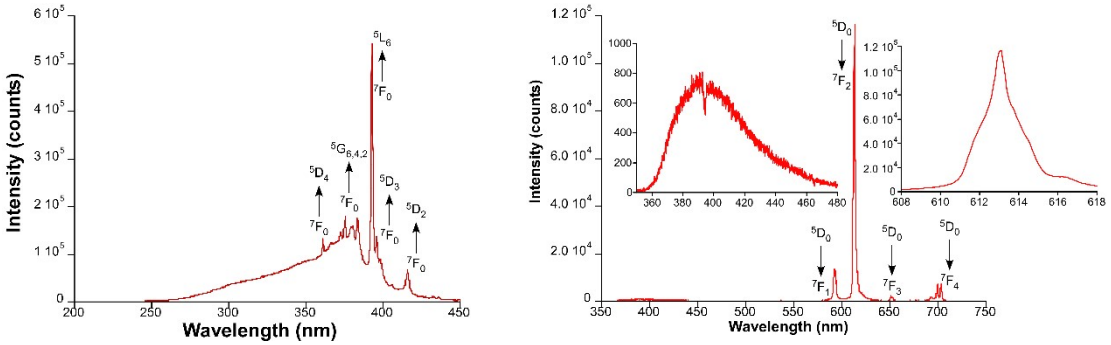

Figure S26. Excitation and emission spectra of compound $\mathbf{3_{Eu}}$ taken at room temperature at open atmosphere at λ_{em} = 612 nm and λ_{ex} = 325 nm showing the assignation for all bands.

Below are shown the decay curves collected for compound $\mathbf{3_{Eu}}$ at room temperature recorded with a μF900 pulsed lamp and different excitation wavelengths. Lifetimes were estimated from best fitting using the following expression:

$$I_t = A_0 + A_1\exp(-t/\tau_1) \quad \text{(eq. 1)}$$

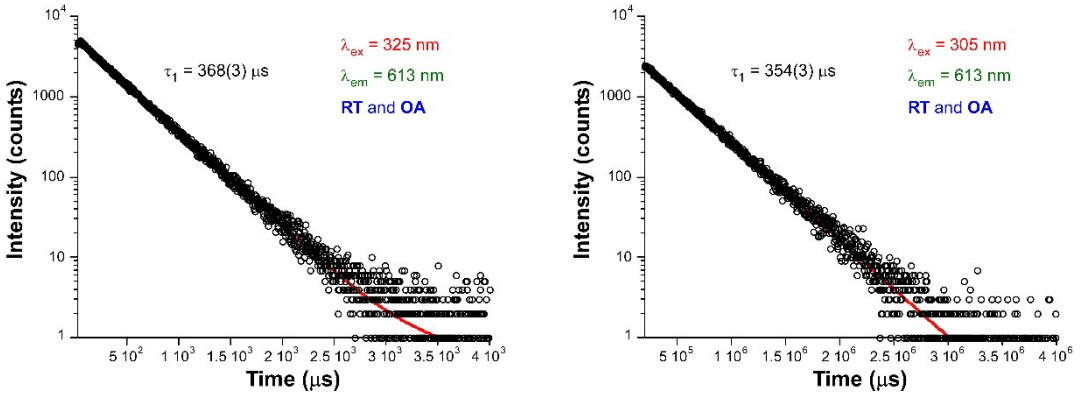

Figure S27. Decay curves of compound $\mathbf{3_{Eu}}$ taken at room temperature and open atmosphere (OA).

Compound $\mathbf{5_{Tb}}$ at room temperature:

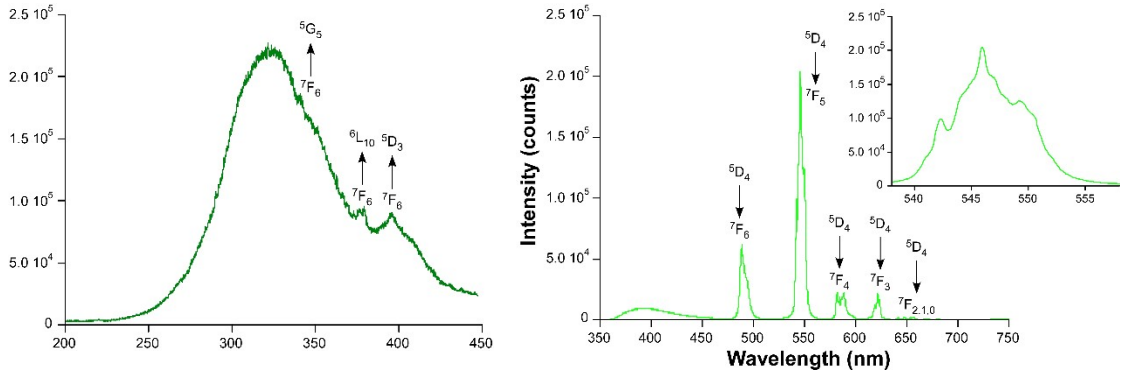

Figure S28. Excitation and emission spectra of compound $\mathbf{5_{Tb}}$ taken at room temperature at open atmosphere at λ_{em} = 546 nm and λ_{ex} = 325 nm showing the assignation for all bands. Inset on the emission spectrum (right) shows the augmented signal of the hypersensitive ($^7F_5 \leftarrow {}^5D_4$ transition) band.

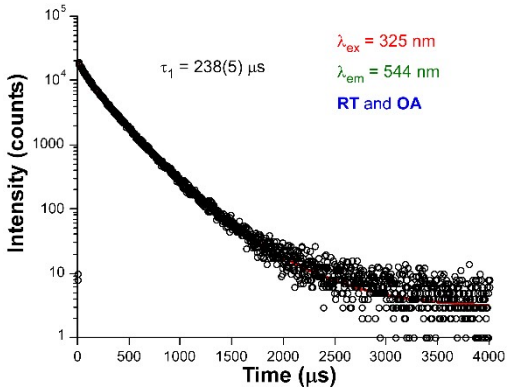

Figure S29. Decay curve of compound $\mathbf{5_{Tb}}$ taken at room temperature and open atmosphere (OA).

S11. Photoluminescence properties of NIR emitting compounds.

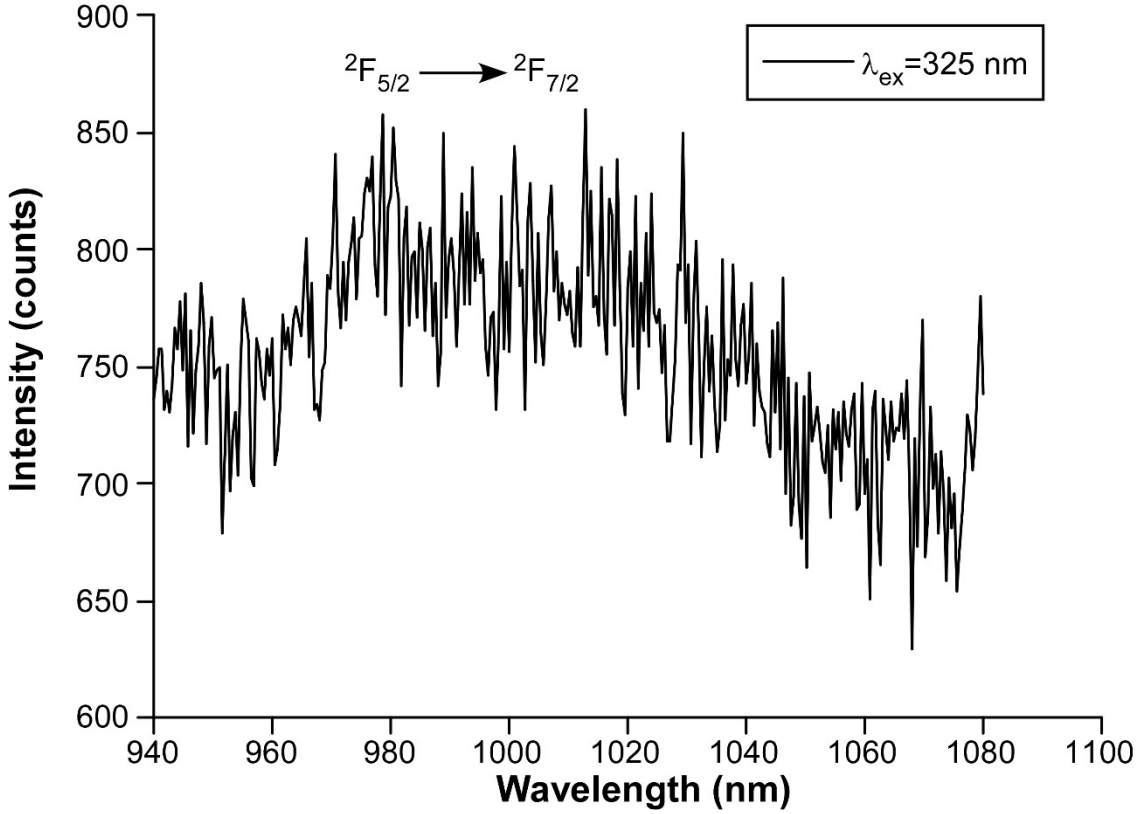

Figure S30. Emission spectrum of compound $\mathbf{8_{Yb}}$ taken at room temperature.

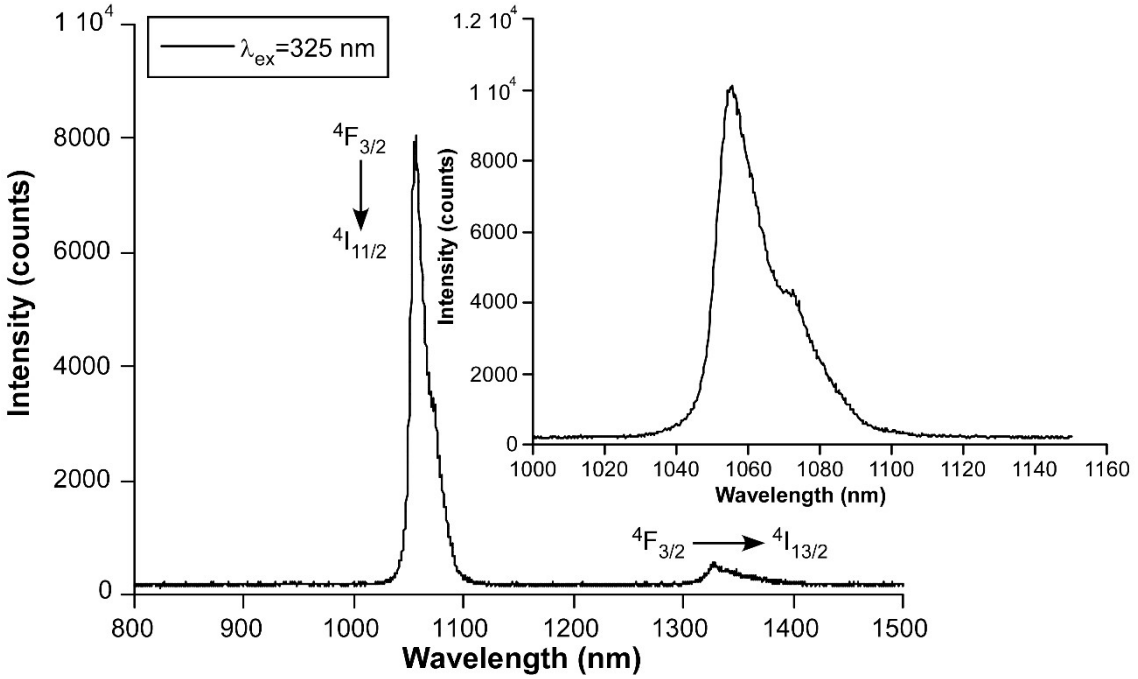

Figure S31. Emission spectrum of compound $\mathbf{2_{Nd}}$ taken at low temperature (25 K).

S12. Vacuum-induced modulation of PL properties of visible emitters.

When the vacuum system is turned on and the sample of $\mathbf{3}_{\mathbf{Eu}}$, placed in a cryostat, is purged, the compound experiences flexible dynamics as already described in section 3. In addition to the expected progressive increase in the emission intensity of the main characteristic intraionic bands, the spectrum reveals that, when high vacuum is achieved, the hypersensitive multiplet is fully resolved into narrow bands while some previously imperceptible peaks at ca. 618 and 625 nm are now visible. These changes are related to changes observed in the excitation spectrum recorded under these conditions, in which the ligand-centred excitation band is shown to be greatly increased.

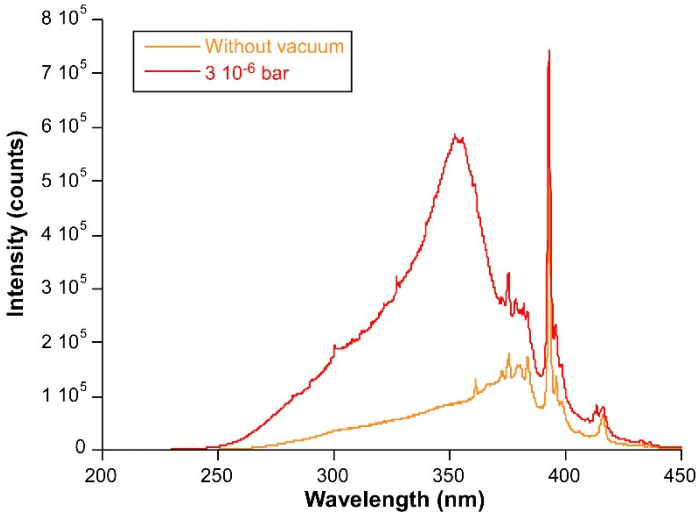

Figure S32. Comparative excitation spectra of compound $\mathbf{3}_{\mathbf{Eu}}$ taken at room temperature under open atmosphere (OA) and under high vacuum (compound $\mathbf{3}_{\mathbf{Eu}}^{\mathbf{UV}}$).

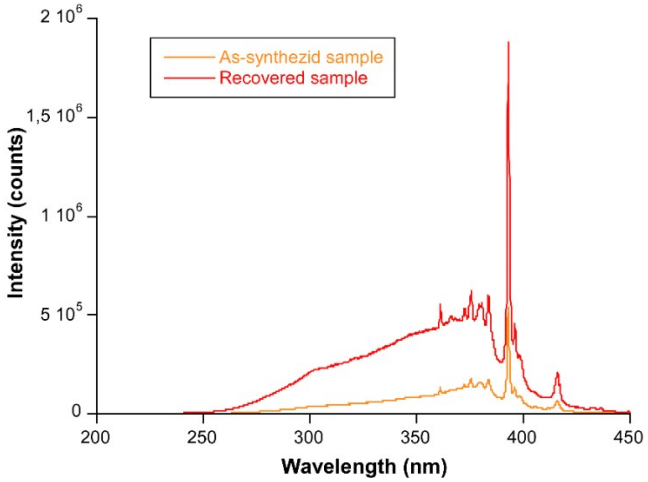

Figure S33. Comparative excitation spectra of compound $\mathbf{3}_{\mathbf{Eu}}$ taken at room temperature under open atmosphere (OA) before (as-synthesized sample) and after applying vacuum (recovered sample), to show the reversibility of the vacuum-triggered transformation.

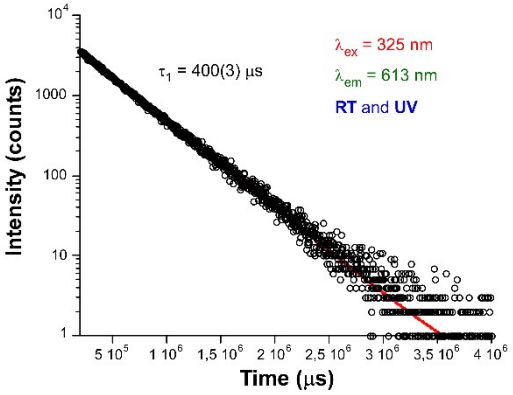

Figure S34. Decay curve of compound $\mathbf{3_{Eu}}$ taken under vacuum (UV) at room temperature.

A similar effect with the vacuum is also noticed for the rest of compounds, although the changes are less important:

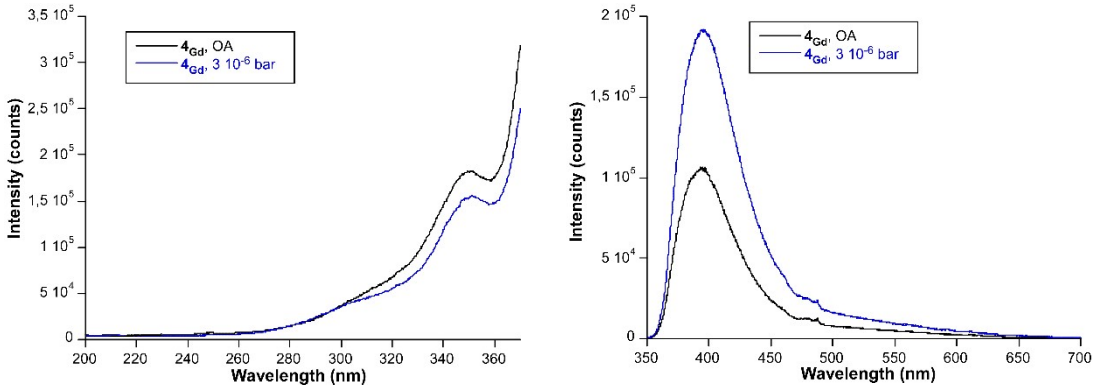

Figure S35. Comparative excitation (λ_{em}=393 nm) and emission (λ_{ex}=325 nm) spectra of compound $\mathbf{4_{Gd}}$ taken at room temperature under open atmosphere (OA) and under high vacuum.

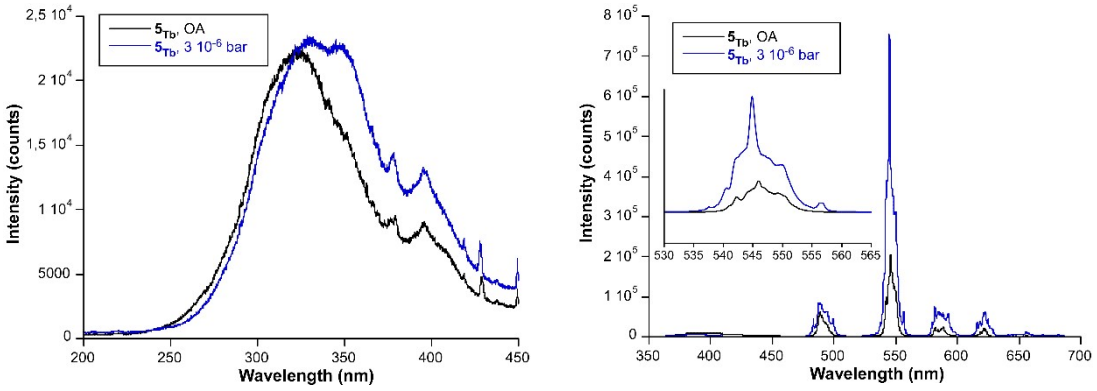

Figure S36. Comparative excitation (λ_{em}=393 nm) and emission (λ_{ex}=325 nm) spectra of compound $\mathbf{5_{Tb}}$ taken at room temperature under open atmosphere (OA) and under high vacuum.

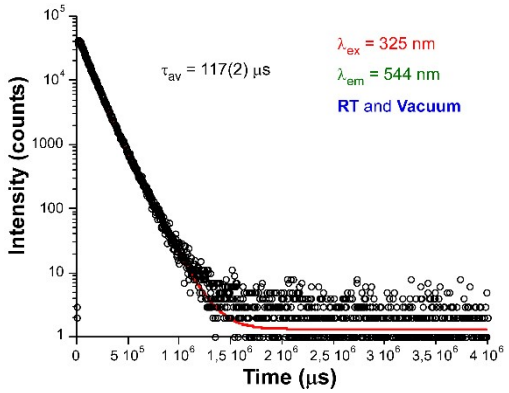

Figure S37. Decay curve of compound $\mathbf{5_{Tb}}$ taken under vacuum (UV) at room temperature.

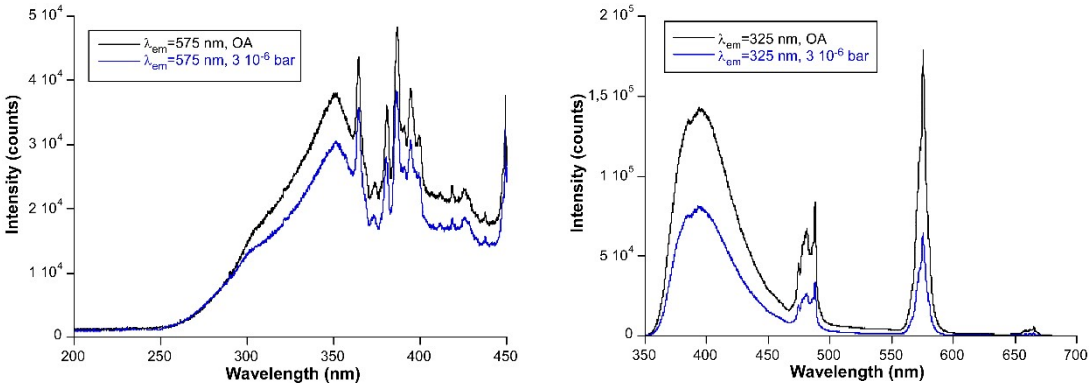

Figure S38. Comparative excitation (λ_{em}=578 nm) and emission (λ_{ex}=325 nm) spectra of compound $\mathbf{6_{Dy}}$ taken at room temperature under open atmosphere (OA) and under high vacuum.

S13. Reversible luminescence of $\mathbf{3_{Eu}}$ after gas-pressurized measurements.

With the aim of verifying the reversibility of the pressurized samples, the routine measurements of the excitation and emission spectra as well as decay curves were repeated on the sample employed for those experiments.

The variable-pressure experiments, briefly, imply introducing the sample into a reactor at 10 bar of CO_2 gas, which is shown to promote framework breathing guided by the partial dehydration occurring under those conditions. After leaving the sample for some days exposed to air, the following measurements were performed:

Measurements at room temperature and open atmosphere:

The samples were analyzed as collected from pressurization experiments and directly mounted into the sample holder of the spectrometer to be measured:

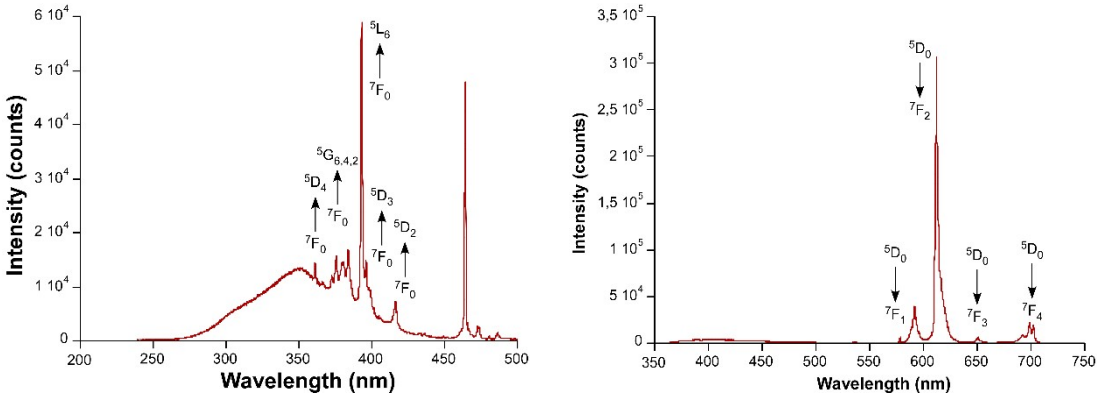

Figure S39. Excitation and emission spectra of compound $\mathbf{3_{Eu}}$ taken at room temperature and open atmosphere after the previously gas-pressurization experiment.

As observed, excitation spectrum reproduces that shown by pristine compound at these conditions.

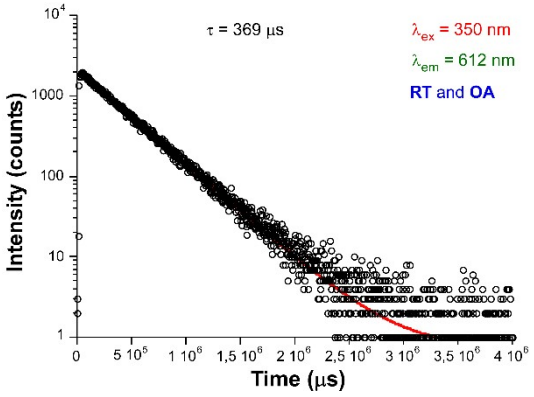

Figure S40. Decay curve and best-fitting to estimate the lifetime of previously pressurized $\mathbf{3_{Eu}}$ taken at room temperature and open atmosphere (OA).

As observed, all data reproduce well those collected for the pristine compound at the same conditions confirming the reversibility of the process. In particular, this lifetime of 369 μs concords perfectly well with that measured for the pristine compound (368 μs).

Measurements at room temperature under vacuum:

To double check the reversibility of the process, another part of the sample was mounted in the spectrometer within the cryostat and high vacuum was applied to it before collecting the data.

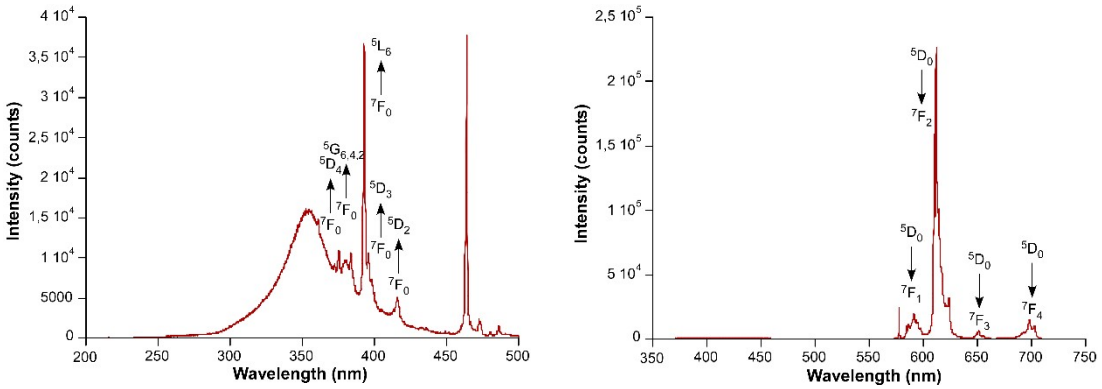

Figure S41. Excitation and emission spectra of compound $\mathbf{3_{Eu}}$ taken at room temperature under high vacuum for the previously pressurized sample.

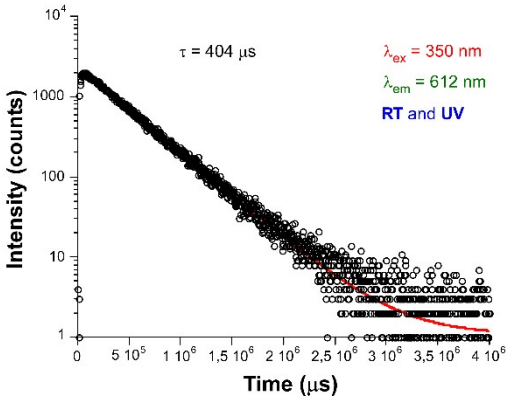

Figure S42. Decay curve and best-fitting to estimate the lifetime of previously pressurized $\mathbf{3_{Eu}}$ taken at room temperature under high vacuum (UV).

Once again, vacuum-triggered partial dehydration of the sample leads to two main spectroscopic effects: i) relative increase in the intensity of the ligand-centred excitation band compared to intraionic bands, suggesting enhanced antennae effect; and ii) increase of emission lifetime to 404 μs, which again reproduces the value measured for the pristine compound under vacuum (400 μs).

Reversibility of the dehydration at room temperature:

The reversibility of the process, i.e. the rehydration of the compound is confirmed in the sample when it is left for 1 day exposed to open atmosphere, because both the excitation/emission spectra and lifetime of the initial material are reproduced:

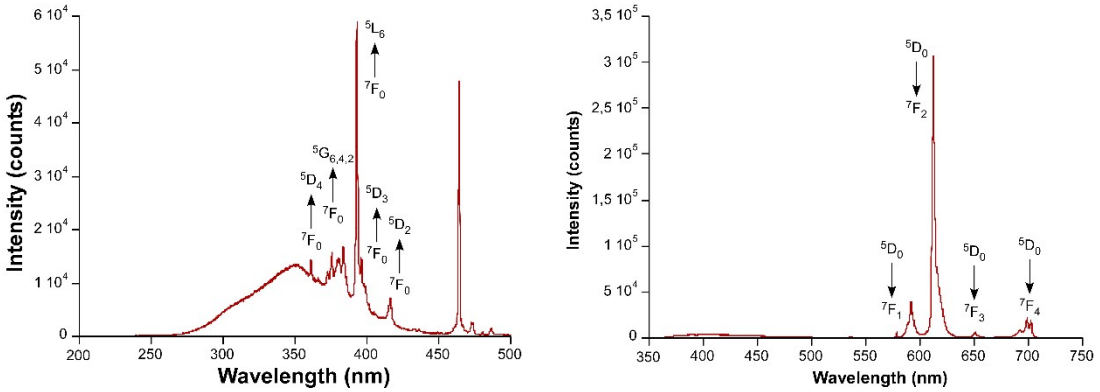

Figure S43. Excitation and emission spectra of compound $\mathbf{3_{Eu}}$ taken at room temperature after one day of exposure to open atmosphere.

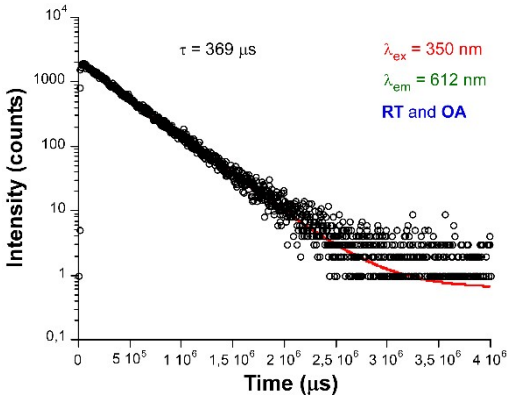

Figure S44. Decay curve and best-fitting to estimate the lifetime of previously pressurized $\mathbf{3_{Eu}}$ taken at room temperature after one day of exposure to open atmosphere.

S14. Comparative XPS analysis on pristine and gas-pressurized compound $\mathbf{3_{Eu}}$.

X-ray photoelectron spectroscopy (XPS) measurements were performed on a Versaprobe III Physical Electronics (ULVAC) system equipped with monochromatic radiation (Al Kα = 1486.7 eV). An initial analysis was carried out to determine the elements present (wide scan: step energy 0.2 eV, pass energy 224 eV) and detailed analyses were carried out on the detected elements (detail scan: step energy 0.05 eV, pass energy 27 eV, time per step 20 ms) with an electron exit angle of 45°. The spectrometer was previously calibrated with Ag (Ag 3d5/2, 368.26 eV). The spectra for the three samples were fitted with CasaXPS 2.3.26 software, which models contributions after a subtraction from the background (Shirley).

To further confirm the reversibility of the pressure-induced rehydration of the samples by simply exposing them to open atmosphere, which forces the spontaneous rehydration of the material and reverts the structure back to the initial stage, both the pristine sample and the sample recovered from gas-pressurization experiments were analyzed with this technique. However, taking into account that the results of this technique are only representative for the composition of the surface of the particles, it may be concluded that, overall, there is a good agreement of the relative atomic amounts of the elements present and, most importantly, that low deviations relative amounts between ligand's elements-to-Eu ratios are found with respect to the formula unit of compound $\mathbf{3_{Eu}}$. In particular, the O amount in the sample is remarkably lower than the expected for the formula unit (O/Eu close to 10 and thus lower than 13, as expected), as usually observed for previous analyses on similar metal-organic materials with this technique, which suggests that the absence of water molecules in the particles' surface is not related to defects on the solid.[2,3] Overall, the very similar ratios found for both samples can be taken as an undoubted result to conclude about the reversibility of the process.

Table S6. Main results from the XPS analysis performed on pristine sample and sample recovered from gas-pressurization experiments of compound $\mathbf{3_{Eu}}$.

Element	Atomic relative amount (%)		Atomic relative ratios			
	3_{Eu}	3_{Eu} (after gas-pres.)	Ratio	Theo.	3_{Eu}	3_{Eu} (a. g-p)
C	47.3	48.2	C/Eu	12	12.6	13.4
O	37.9	37.5	O/Eu	13	10.1	10.4
N	7.4	7.2	N/Eu	2	2.0	2.0
Cl	3.6	3.5	Cl/Eu	1	1.0	1.0
Eu	3.8	3.6	–	–	–	–

S15. Photoluminescence properties on the thermally dehydrated compounds.

As discussed in the manuscript, the polycrystalline samples of compounds $\mathbf{3}_{\mathbf{Eu}}$ and $\mathbf{5}_{\mathbf{Tb}}$ were submitted to thermal treatment by their heating at 215 °C for 3 h to bring the fully dehydrated products. As a consequence, the photoluminescence properties of these so-called $\mathbf{3}_{\mathbf{Eu}}^{\mathbf{D}}$ and $\mathbf{5}_{\mathbf{Tb}}^{\mathbf{D}}$ were studied at RT:

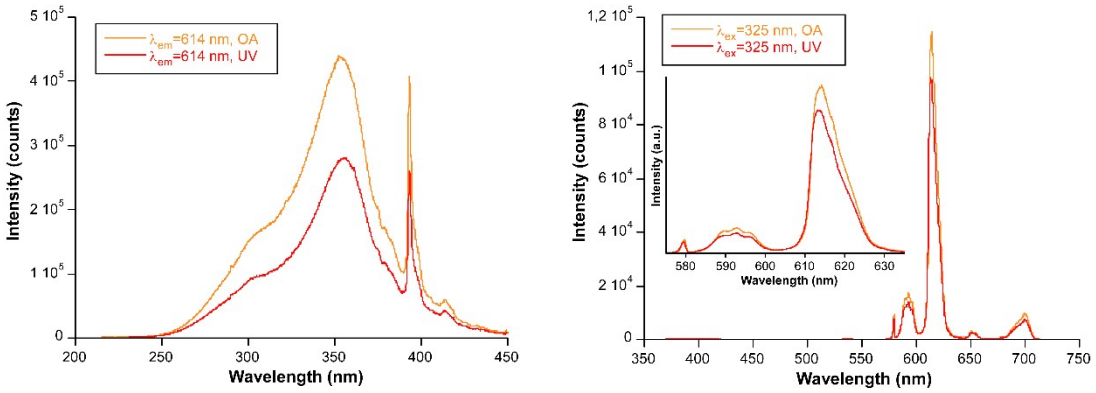

Figure S45. Excitation and emission spectra of compound $\mathbf{3}_{\mathbf{Eu}}^{\mathbf{D}}$ taken at room temperature under open atmosphere (OA) and under vacuum (UV).

The decay curves of the Eu-centred emission have been acquired under the same experimental setup used for the original $\mathbf{3}_{\mathbf{Eu}}$ compound for under open atmosphere (OA) and high vacuum (UV) situations, showing that applying vacuum slightly reduces the emission lifetime of the compound, as observed for the net emission intensity.

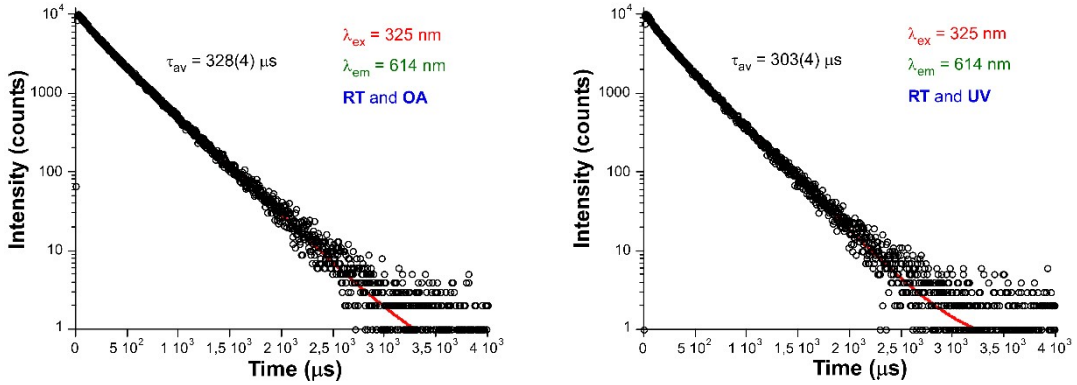

Figure S46. Decay curves of compound $\mathbf{3}_{\mathbf{Eu}}^{\mathbf{D}}$ taken at room temperature.

Compound $\mathbf{5}_{\mathbf{Tb}}^{\mathbf{D}}$ shows the opposite trend to that observed for $\mathbf{3}_{\mathbf{Eu}}^{\mathbf{D}}$, because the emission intensity is slightly increased and the lifetime decreased with the application of vacuum to the sample:

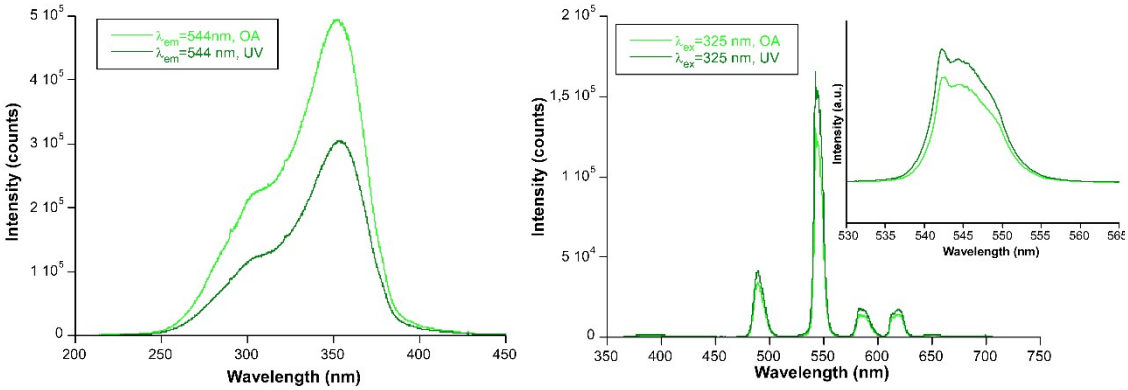

Figure S47. Excitation and emission spectra of compound $\mathbf{5_{Tb}^{D}}$ taken at room temperature under open atmosphere (OA) and under vacuum (UV).

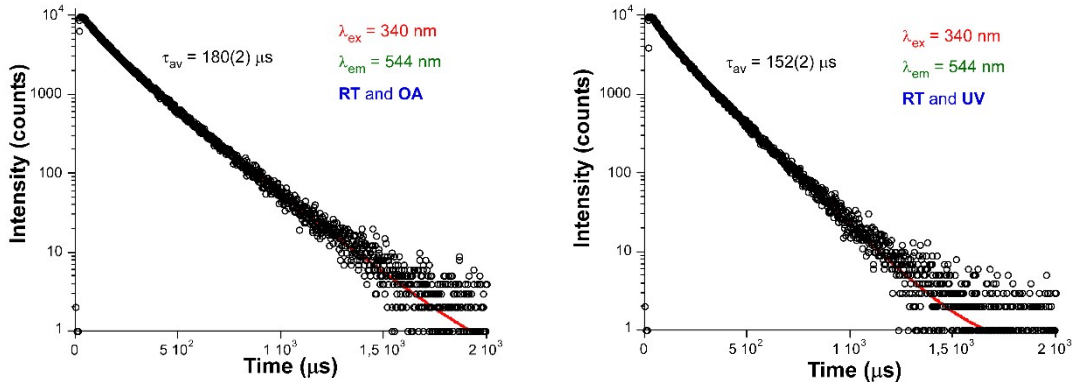

Figure S48. Decay curves of compound $\mathbf{5_{Tb}^{D}}$ taken at room temperature.

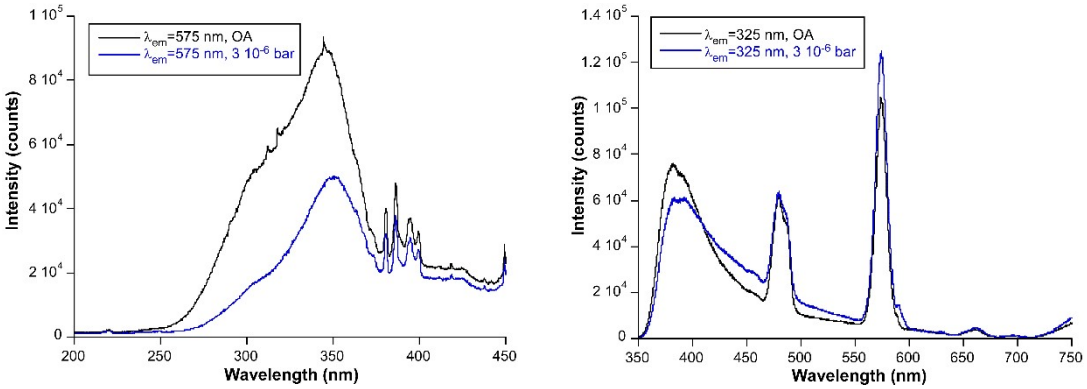

Figure S49. Excitation and emission spectra of compound $\mathbf{6_{Dy}^{D}}$ taken at room temperature under open atmosphere (OA) and under vacuum (UV).

The effect of the dehydration has been also monitored for compound $\mathbf{4_{Gd}}$, by analyzing $\mathbf{4_{Gd}^{D}}$, in order to estimate valuable data about the ligand-centred triplet emission at low temperature.

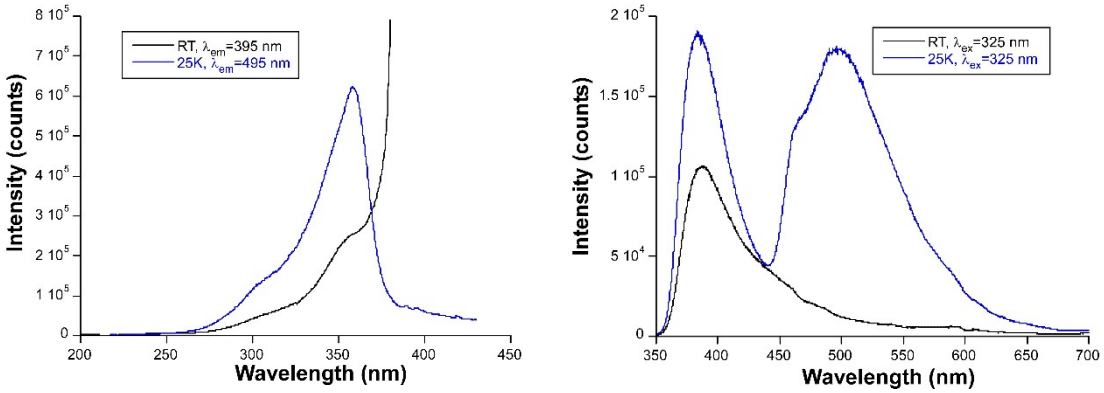

(a) **(b)**

Figure S50. Comparative excitation and emission spectra of compound $\mathbf{4_{Gd}^{D}}$ taken at variable temperature with: **(a)** λ_{em} = 395 nm and **(b)** λ_{ex} = 325 nm.

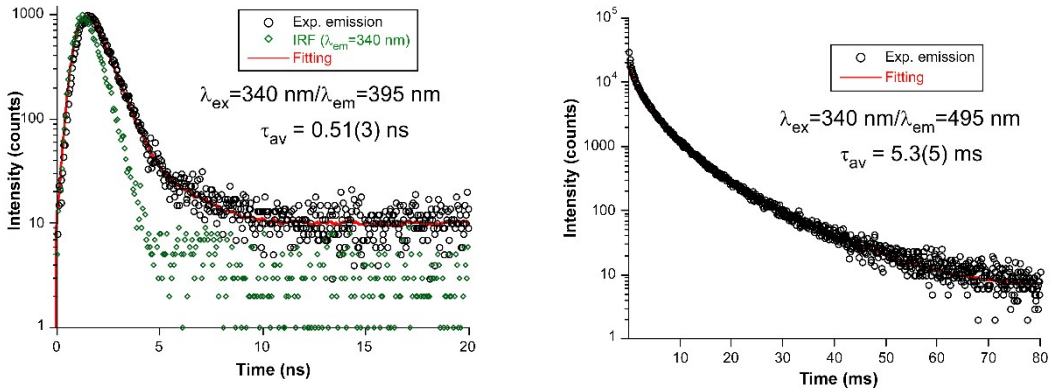

(a) **(b)**

Figure S51. Decay curves of compound $\mathbf{4_{Gd}^{D}}$ recorded under LED pulsed lamp illumination (λ_{ex} = 340 nm) for: **(a)** λ_{em} = 395 nm at room temperature and **(b)** λ_{em} = 495 nm at low temperature.

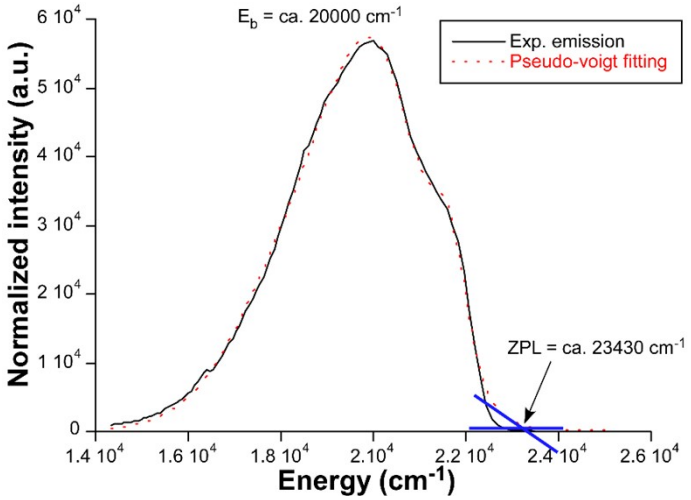

Figure S52. Processed phosphorescence emission spectrum for compound $\mathbf{4_{Gd}^{D}}$ recorded at t = 5 ms (after the lamp pulse) showing the best gaussian fitting to estimate the barycentre and zero-phonon line.

The emission colour of the dehydrated compounds changes remarkably for $\mathbf{5}_{\mathbf{Tb}}^{\mathbf{D}}$ whereas is practically unchanged for $\mathbf{3}_{\mathbf{Eu}}^{\mathbf{D}}$ compared to the neat compounds as corroborated by the micro-PL photographs shown below:

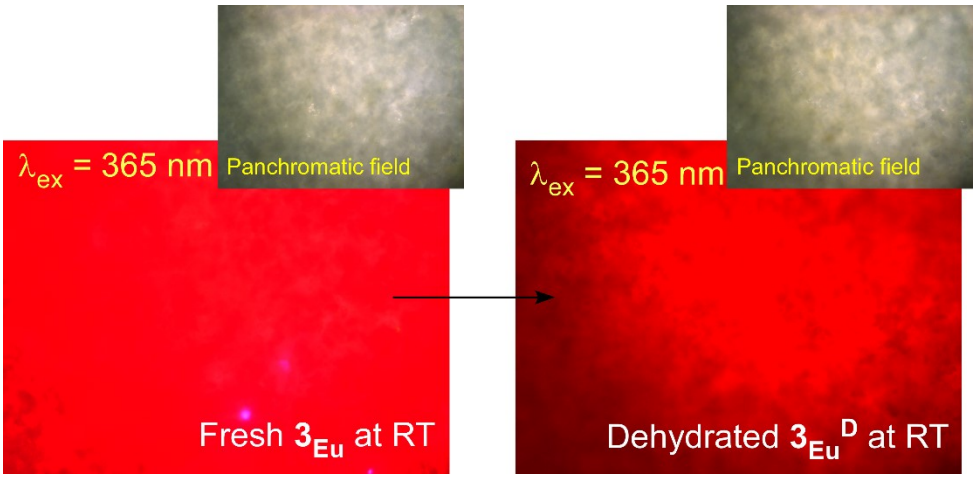

Figure S53. Comparative emission of the micro-PL images of the original ($\mathbf{3}_{\mathbf{Eu}}$) and dehydrated ($\mathbf{3}_{\mathbf{Eu}}^{\mathbf{D}}$) samples taken at room temperature.

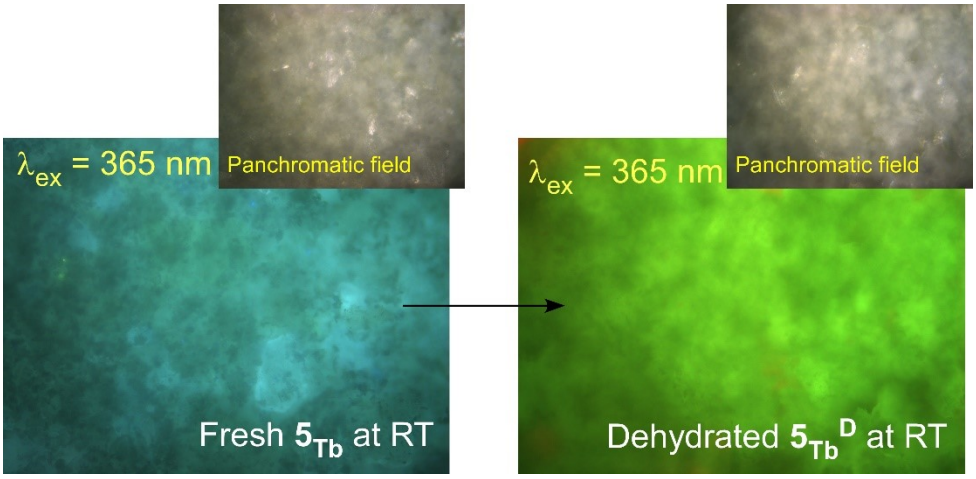

Figure S54. Comparative emission of the micro-PL images of the original ($\mathbf{5}_{\mathbf{Tb}}$) and dehydrated ($\mathbf{5}_{\mathbf{Tb}}^{\mathbf{D}}$) samples taken at room temperature.

S16. Evolution of PL properties of compounds under low temperature.

After this first inspection of the samples under the vacuum at room temperature, the measurements were repeated at low temperatures by the action of a He recovery system that requires previous high vacuum in a cryostat. Therefore, all samples included in this section can be referred to as $\mathbf{3_{Eu}}^{UV}$ and $\mathbf{5_{Tb}}^{UV}$:

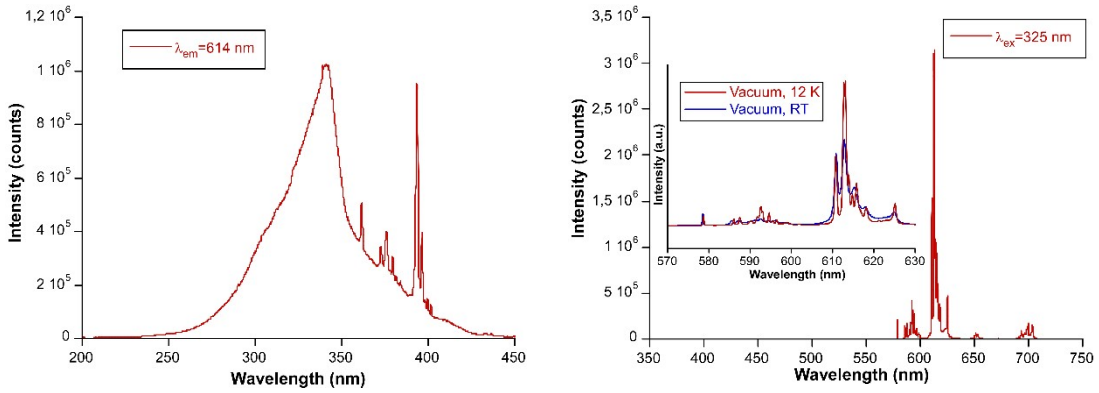

Figure S55. Excitation (λ_{em}=614 nm) and emission (λ_{ex}=325 nm) spectra of compound $\mathbf{3_{Eu}}^{UV}$ taken at low temperature under high vacuum.

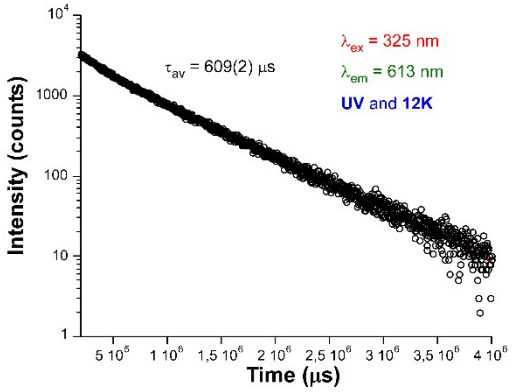

Figure S56. Decay curve of compound $\mathbf{3_{Eu}}^{UV}$ taken at low temperature.

Contrary to what happens for the Eu counterpart, a sample of $\mathbf{5_{Tb}}^{UV}$ shows a decrease of the total intensity of the emission signal when applying the vacuum, as discussed in the manuscript.

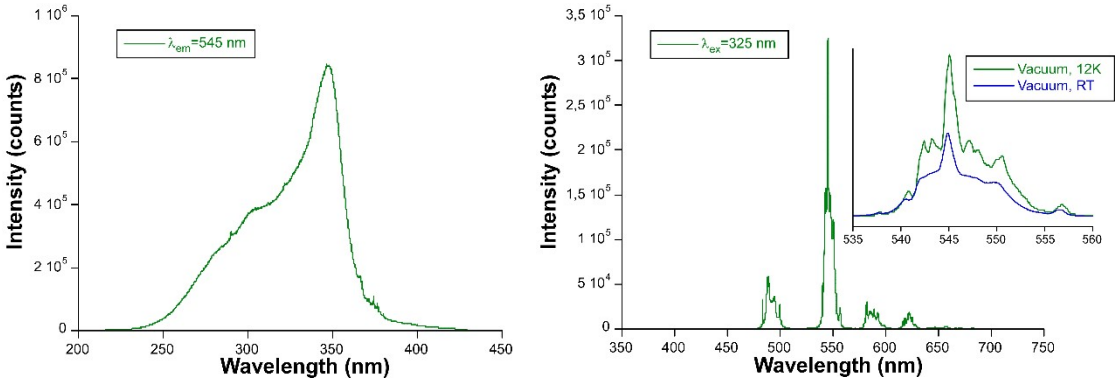

Figure S57. Excitation and emission spectra of compound $\mathbf{5_{Tb}}^{UV}$ taken at low temperature. Inset shows the comparative emission for RT and low temperature under vacuum.

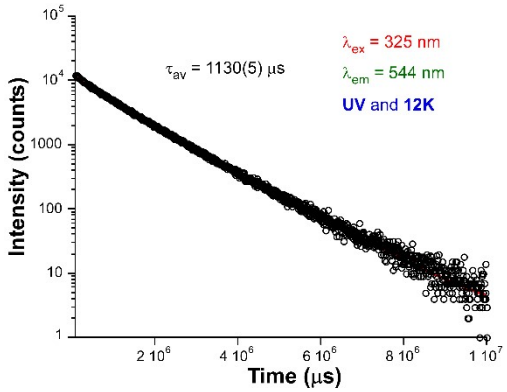

Figure S58. Decay curve of compound $\mathbf{5_{Tb}}^{UV}$ taken at low temperature.

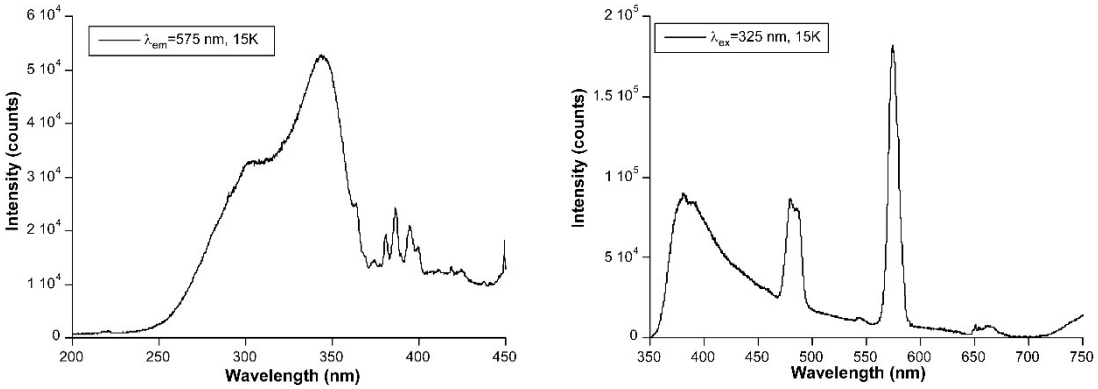

Figure S59. Excitation and emission spectra of compound $\mathbf{6_{Dy}}^{D}$ taken at low temperature.

The emission lifetimes could not be estimated for the dehydrated compound $\mathbf{6_{Dy}}^{D}$ as already happened for the original compound because the lifetimes are shorter than the pulse of the employed nanosecond-based lamp.

Below are shown thermometric evolution of all samples, together with the best fitting results:

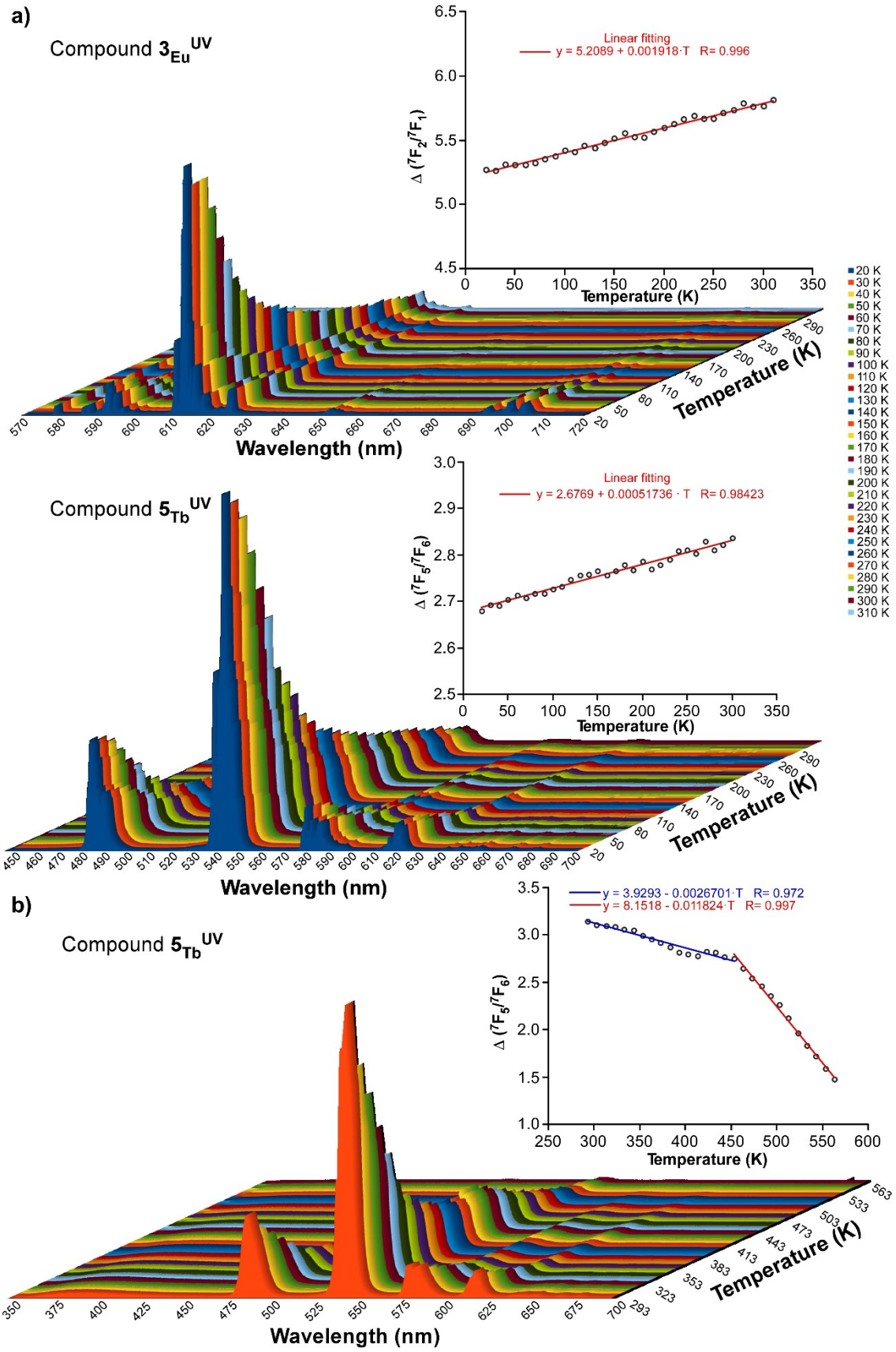

Figure S60. Thermometric evolution of the luminescent emission of compounds $\mathbf{3}_{\mathbf{Eu}}^{\mathbf{UV}}$ and $\mathbf{5}_{\mathbf{Tb}}^{\mathbf{UV}}$. Inset shows the linear fitting for the $\Delta(^7F_2/^7F_1$ for Eu and $^7F_5/^7F_6$ for Tb) parameter in **a)** low and **b)** high temperature.

At last, the PL of these dehydrated compounds $\mathbf{3}_{\mathbf{Eu}}^{\mathbf{D}}$ and $\mathbf{5}_{\mathbf{Tb}}^{\mathbf{D}}$ was measured under variable low temperatures:

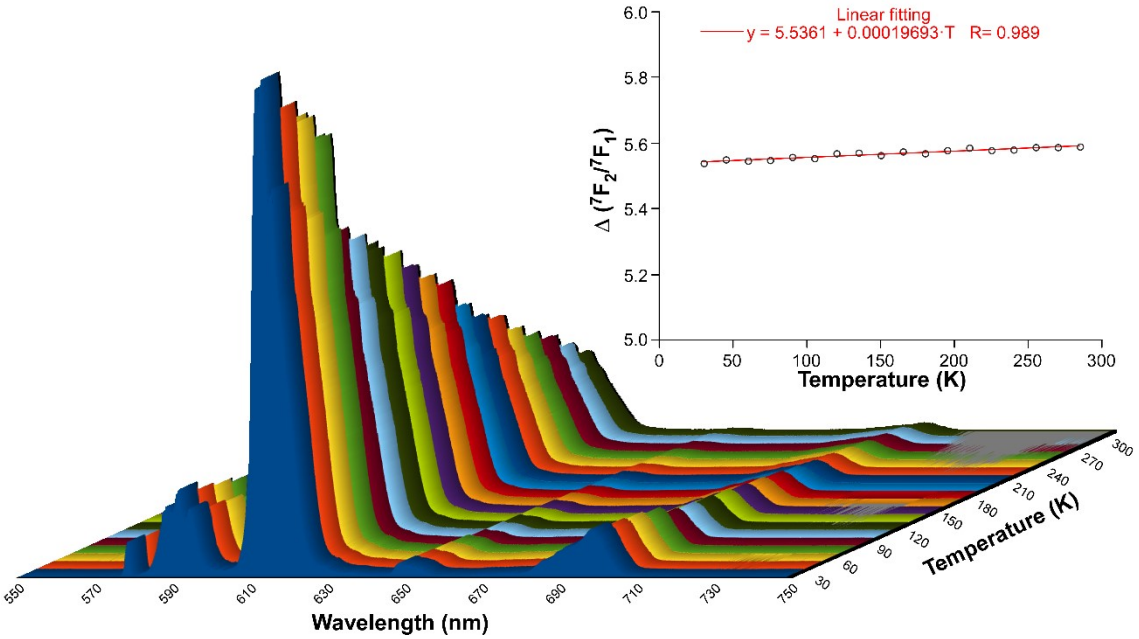

Figure S61. Thermoluminescent emission of compound $\mathbf{3}_{\mathbf{Eu}}^{\mathbf{D\text{-}V}}$ taken in the 30-300 K range at λ_{ex} = 325 nm.

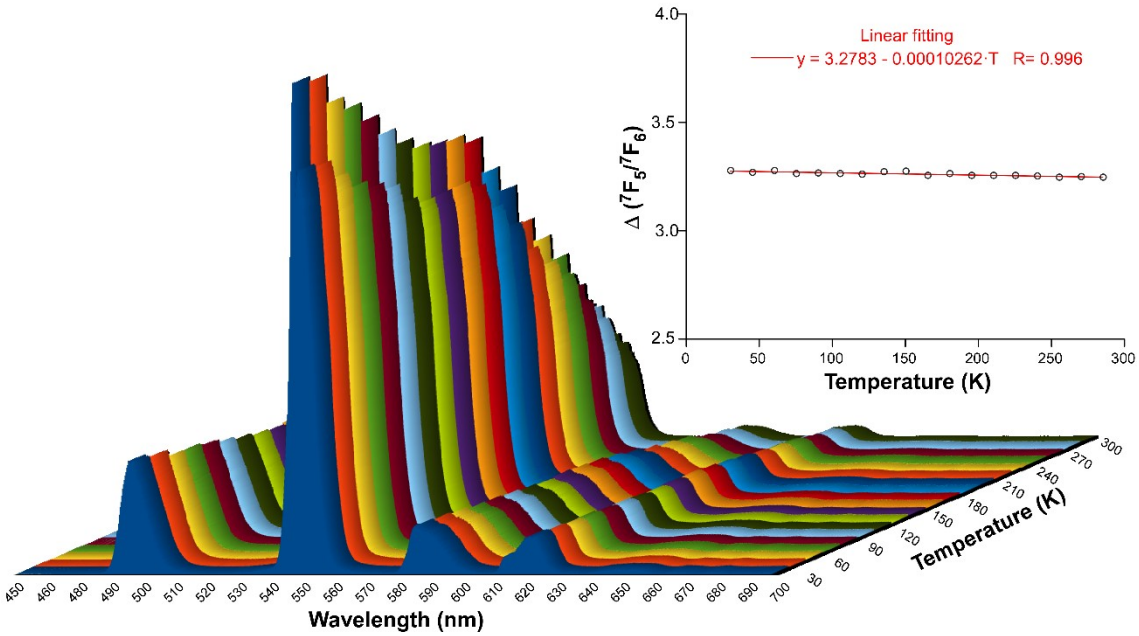

Figure S62. Thermoluminescent emission of compound $\mathbf{5}_{\mathbf{Tb}}^{\mathbf{D\text{-}V}}$ taken in the 30-300 K range at λ_{ex} = 325 nm.

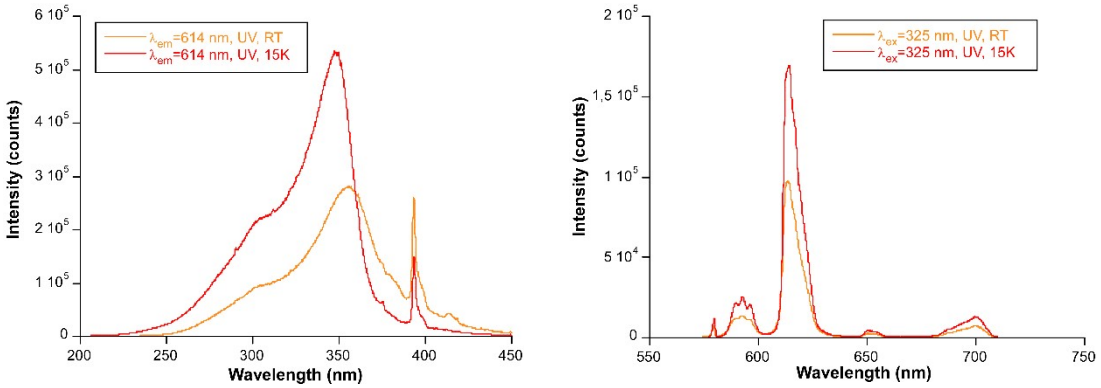

Figure S63. Excitation and emission spectra of compound $\mathbf{3}_{\mathbf{Eu}}^{\mathbf{D\text{-}V}}$ taken at low temperature.

The decay curve of the Eu-centred emission on $\mathbf{3}_{\mathbf{Eu}}^{\mathbf{D\text{-}V}}$ has been acquired under the same experimental setup used for the original $\mathbf{3}_{\mathbf{Eu}}$ compound.

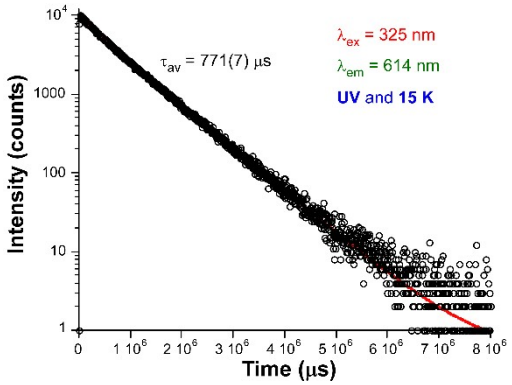

Figure S64. Decay curves of compound $\mathbf{3}_{\mathbf{Eu}}^{\mathbf{D\text{-}V}}$ taken at low temperature.

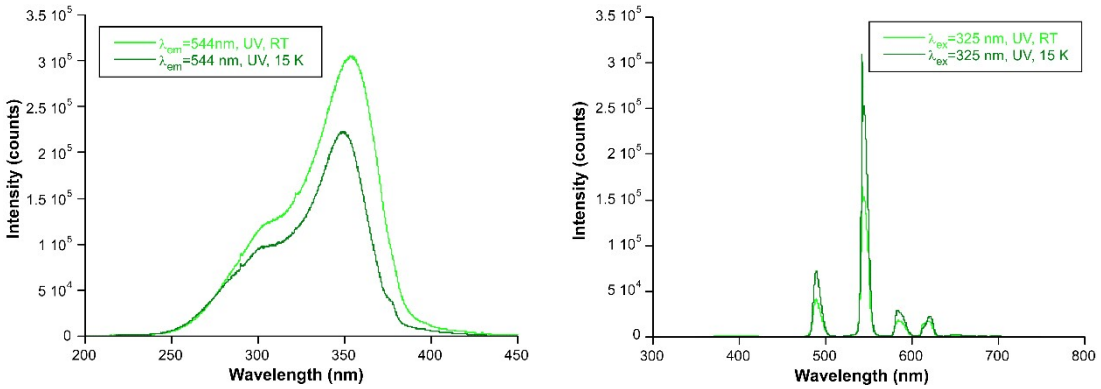

Figure S65. Excitation and emission spectra of compound $\mathbf{5}_{\mathbf{Tb}}^{\mathbf{D\text{-}V}}$ taken at low temperature.

The decay curve of the Tb-centred emission on $\mathbf{5}_{\mathbf{Tb}}^{\mathbf{D\text{-}V}}$ has been acquired under the same experimental setup used for the original $\mathbf{5}_{\mathbf{Tb}}$ compound.

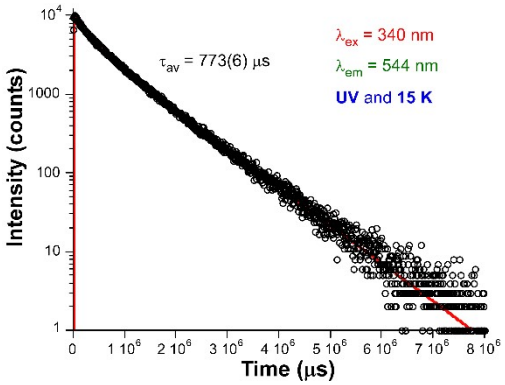

Figure S66. Decay curve of compound $\mathbf{5}_{\mathbf{Tb}}^{\mathbf{D\text{-}V}}$ taken at low temperature.

S17. Evolution of PL properties of compound $\mathbf{5_{Tb}}$ under high temperature.

As mentioned in the manuscript, the thermometric activity of compound $\mathbf{5_{Tb}}$ was evaluated in high temperature range, covering the photoluminescence evolution of the compound (starting from RT) during its thermal dehydration (up to 290 ºC), thus leading to $\mathbf{5_{Tb}^{D}}$. Such a process is irreversible because the thermal treatment promotes the amorphization of the compound. As observed in the next figure, the sample recovers part of the PL emission signal compared to the high temperature data (where the non-vibrational pathways dominate the scenario causing a massive quenching of the PL emission) although the pattern of the PL bands after the thermal treatment has changed compared to the original compound.

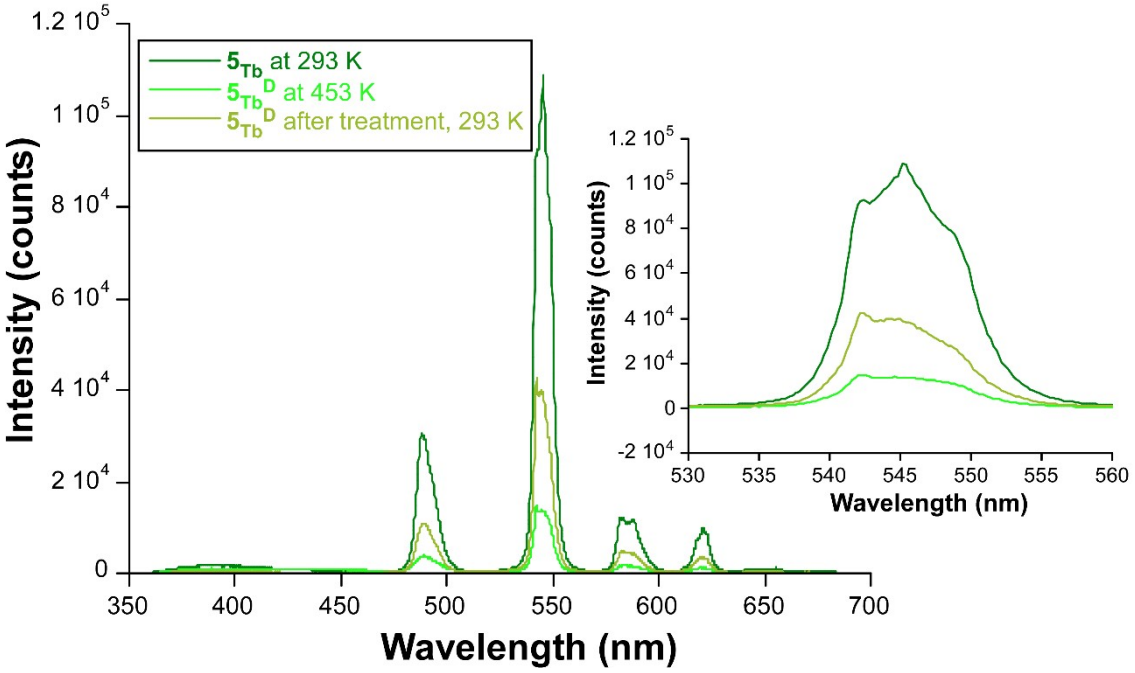

Figure S67. Comparative emission spectra between original compound $\mathbf{5_{Tb}}$ at 293 K, $\mathbf{5_{Tb}^{D}}$ at 563 K and $\mathbf{5_{Tb}^{D}}$ at 293 K (after treatment).

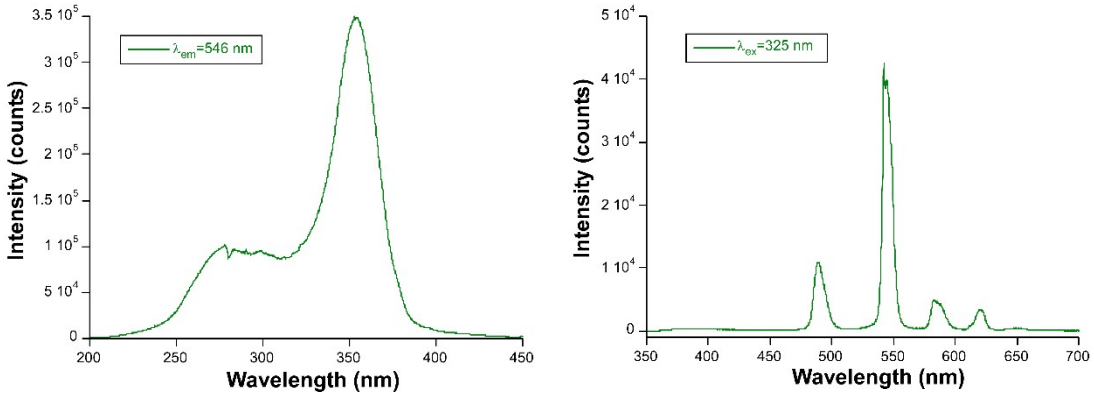

Figure S68. Excitation and emission spectra of compound $\mathbf{5_{Tb}^{D}}$ (after thermometric treatment up to 563 K) taken at room temperature.

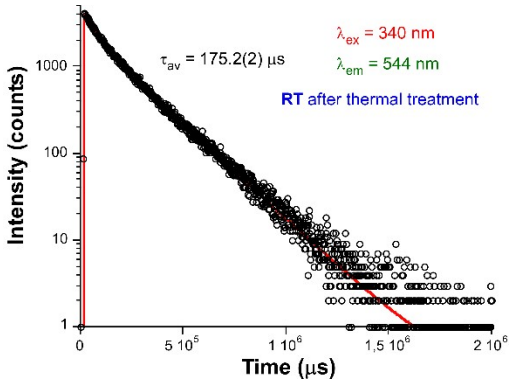

Figure S69. Decay curve of compound $\mathbf{5}_{\mathbf{Tb}}^{\mathbf{D}}$ (after thermometric treatment up to 563 K) taken at room temperature.

S18. ^{1}H NMR and ESI-MS characterization in aqueous solution.

As stated in the manuscript, these compounds present quite high solubility in water. Given that dissolved compounds preserve their good photoluminescence properties once dissolved, we may anticipate that, during dissolution, these compounds could potentially preserve part of their initial structure, particularly the $[M(\mu\text{-}2onic)_4]^-$ anionic complex because it is a priori the most stable entity in the crystal structure being formed by four chelating rings. In this sense, ^{1}H NMR characterization was employed to corroborate the stability of the yttrium-based complex (**1$_Y$**) as a representative sample of the family due to its diamagnetic nature by the comparison of its spectrum with that of the free ligand. The samples were prepared by dissolving 0.5 mg of each compound in 500 µL of deuterated water. A stoichiometric amount of NaOH was added to the sample of the ligand to complete its dissolution, otherwise the protonated form H2onic is not soluble. As observed, the signals corresponding to the aromatic protons are significantly shifted due to the coordination of the ligand to the Y(III) ion in the soluble complex. No trace for the equivalent signals assigned to the free 2onic molecule are observed in the corresponding chemical shift in the spectrum of the dissolved **1$_Y$** compound (**1$_Y$@H$_2$O**), meaning that a speciation of the complex (dissociation of a coordinated ligand) does not happen.

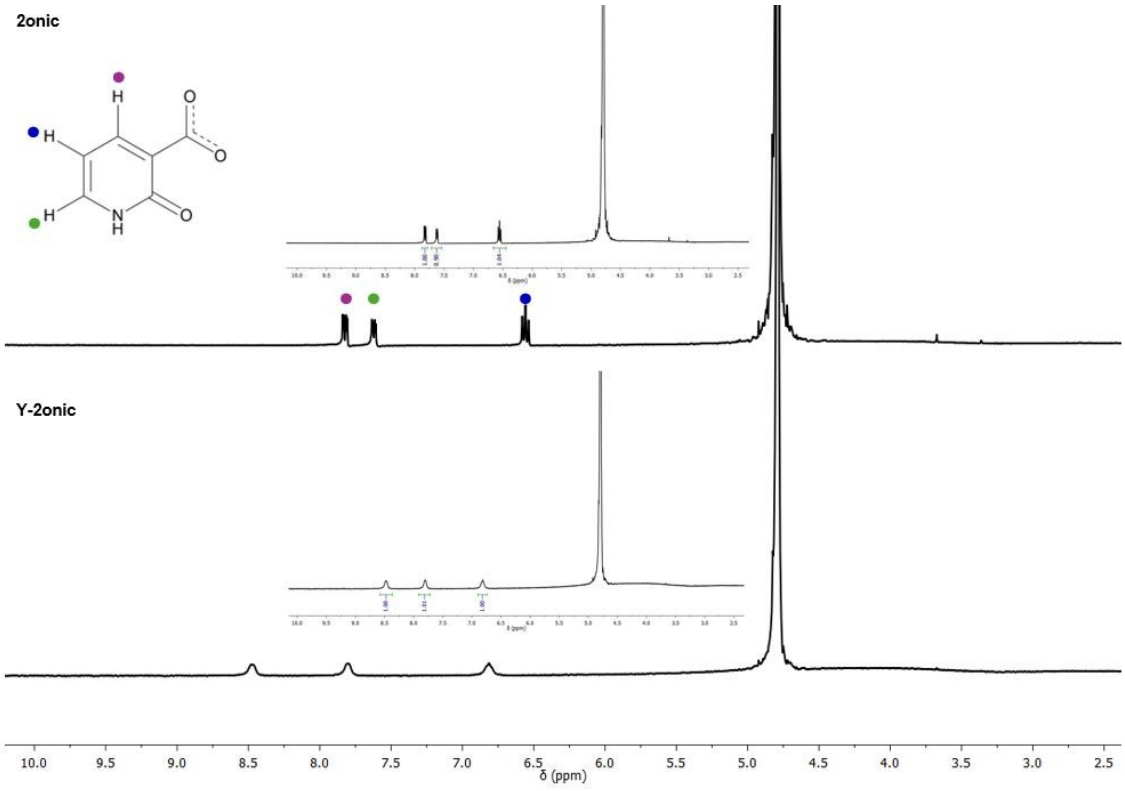

Figure S70. ^{1}H NMR results for the water-dissolved compound **1$_Y$@H$_2$O** (top) and free 2onic ligand (bottom). Signals are assigned by colours (see molecular structure of the ligand). Insets show detailed integration for both samples.

The solution containing the complex (**1$_Y$@H$_2$O**) was subsequently analyzed by this technique periodically during five months, showing no evidence of speciation in the last measurement.

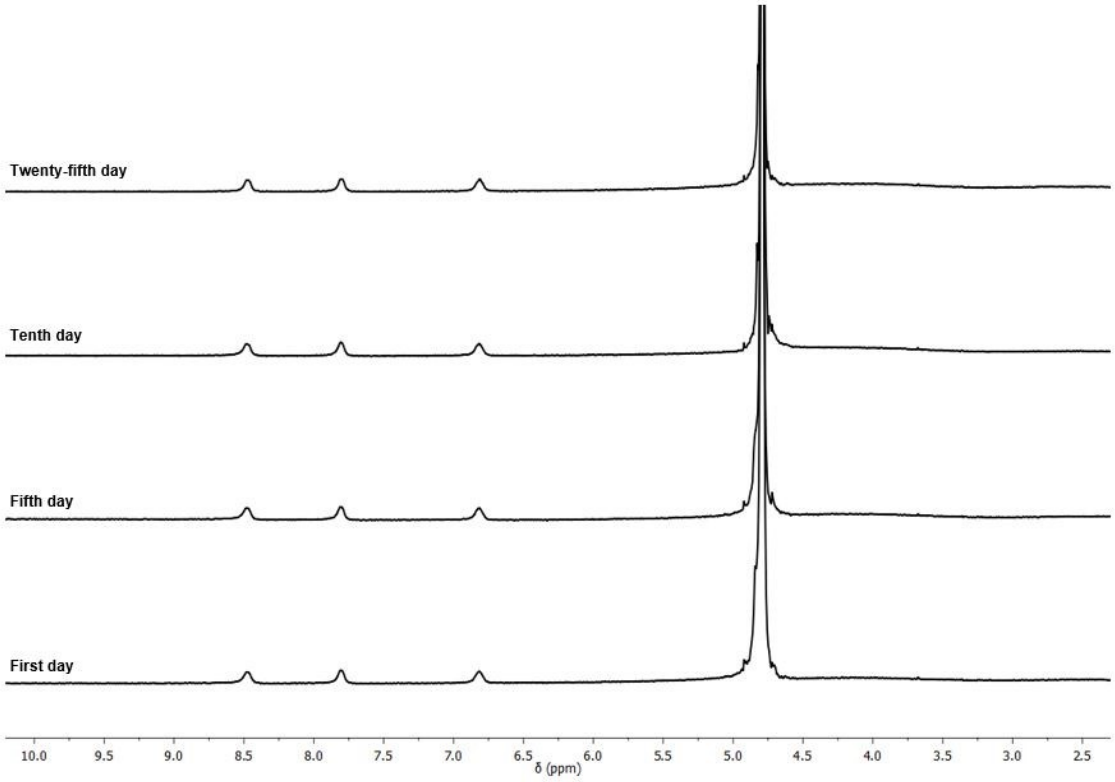

Figure S71. ^{1}H NMR spectra for $\mathbf{1_Y@H_2O}$ acquired along several months after solution preparation to show the stability of the complex.

In addition to the NMR, we also performed an analysis of the water stable complex by ESI MS measurements, recorded at a flow rate of 20 μL/min by an electrospray ionization source in positive and negative modes. High resolution data were acquired in scan mode, using a mass range of 30−1200 u in resolution mode (FWHM ≈ 20,000) and a scan time of 0.1 s. The source temperature was set to 120 °C and the desolvation temperature to 350 °C. The capillary voltage was 2.5 kV (negative) and the cone voltage was 15 V. Nitrogen was used as the desolvation and cone gas at flow rates of 600 and 10 L/h, respectively. Before analysis, the mass spectrometer was calibrated with a sodium formate solution and a leucine enkephalin solution was used for the lock mass correction, monitoring the ions at a mass-to-charge ratio (m/z) of 556.2771. All of the acquired spectra were automatically corrected during acquisition based on the lock mass. Note that the rest of the spectrum contains only some residual signals lacking periodicity that could not be properly assigned. As observed in the figure below, a very intense signal centred at an *m*/*z* of 641 and with a periodicity of one unit (indicative of a -1 charge) was found in the ESI$^-$ MS spectrum, which fits well with the $[Y(2onic)_4]^-$ complex.

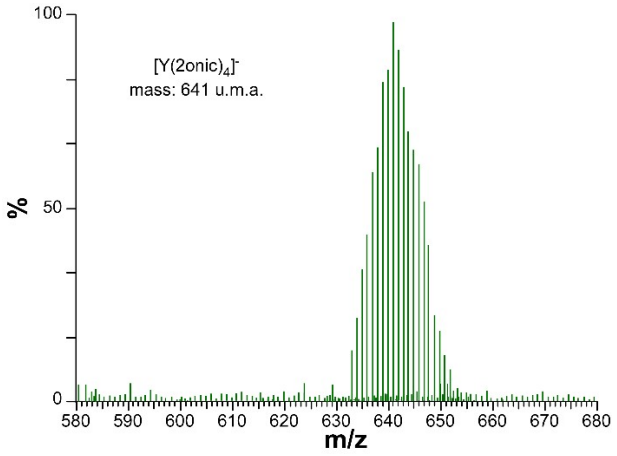

Figure S72. Magnified ESI$^-$ MS spectrum of $\mathbf{1_Y@H_2O}$ focusing the region of interest containing the dissolved complex.

S19. Photophysical characterization of compounds dissolved in aqueous solution.

Figure S73. Photographs of the aqueous $\mathbf{3_{Eu}@H_2O}$ (left) and $\mathbf{5_{Tb}@H_2O}$ (right) solutions (at 1.25 mg mL^{-1} concentration) under UV excitation (λex = 365 nm).

After this confirmation, the PL measurements were performed for the aqueous samples of the free ligand and best-emitting compounds ($\mathbf{3_{Eu}}$, $\mathbf{5_{Tb}}$ and $\mathbf{6_{Dy}}$) at room temperature.

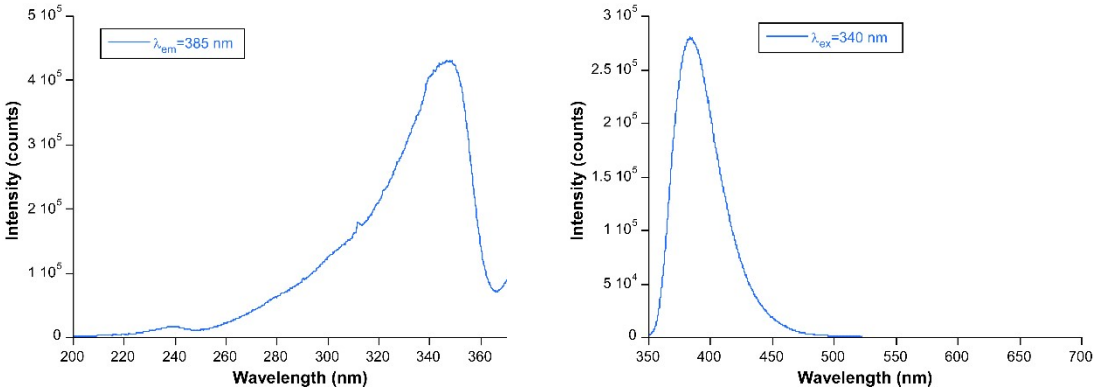

Figure S74. Excitation and emission spectra of the aqueous solution of free H2onic ligand sample taken at room temperature.

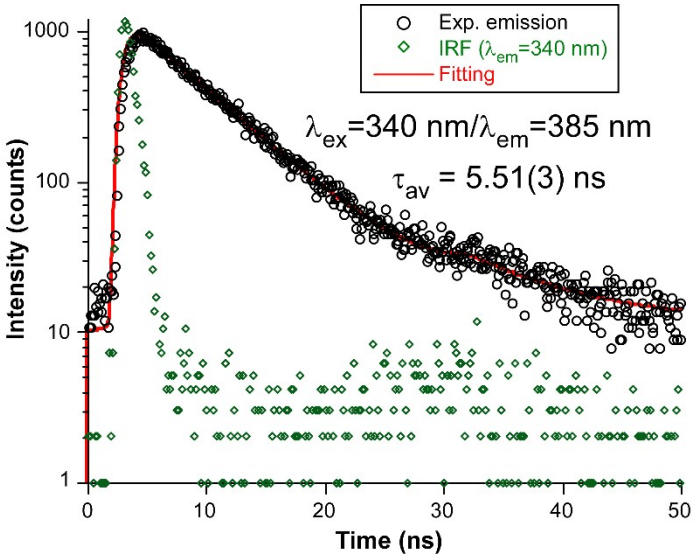

Figure S75. Decay curve of the emission maxima of the aqueous solution of free H2onic ligand sample taken at room temperature.

Further evidence for the stability of the $[M(\mu\text{-}2onic)_4]^-$ anionic fragments after the dissolving of compounds in water is shown by the comparison of the UV-Vis absorbance spectra of the aqueous solutions with the absorption spectra acquired in solid state. The aqueous solutions of these compounds were prepared by dissolving 5 mg of the corresponding compound into 4 mL of distilled water (1.25 mg mL^{-1}). As observed in the figure below, the spectra show the occurrence of three bands resembling those found in the solid (see Figure S13), finding a hypsochromic shift of about 30 nm for the aqueous spectra with respect to the solid.

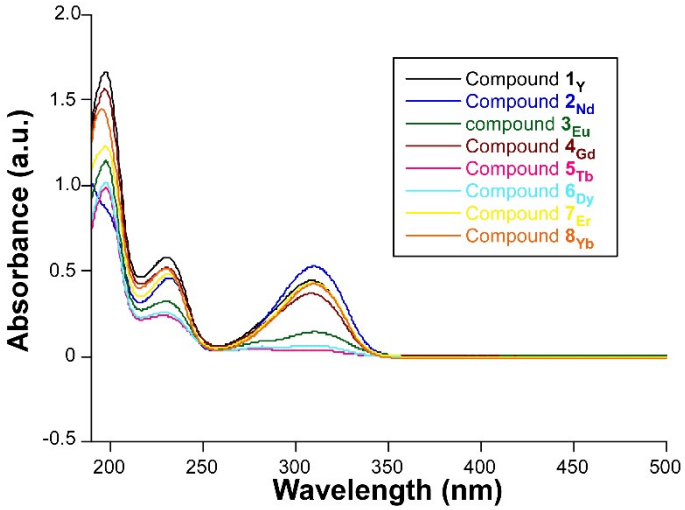

Figure S76. UV-Vis measurement of the aqueous solutions of all compounds.

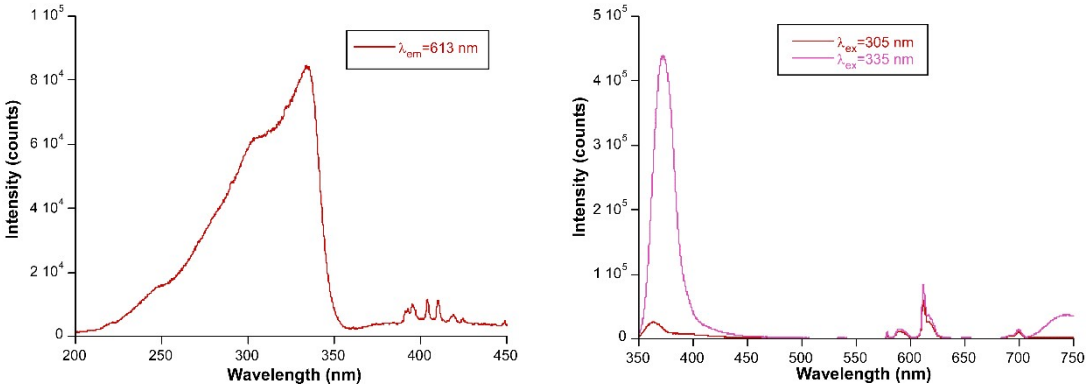

Figure S77. Excitation and emission spectra of compound $\mathbf{3_{Eu}@H_2O}$ taken at ambient conditions.

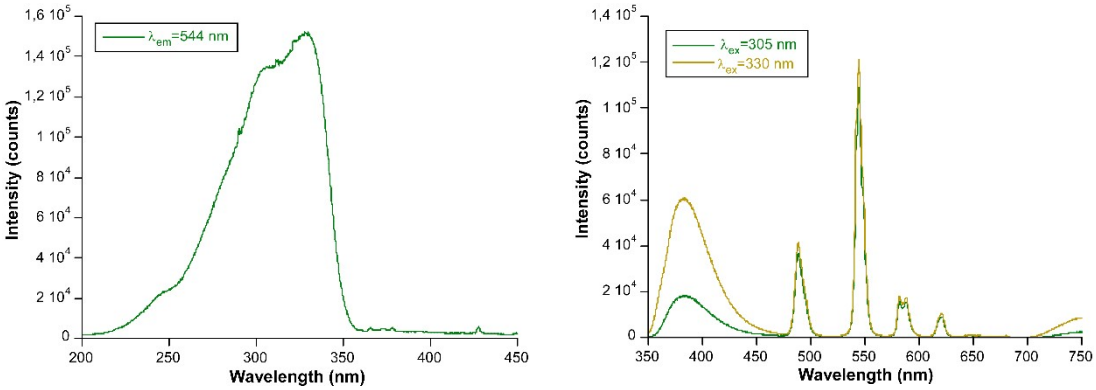

Figure S78. Excitation and emission spectra of compound $\mathbf{5_{Tb}@H_2O}$ taken at ambient conditions.

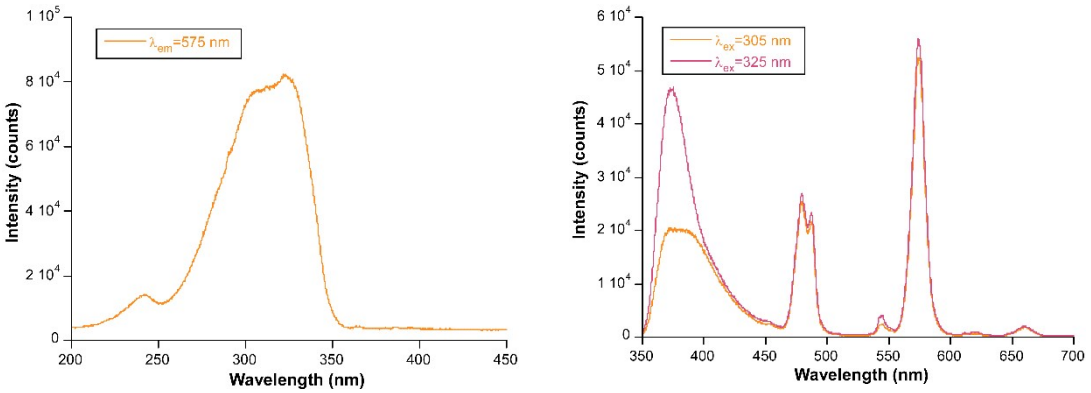

Figure S79. Excitation and emission spectra of compound $\mathbf{6_{Dy}@H_2O}$ taken at ambient conditions.

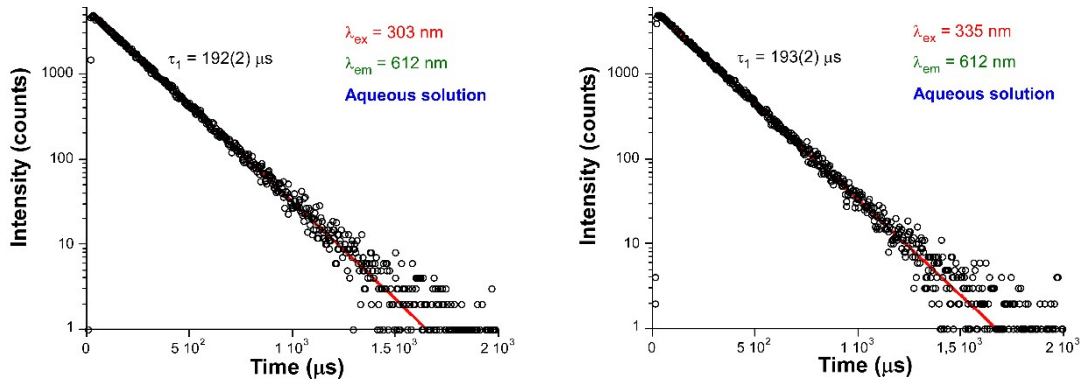

Figure S80. Decay curves with the best fitting results for the aqueous compound $\mathbf{3_{Eu}@H_2O}$ solution.

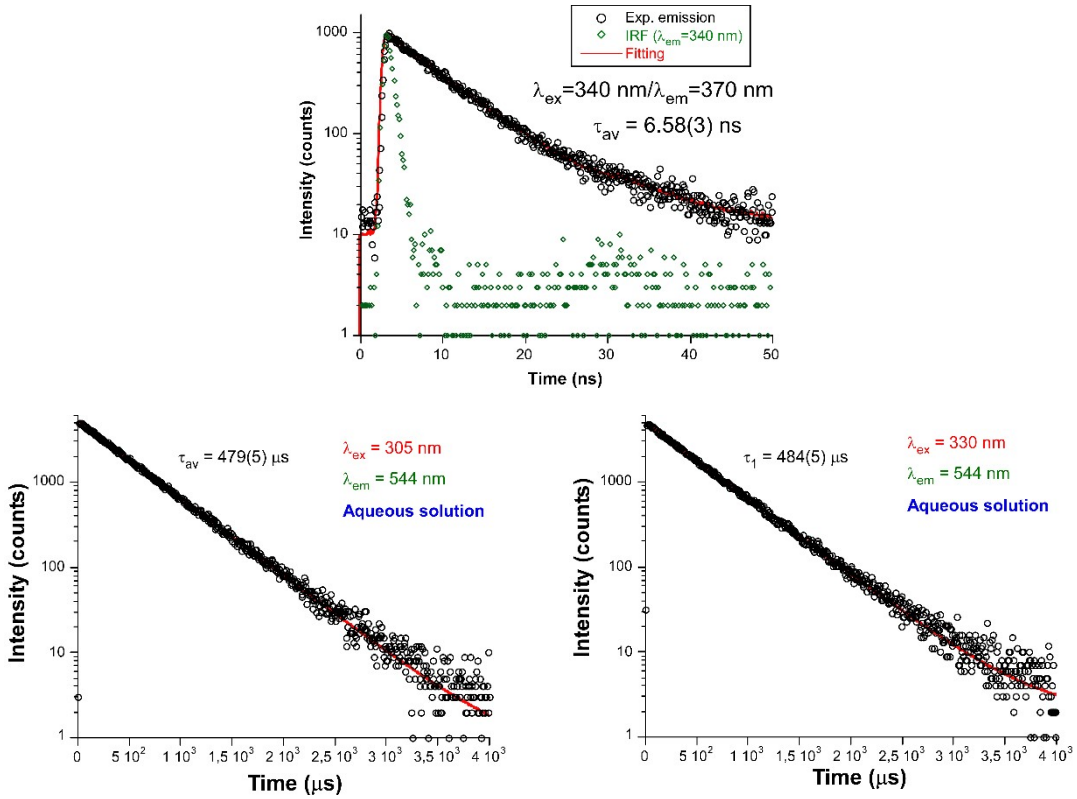

Figure S81. Decay curves with the best fitting results for the aqueous compound $\mathbf{5_{Tb}@H_2O}$ solution.

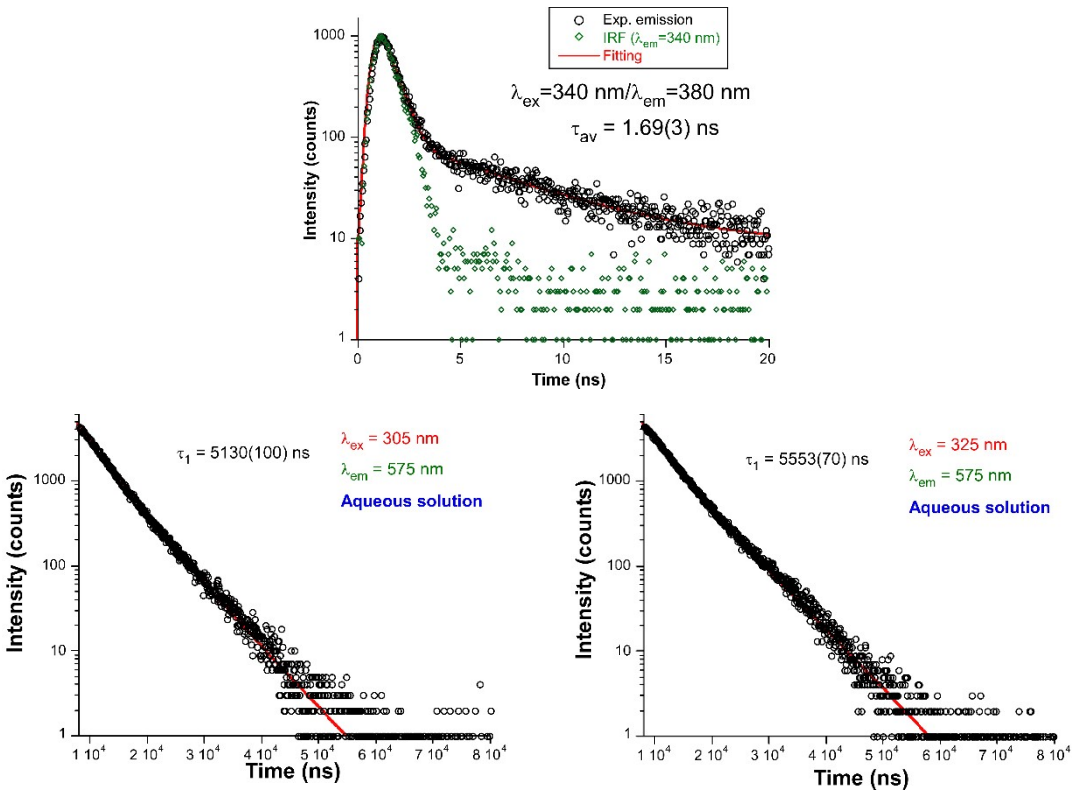

Figure S82. Decay curves with the best fitting results for the aqueous compound $\mathbf{6_{Dy}@H_2O}$ solution.

Number of coordinated water molecules in ***3_{Eu}@H_2O***:

The excitation and emission spectra of dissolved compound $\mathbf{3_{Eu}}$ were also measured in deuterated water in order to estimate the number of coordinated water molecules in the dissolved complex by means of the conventional procedure that makes use of equation 2, in which $A = 1.05$.

$q = A(\tau_{H2O}^{-1} - \tau_{D2O}^{-1})$ (eq. 2)

As stated in the manuscript, $q = 0.0049$, thus a value close to zero, meaning that no water molecule replaces the ligand or incorporates into the complex increasing the coordination number of Eu(III) and therefore, concluding that $[Ln(2onic)_4]^-$ entity is stable in solution in agreement with the NMR and ESI-MS results (see section S11).

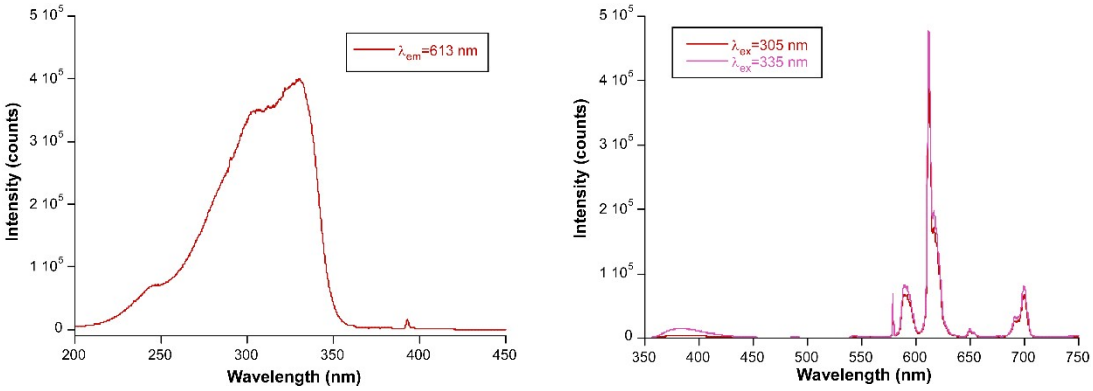

Figure S83. Excitation and emission spectra of $\mathbf{3_{Eu}@D_2O}$ sample taken at room temperature at λ_{em} = 613 nm and λ_{ex} = 304/330 nm.

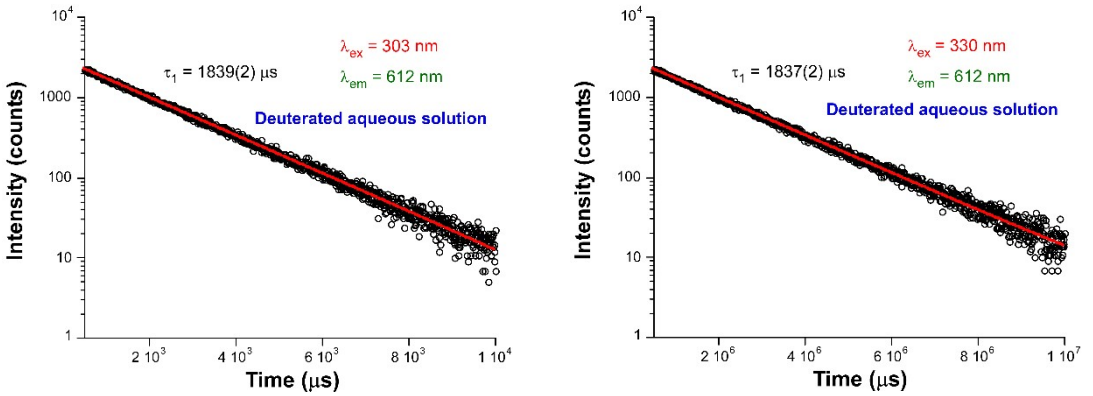

Figure S84. Decay curve of compound $\mathbf{3_{Eu}@D_2O}$ taken at room temperature under the main emission line (λ_{em} = 613 nm).

In addition to the solutions composed of the as-synthesized compounds, we also measured steady-state spectra and decay curves for the solutions containing the dehydrated compounds (thus named as $\mathbf{3_{Eu}^{D}@H_2O}$, $\mathbf{5_{Tb}^{D}@H_2O}$ and $\mathbf{6_{Dy}^{D}@H_2O}$) using the same setup.

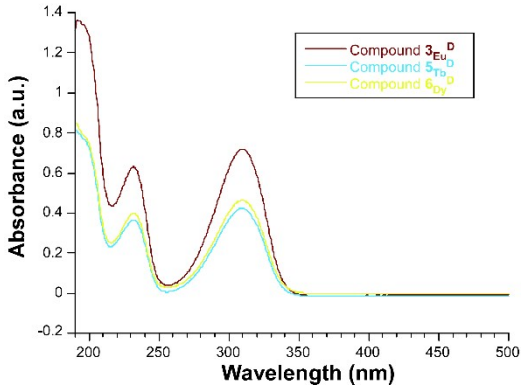

Figure S85. UV-Vis measurement of the aqueous solutions of the dehydrated compounds $\mathbf{3_{Eu}{}^{D}@H_2O}$, $\mathbf{5_{Tb}{}^{D}@H_2O}$ and $\mathbf{6_{Dy}{}^{D}@H_2O}$.

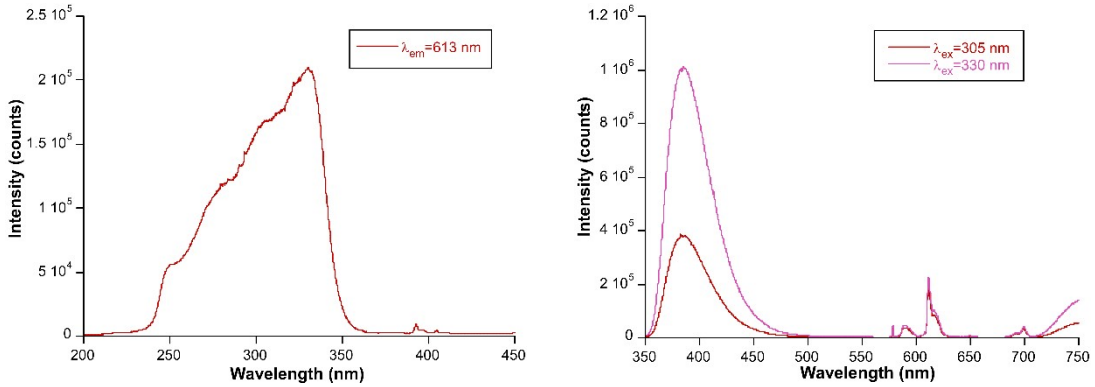

Figure S86. Excitation and emission spectra of compound $\mathbf{3_{Eu}{}^{D}@H_2O}$ taken at ambient conditions.

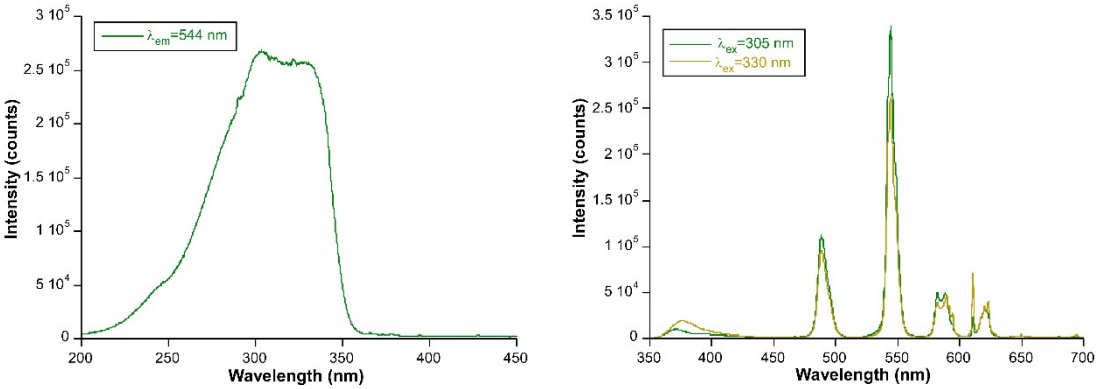

Figure S87. Excitation and emission spectra of compound $\mathbf{5_{Tb}{}^{D}@H_2O}$ taken at ambient conditions.

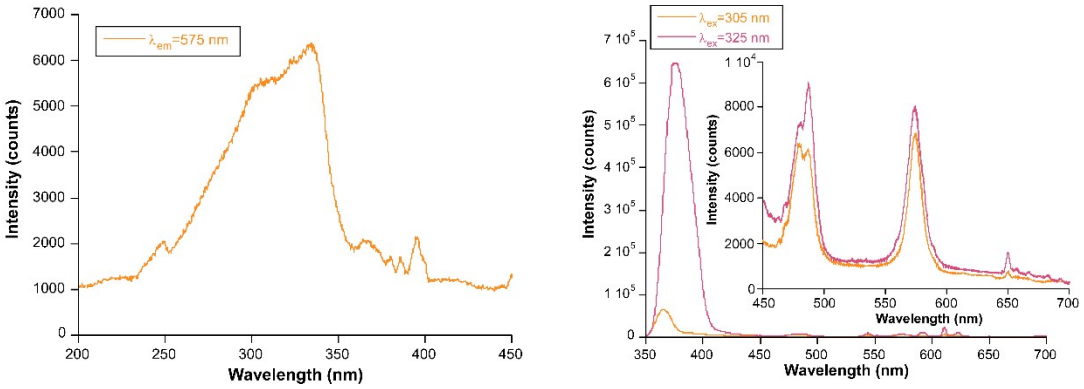

Figure S88. Excitation and emission spectra of compound $\mathbf{6_{Dy}^{D}@H_2O}$ taken at ambient conditions.

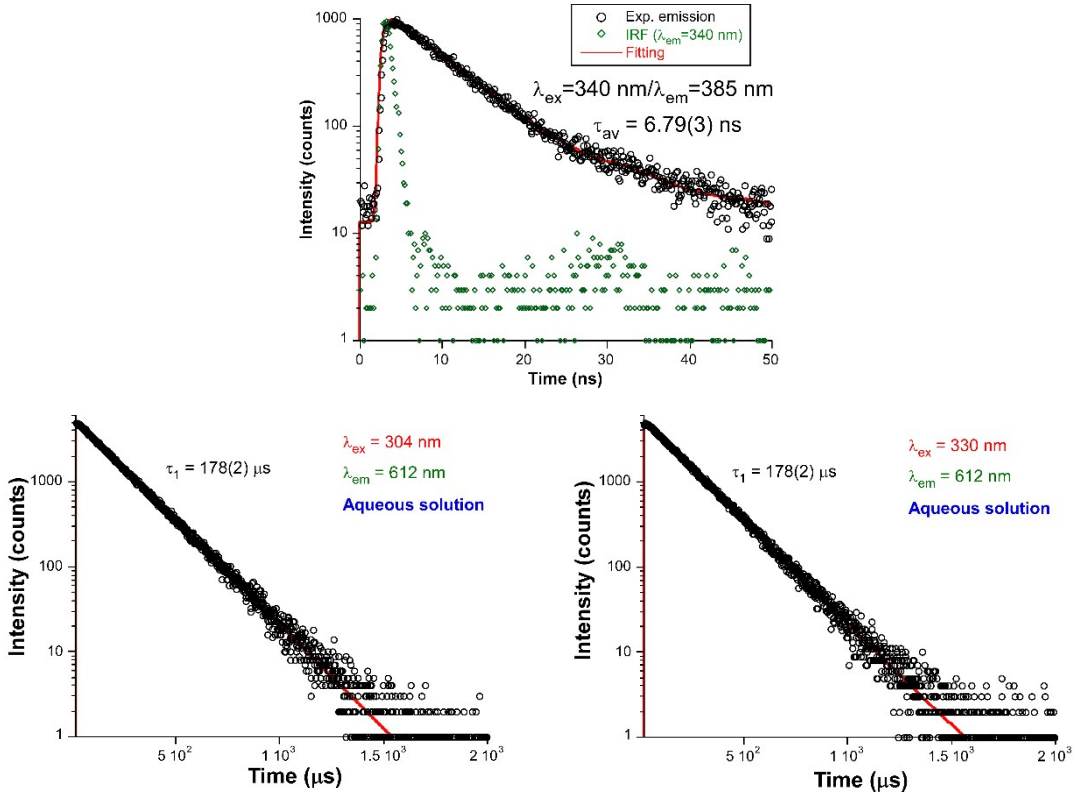

Figure S89. Decay curves with the best fitting results for the aqueous compound $\mathbf{3_{Eu}^{D}@H_2O}$ solution.

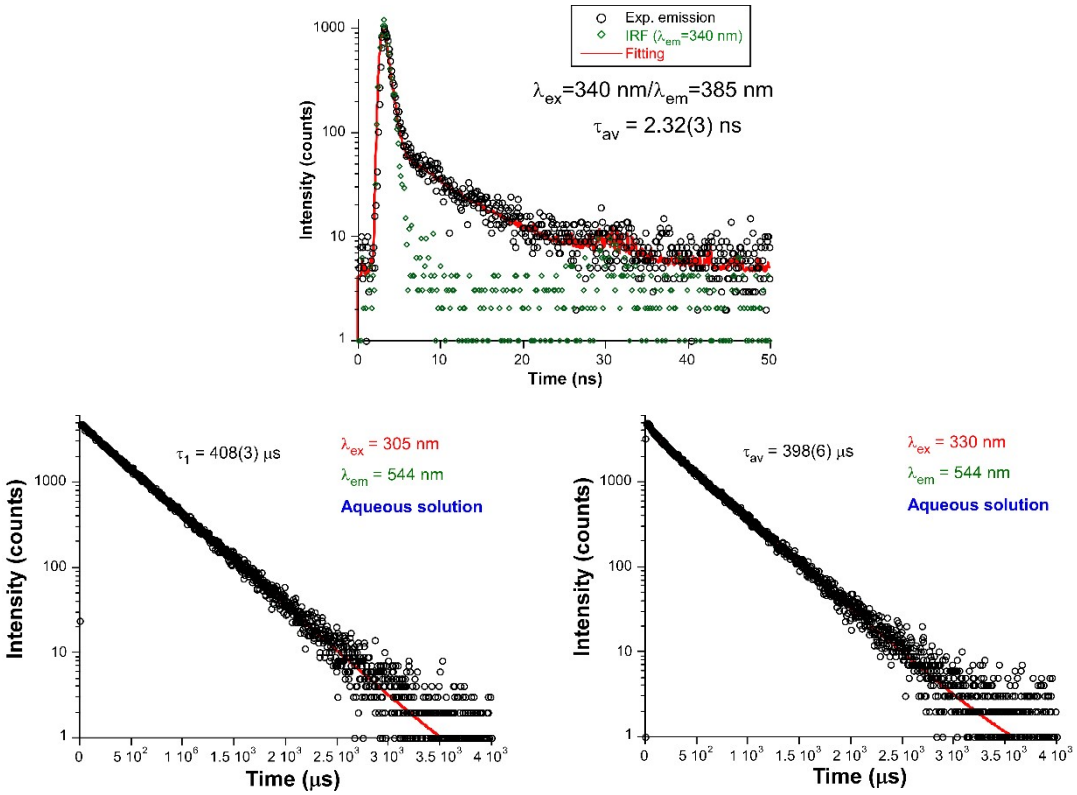

Figure S90. Decay curves with the best fitting results for the aqueous compound $\mathbf{5_{Tb}^{D}@H_2O}$ solution.

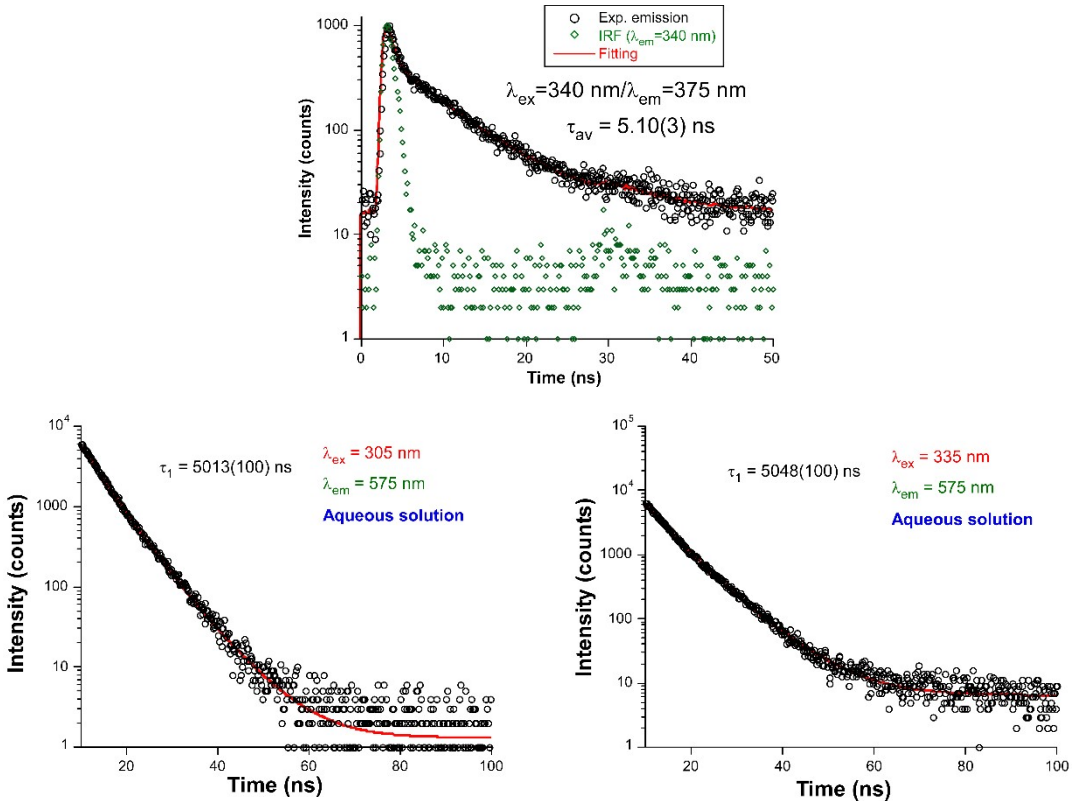

Figure S91. Decay curves with the best fitting results for the aqueous compound $\mathbf{6_{Dy}^{D}@H_2O}$ solution.

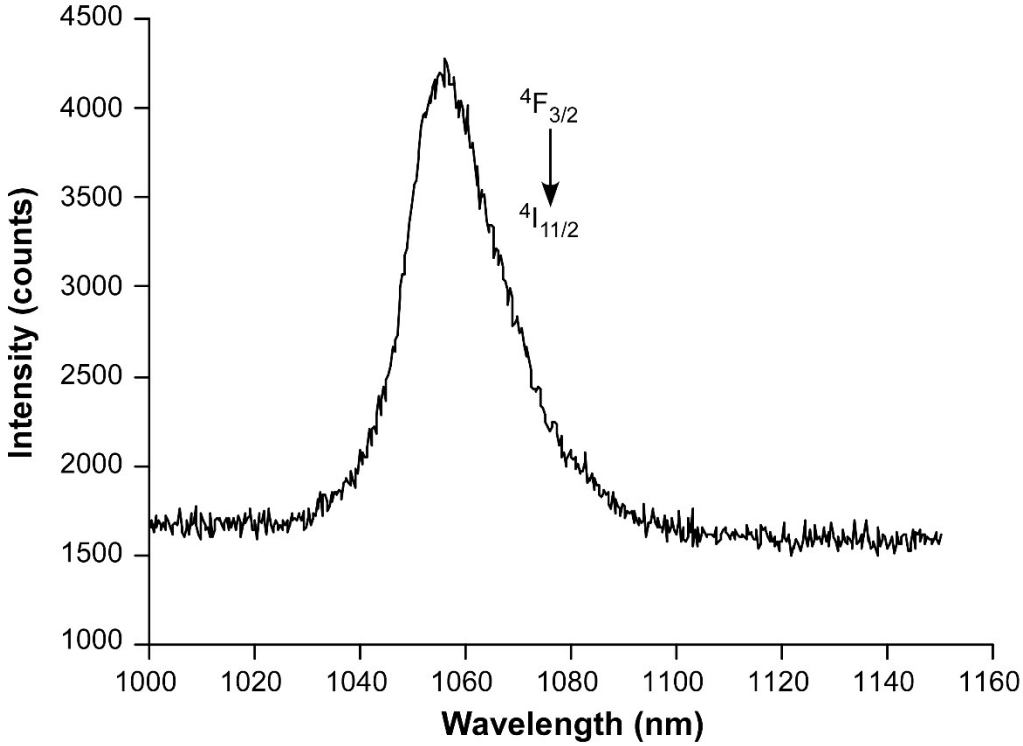

Figure S92. Emission spectrum of compound $\mathbf{2_{Nd}@H_2O}$ taken at ambient conditions.

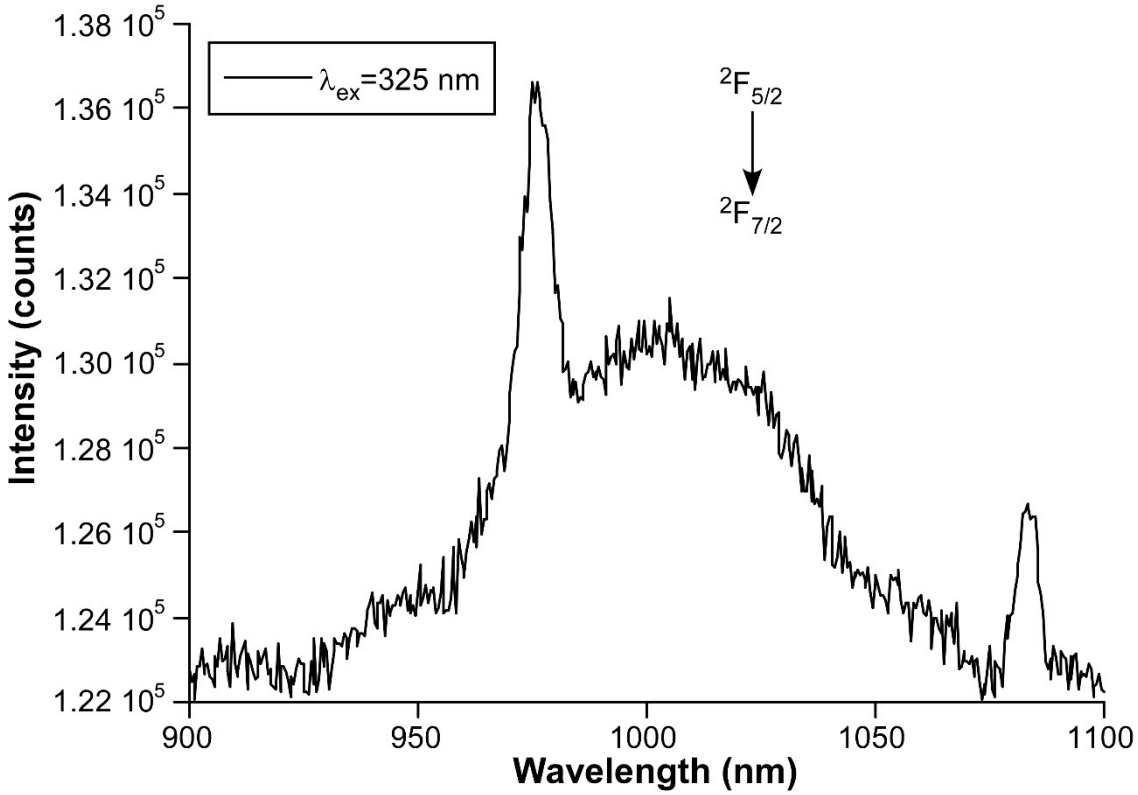

Figure S93. Emission spectrum of compound $\mathbf{8_{Yb}@H_2O}$ taken at ambient conditions.

S20. Computational calculations.

Gaussian 16 package[4] was employed for the geometry optimizations on the suitable models of both H2onic ligand molecule and compound $\mathbf{4}_{\mathbf{Gd}}$. These calculations were performed at B3LYP level of theory with the def2-TZVP basis set the corresponding relativistic pseudo-potential for Gd(III). For the calculations of the UV/Vis absorption spectra, the first 40 excitations were calculated on previous models using MC-RPA methodology run on top of a CASSCF calculation as implemented in ORCA, using the same previously mentioned basis set. The most representative excitations (those with highest oscillator strengths) related to the two main experimental bands have been analyzed and plotted.

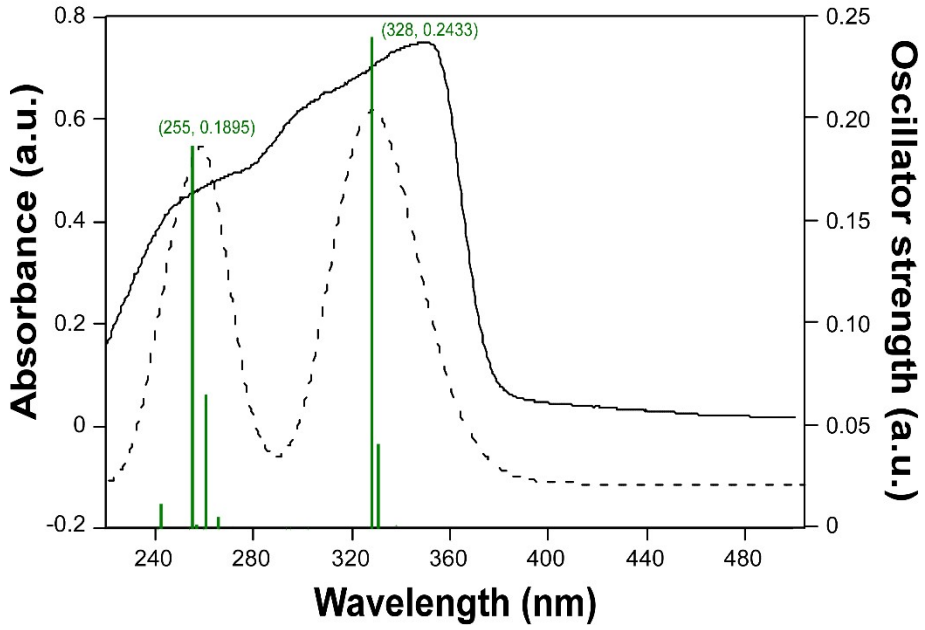

Figure S94. Comparison of UV/Vis absorption and computed spectra with MC-RPA methodology for the suitable model of H2onic ligand.

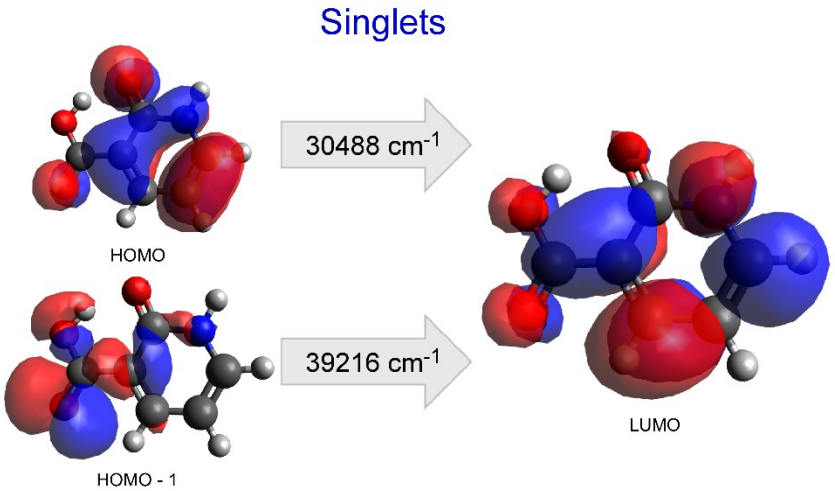

Figure S95. Composition of calculated selected excitations for the optimized model of H2onic ligand molecule.

Table S7. Experimental and calculated main excitation wavelengths (nm) measured at room temperature. Singlet electronic transitions and associated oscillator strengths were calculated using a model of compound $\mathbf{4}_{\mathbf{Gd}}$ in gas phase.

Exp. λ	Calc λ	Significant contributions	State (S_n)	Osc. st. (a.u.)
335	331	HOMO → LUMO (8%) HOMO – 1→ LUMO +1 (7%)	1	0.0583
305	306	HOMO → LUMO + 2 (11%) HOMO – 1→ LUMO +1 (6%)	3	0.2397
235	246	HOMO – 4 → LUMO (6%) HOMO – 2 → LUMO + 2 (5%)	14	0.1610

The possible existence of ligand-to-metal charge transfer (LMCT) states close to the donor levels in the compounds has been explored based on the results of the CASSCF(3,3) calculation performed on the model of compound $\mathbf{4}_{\mathbf{Gd}}$ (see further details in *Computational calculations section in the manuscript*). A rough estimate of LMCT energies can be obtained from the calculated MOs (see Figure, which show that the energy difference between the first unoccupied MO showing substantial contribution at the Gd^{3+} atom and the HOMO is, as shown below, of ca. 53500 cm^{-1}, meaning that the energy for the LMCT band could be located at about 187 nm, therefore, outside the relevant excitation window of the compound.

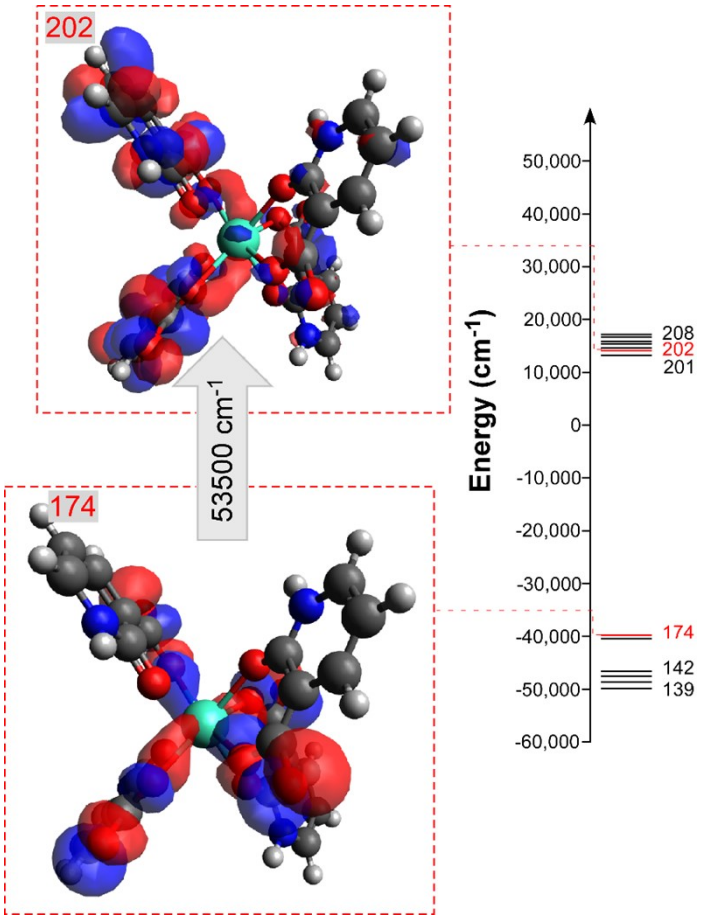

Figure S96. Energy diagram of the MOs of compound $\mathbf{4_{Gd}}$ showing selected HOMO and LUMO to represent an estimation of LMCT energy. Isosurfaces of 0.05 *e*/*a*03.

In the following figure, a representation of the molecular orbitals involved in the abovementioned excited states is shown.

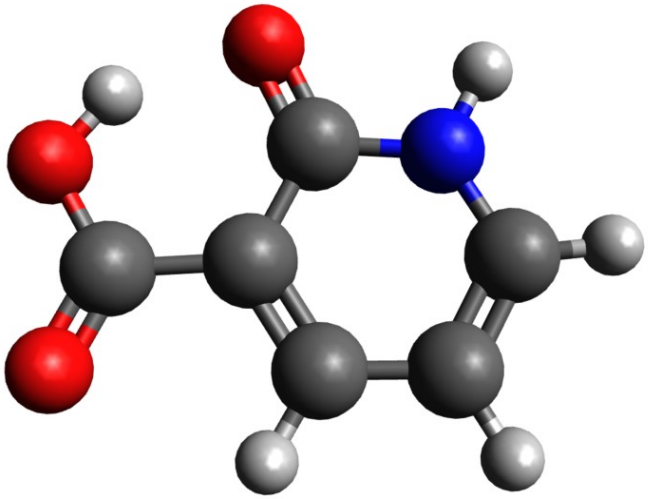

Figure S97. Model of the optimized molecule of the H2onic ligand used for the calculations.

Table S6. Spherical atomic coordinates, charge factors (*g*) and polarizabilities (α) for compound $\mathbf{3_{Eu}}$.

Atoms	Spherical coordinates			g	α (Å^3)
	R (Å)	Θ (°)	Φ (°)		
		Eu1			
O32A	2.5136	63.65	114.16	1.0837	1.0118
O32A(i)	2.5136	116.35	65.84	1.0837	4.7438
O32B	2.3385	132.55	156.04	1.1148	0.0051
O32B(i)	2.3385	47.45	23.96	1.1149	3.9130
O1w	2.4992	62.88	294.98	1.0828	2.0578
O1w(i)	2.4992	117.12	245.02	1.0828	1.3037
O2w	2.3419	46.12	203.31	1.1207	0.6743
O2w(i)	2.3420	133.88	336.69	1.1207	0.8219
		Eu2			
O21A	2.3874	141.43	67.43	1.1321	1.6709
O31A	2.3873	38.57	112.57	1.1321	4.3355
O21A(iv)	2.3596	74.46	32.53	1.1419	3.9102
O31A(iv)	2.3595	105.54	147.47	1.1418	0.5171
O21B(ii)	2.3685	104.62	326.55	1.0119	0.0058
O31B(ii)	2.3684	75.38	213.45	1.1419	0.33874
O21B(iii)	2.3895	37.56	292.26	1.1309	0.6463
O31B(iii)	2.3895	142.44	247.75	1.1309	1.5056

[a] Symmetries: (i) 1/2-x, y, 1/2-z; (ii) 3/2-x, -1+y, 1/2-z; (iii) x, -1+y, z; (iv) 3/2-x, y, 1/2-z.

The energy transfer efficiency (η_{sens}) and the rest of sensitization parameters for the Eu-based compounds was calculated from the experimental values of the observed lifetime (τ_{obs}) and the absolute QY (Φ^{Eu}_{L}) using the following equations originally described by Werts et al.[11]:

$$\Phi^{Eu}_{Eu} = \tau_{obs} / \tau_{rad} = A_{rad} / (A_{rad} + A_{nr}) \text{ (eq. 3)}$$

$$\Phi^{Eu}_{Eu} = \Phi^{Eu}_{L} / \eta_{sens} \text{ (eq. 4)}$$

$$A_{rad} = 1/ \tau_{rad} = A_{MD} \times \eta^3 \times (I_{tot}/I_{MD}) \qquad \text{(eq. 5)}$$

In these equations, I_{TOT} is the integrated emission spectrum, and E_{MD} is the integrated emission band of a magnetic dipole transition ($^7F_1 \leftarrow {}^5D_0$ for Eu^{3+}). AMD is the spontaneous emission probability of the magnetic dipole transition (14.65 s^{-1} for Eu^{3+}), and n is the refractive index of the medium (1.33 for aqueous solution[12] and 1.5 for the powdered solid according to the bibliography).[13,14] These calculations have been applied to the experimental data recorded for all media: solid powder, solution and film, and the results are shown in Table 3 in the manuscript.

Table S6. Intensity parameters $\boldsymbol{\Omega_\lambda}$ and $\boldsymbol{\Omega_\lambda^{FED}}$ contributions in units of 10^{-20} cm^2 for compound $\mathbf{3_{Eu}}$ in the different measured states.

$\mathbf{3_{Eu}}$	
$\boldsymbol{\Omega_\lambda}$	$\boldsymbol{\Omega_\lambda^{FED}}$
5.18	0.0005
2.84	0.0057
0.0700	0.0145

S21. References.

1 Bruker, *APEX2*, Madison, 2012.

2 G. M. Sheldrick, *SADABS, Empirical Absorption Correction Program*, 1997.

3 M. C. Burla, R. Caliandro, M. Camalli, B. Carrozzini, G. L. Cascarano, C. Giacovazzo, M. Mallamo, A. Mazzone, G. Polidori, R. Spagna, *J. Appl. Crystallogr.*, 2012, 45, 357–361.

4 O. V Dolomanov, L. J. Bourhis, R. J. Gildea, J. A. K. K. Howard, H. Puschmann, *J. Appl. Crystallogr.*, 2009, 42, 339–341.

5 J. Rodríguez-Carvajal, *FULLPROF 2000, version 2.5d, Lab. Léon Brillouin (CEA-CNRS), Cent. d'Études deSaclay, Gif sur Yvette Cedex, Fr. 2003*.

6 Gaussian 16, Revision C.01, M. J. Frisch, G. W. Trucks, H. B. Schlegel, G. E. Scuseria, M. A. Robb, J. R. Cheeseman, G. Scalmani, V. Barone, G. A. Petersson, H. Nakatsuji, X. Li, M. Caricato, A. V Marenich, J. Bloino, B. G. Janesko, R. Gomperts, B. Mennucci, H. P. Hratchian, J. V Ortiz, A. F. Izmaylov, J. L. Sonnenberg, D. Williams-Young, F. Ding, F. Lipparini, F. Egidi, J. Goings, B. Peng, A. Petrone, T. Henderson, D. Ranasinghe, V. G. Zakrzewski, J. Gao, N. Rega, G. Zheng, W. Liang, M. Hada, M. Ehara, K. Toyota, R. Fukuda, J. Hasegawa, M. Ishida, T. Nakajima, Y. Honda, O. Kitao, H. Nakai, T. Vreven, K. Throssell, J. A. Montgomery Jr., J. E. Peralta, F. Ogliaro, M. J. Bearpark, J. J. Heyd, E. N. Brothers, K. N. Kudin, V. N. Staroverov, T. A. Keith, R. Kobayashi, J. Normand, K. Raghavachari, A. P. Rendell, J. C. Burant, S. S. Iyengar, J. Tomasi, M. Cossi, J. M. Millam, M. Klene, C. Adamo, R. Cammi, J. W. Ochterski, R. L. Martin, K. Morokuma, O. Farkas, J. B. Foresman, D. J. Fox, Gaussian, Inc., Wallingford CT, 2016.

7 A. D. Becke, *J. Chem. Phys.*, 1993, 98, 5648–5652.

8 B. Miehlich, A. Savin, H. Stoll, H. Preuss, *Chem. Phys. Lett.*, 1989, 157, 200–206.

9 C. Lee, W. Yang, R. G. Parr, *Phys. Rev. B Condens. Matter*, 1988, 37, 785–789.

10 V. A. Rassolov, J. A. Pople, M. A. Ratner, T. L. Windus, *J. Chem. Phys.*, 1998, 109, 1223–1229.

11 M. M. Francl, W. J. Pietro, W. J. Hehre, J. S. Binkley, M. S. Gordon, D. J. DeFrees, J. A. Pople, *J. Chem. Phys.*, 1982, 77, 3654–3665.

12 P. J. Hay, W. R. Wadt, *J. Chem. Phys.*, 1985, 82, 270–283.

13 N. M. O'boyle, A. L. Tenderholt, K. M. Langner, *J. Comput. Chem.*, 2008, 29, 839–845.

14 R. Dennington, T. A. Keith, J. M. Millam, 2019.